論文 / 著書情報
Article / Book Information

題目(和文)	
Title(English)	Hydraulic-Powered Ergonomic Knee Exoskeleton for the Elderly
著者(和文)	KITTISARESSarin
Author(English)	Sarin Kittisares
出典(和文)	学位:博士(工学), 学位授与機関:東京工業大学, 報告番号:甲第12528号, 授与年月日:2023年9月22日, 学位の種別:課程博士, 審査員:鈴森 康一,遠藤 玄,吉田 和弘,塚越 秀行,菅原 雄介
Citation(English)	Degree:Doctor (Engineering), Conferring organization: Tokyo Institute of Technology, Report number:甲第12528号, Conferred date:2023/9/22, Degree Type:Course doctor, Examiner:,,,,
学位種別(和文)	博士論文
Type(English)	Doctoral Thesis

Department of Mechanical Engineering
Graduate Major in Mechanical Engineering
Doctoral Thesis
2023

Hydraulic-Powered Ergonomic Knee Exoskeleton for the Elderly

Advisors Prof. Koichi Suzumori
Prof. Gen Endo

Sarin Kittisares
Graduate Major in Mechanical Engineering
School of Engineering
Tokyo Institute of Technology

Abstract

Falls pose a significant health risk among older individuals, particularly during Activities of Daily Living (ADL), such as sit-to-stand (STS) or stair climbing (SC), primarily due to deteriorated extremity power and torque deficits. While robotic exoskeletons have been developed to assist the elderly with ADLs, current designs suffer from discomfort caused by high inertia and human-robot kinematic incompatibilities. To address these issues, this thesis focuses on the development of ergonomic four-bar mechanisms and the integration of hydraulic artificial muscles (HAM) to reduce kinematic discrepancies, system weight, and inertia, thereby reducing discomfort.

Chapter 1 of the thesis provides a comprehensive introduction to the hazard risk associated with ADLs in the elderly population. It highlights the significance of falls and their impact on health, mortality, and quality of life. The chapter also discusses the existing approaches in assistive technology for addressing these challenges. A major focus of Chapter 1 is on robotic exoskeletons, which are considered one of the most advanced and versatile assistive technologies available today. The chapter explores the current capabilities and limitations of exoskeletons in supporting ADLs. Additionally, the chapter also discusses the use of hydraulic systems in wearable robotics, particularly in the context of exoskeleton design. Chapter 1 sets the foundation for the subsequent chapters, establishing the importance of developing advanced and effective assistive technologies, particularly robotic exoskeletons, and highlighting the potential of hydraulic systems in enhancing their capabilities.

Chapter 2 presents a novel knee exoskeleton designed specifically for STS assistance. The exoskeleton combines a HAM with a four-bar linkage joint to provide effective support during the STS motion. The key innovation of the proposed exoskeleton lies in its utilization of the unique force-contraction relationship of the HAM. This allows for the generation of varying torque at different joint positions,

which is achieved through the geometric design of the proposed Angled Bar. By incorporating the four-bar linkage, the joint mechanism becomes polycentric, closely resembling the motion of natural knee joints and minimizing any discomfort that may arise from the exoskeleton. Experimental results demonstrate the device's ability to generate the required torque for STS with the peak value of 70.7 N m at 100° knee joint angle. The root-mean-square error was approximately 5 N m. Additionally, a subject study was conducted to evaluate the impact of the exoskeleton on muscle activity. The study revealed a significant reduction in muscle activity of the Rectus femoris, with the peak Electromyography (EMG) signal decreasing from 52.1 µV without assistance to 20.9 µV with the assistance of the exoskeleton. These findings further support the efficacy of the device in reducing the muscular effort required during STS movements.

Chapter 3 proposes a novel multi-degree-of-freedom (DoF) hydraulic system specifically designed for mobile and wearable robots. The primary goal of the system is to reduce weight and improve power efficiency while maintaining adequate control over multiple actuators. The proposed hydraulic system combines the advantages of traditional centralized hydraulic systems and electrohydraulic actuators (EHA) by incorporating on-off valves for channel switching. This design choice facilitates the efficient control of hydraulic pressure and volume in multiple actuators simultaneously, albeit with a minor trade-off in performance. Two control algorithms, namely the alternating pressure control system (APCS) and the multi-channel EHA (MEHA), are introduced. Additionally, two variants of the APCS, designed to enhance power efficiency and reduce reliance on sensor feedback, are proposed. The system allows for simultaneous control of pressure and volume in multiple actuators virtually, albeit with a small error and delay. The system's ability to reduce weight, improve power efficiency, and enable effective control over multiple actuators opens new possibilities for the development of mobile and wearable multi-DoF hydraulic robots.

Chapter 4 builds upon the findings of Chapters 2 and 3 to propose a multi-DoF powered exoskeleton for SC assistance. The device incorporates an asymmetric dual four-bar linkage mechanism for the knee joint, enabling the higher power requirements of SC and allowing internal rotation of the knee joint. The parameters of the four-bar linkage were optimized through a genetic algorithm to replicate the kinematics of the biological knee joint on both the medial and lateral sides. The de-

vice was evaluated through three experiments. First, the torque output device was measured to validate the performance of the proposed device. Second, the improved comfort of the proposed joint mechanism was evaluated through measurement of undesired load, which reduced from 14.15 N and 18.32 N to 1.88 N and 1.07 N on the medial and lateral sides, respectively. Third, the supportive capabilities of the device were validated with a human subject. The EMG signal of the Rectus femoris reduced from 52.34 µV to 23.06 µV with the assistance of the proposed exoskeleton. This chapter provides a basis for the development of a more compact and more comfortable design in future iterations.

This research contributes to the field of wearable robotics by developing ergonomic designs and integrating hydraulic artificial muscles, reducing discomfort, and enhancing performance during ADLs. The proposed knee exoskeleton and hydraulic system lay the foundation for future advancements in assisting older individuals with daily activities, thereby mitigating the risk of falls and improving their overall well-being.

Contents

List of Figures

List of Tables

List of Symbols

D	diameter of tubing when the braiding angle is 90°
d_0	diameter of tubing at rest length
d_e	effective diameter of tubing at rest length
DR	dynamic duty ratio
$\mathrm{DR}_{\mathrm{app}}$	applicable value of dynamic duty ratio
e	regression error term
EDM	Energy Density per Mass
f	source pressure frequency
F	contraction force of the HAM
f_P	function of point P of the four bar linkage
FDM	Force Density per Mass
k	generation of genetic algorithm
k_e	elastic constant
l	length of the artificial muscle
l_0	rest length of the device
l_1	length of Angle Bar
l_2	x coordinate of the fixed end of the HAM
l_3	y coordinate of the fixed end of the HAM
m	mass
n	number of sampled points
n_t	turn number of a sleeve strand
P	pressure
$\mathbf{P}_{\mathrm{knee},i}$	position vector of the biological knee joint at angle i
$P_{r,i}$	reference pressure of actuator i

P_a	actuator pressure
P_i	pressure required to inflate the unconstrained inner tube to a diameter equivalent to the device diameter at any value of ϕ
P_r	reference pressure
P_s	source pressure
r_1	length of link AB
r_2	length of link BC
r_3	length of link CD
r_4	length of link AD
RMSE	Root Mean Square Error
s	Laplace variable
s_e	length of a sleeve strand
t_{close}	closing instance of the valve
t_{fall}	fall time
t_{open}	total duration for which the valve is open, including the operating period of the valve
t_{period}	period of each actuator
t_{rise}	rise time
t_{settling}	settling period of source pressure
$T_{req,i}$	required torque at knee joint at point i
T_i	torque generated using selected parameters at point i
u_s	coefficient of friction between the strands of the helical sleeve
$u_s t$	coefficient of friction between the strands of the sleeving and the inner tube
V_a	actuator volume
V_r	reference actuator volume
x	position
$\mathbf{x}$	optimization variable vector containing initial position of points A, B, C, and D
x_{ICR}	x coordinate of ICR
x_i	current state of actuator i

$x_{r,i}$	reference signal of actuator i
x_A	x coordinate of point A
x_B	x coordinate of point B
x_C	x coordinate of point C
x_D	x coordinate of point D
x_E	x coordinate of point E
y_{ICR}	y coordinate of ICR
$y_{r,i}$	reference value at point i
y_A	y coordinate of point A
y_B	y coordinate of point B
y_C	y coordinate of point C
y_D	y coordinate of point D
y_E	y coordinate of point E
y_i	measured value at point i
β_0	vertical intercept
β_1	regression coefficient
ϵ	error band
ε	contraction ratio
$\varepsilon_{\text{max},e}$	measured maximum contraction ratio
ε_{max}	maximum contraction ratio
ϕ	braiding angle
ϕ_0	initial braiding angle
ϕ_e	effective braiding angle
ψ	bending angle of the Angled Bar
σ_k	standard deviation at generation k
θ_{knee}	knee joint angle
θ_{max}	maximum knee flexion angle
θ_1	angle of link AB
θ_2	angle of link BC
$\theta_{2,0}$	initial angle of link BC
θ_3	angle of link CD
θ_4	angle of link AD

Chapter 1

Introduction

1.1 Background

Falling accidents are a major health risk in older people. In 2011, the Canadian Institute for Health Information reported that 74% of hospitalizations from major injury for cases age 65 and older were caused by falls. Moreover, unintentional falls are the leading external cause of death, causing 76% of deaths from injury in the 65 and older age group [1, 2]. Most falls are unintentional (as opposed to intentional falls such as assault or suicide) and are preventable.

Falls are exceptionally deadly in the elderly particularly due to the increased risk of fractures. Fractures, such as hip fractures, significantly elevate the mortality risk in the elderly. For instance, hip fractures result in five to eight times greater risk of mortality within the first three months [3] and 1.8 years or 25% reduced life expectancy compared to similar demographics [4]. Survivors of initial fracture may also need to spend a large proportion of the lifetime in nursing facilities, having a lower quality of life and high healthcare expense [4].

The specific actions involved in activities of daily living (ADLs) play a crucial role in the risk of falling among older adults. Self-reported data from older adults consistently indicate that sit-to-stand (STS) and stair climbing (SC) movements are among the most challenging ADLs they encounter, as highlighted in a study by Verghese et al. [5]. Statistical data also supports their concerns, with rising, sitting down, and stair negotiation being some of the actions with the highest risk of accidents for the elderly [2, 6, 7].

Older adults are more prone to falls due to several risk factors, including de-

creased muscle strength, balance impairment, and cognitive impairment [8]. The decreased muscular capability in particular is mechanically limiting older adults' capability to perform ADLs. Hortobágyi et al. [9] found that old adults perform STS and SC, near their maximal capabilities. Another study by Böhme et al. [10] reported a significant power deficit in the elderly during SC. Previous studies on STS also confirmed that adequate lower extremities strength is crucial for successful STS; among the three joints that are required for STS, namely the ankle, knee, and hip, the knee joint has the highest torque requirement [10–12] and is a limiting factor for STS action [13]. Moreover, lower extremities are a stronger predictor of success than balance control for successful STS [14].

The identification of STS and SC as actions associated with an elevated risk of falls highlights the importance of targeting these specific activities for preventive interventions and assistive technologies. By developing strategies and technologies that address the unique challenges posed by these actions, it is possible to significantly reduce the incidence of falls among older adults and enhance their safety and independence in performing ADLs.

1.2 Traditional Assistive Devices

With lower extremity strength being the most significant factor for falling accidents, previous assistive devices aim to provide additional force or torque to support the action. These devices can be roughly divided into two main categories: manual and powered. Manual devices, such as canes, transfer poles, assist rails, and handles, do not directly provide mechanical assistance but depend on the user's upper extremities to contribute additional force to support challenging ADLs. Powered devices, on the other hands, are designed to directly provide assistive force or torque to the user to perform a specific action. For example, powered seat, stand assist power lift, and stair lifts are devices designed specifically for STS and SC support. They are installed or placed at the required locations to be activated upon the user's request.

1.2.1 Manual Assistive Device

Manual devices are equipment designed to assist users in using their upper extremities to pull or push themselves and provide additional force or stabilize their

movement. They do not provide mechanical assistance by themselves and their utilities are limited by the user's upper extremity strength and stability. This type of device may be completely mobile, or permanently or semi-permanently installed to the locations where assistance is required. Mobile manual devices are relatively light and small and may be beneficial for other actions such as walking at the cost of significantly lower stability. Examples of mobile devices include walking sticks, quad canes, and walkers.

In contrast, permanent equipment, such as rails, handles, poles, or stair climbing aids [15] are permanently installed to assist the elderly where a more difficult ADL is required. Their usefulness is limited to the area where they are installed. Semi-permanent equipment, such as tension poles, depends on friction and tension to fix itself to the floor and ceiling. This type of equipment may require regular inspection to prevent the devices from becoming the cause of accidents themselves. Novel manual assistive device such as the tension pole based movable handrail [16] reduces the limitation of these device, but their applicability and safety in real-world settings remain unproven.

1.2.2 Powered Assistive Device

Powered assistive devices have been developed to provide external mechanical assistance to individuals during challenging ADLs. While these devices are effective in helping users achieve the desired location and posture, several important considerations need to be addressed, including safety, user balance, posture, and mobility. Numerous research studies have investigated the use of powered assistive devices, employing various approaches and achieving varying degrees of success. In this section, previous commercial and experimental powered devices are discussed.

The most common commercial devices for STS assist is the standing lift such as the Molift Quick Raiser 2 (Etac AB, Kista, Sweden) [17] shown in Fig. 1.1. The caretaker moves the device next to the patient and straps the patient to the device. The device then hoists the patient up from a seated position to a standing position as shown in Fig. 1.1. The caretaker may then place the patient on a wheelchair or move the patient along with the device. This type of device's main purpose is to help caretakers move their patients; the patient is required to exercise neither their upper nor lower extremities as the standing lift provides all of the required force.

Figure 1.1: A standing lift with a patient strapped to the device. [17].

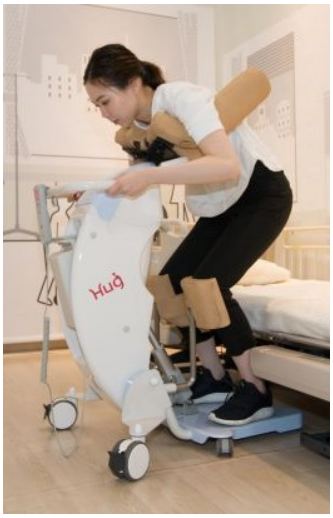

Figure 1.2: A mobility support robot. [18].

This, however, is not beneficial for rehabilitative purposes as the resulting standing motion differs greatly from normal STS trajectory. Moreover, the patient cannot utilize their muscles, which may further deteriorate their remaining strength. For these reasons, this type of device is only suitable for terminal patients in nursing homes with the constant presence of a caretaker.

Mobility support robots such as the Hug T1 (FUJI CORPORATION, Aichi, Japan) [18] shown in Fig. 1.2 have also been developed as an alternative to standing lifts. The robot "hugs" the patient and lift them up, reducing the workload of caretakers when assisting patients. These devices are an improvement to the previous standing lifts in the rehabilitation aspect: they allow patients to exercise their muscles while standing up. Furthermore, the STS motion provided by the robot simulates a natural trajectory of the STS action. However, as a device designed to assist caretakers in nursing facilities, they are large and bulky and not suitable for outdoor use. Thus, they cannot enhance the older people's ability to live independently.

Another popular type of commercial device is the power lift recliner [19] shown in Fig. 1.3, which doubles as a recliner chair and an assistive device for older people. A study by Ruszala and Musa [20] showed that power lift recliners provide the least stability and ease of use compared to other powered assistive devices. However, they

Figure 1.3: A power lift recliner chair in a lifted position. [19].

Figure 1.4: A stair lift [21].

also enable the elderly to sit up by themselves in some cases thus preserving their dignity. As a recliner chair, they are suitable for older people who only needs minor assistance in their home, but not for outdoor use.

Lastly, stair lifts including the Elan Straight Indoor Stair Lift (Bruno Independent Living Aids, Inc., WI, USA) shown in Fig. 1.4 are often used for SC assist. This type of device are seats attached to a powered rails installed on stair railings. The user sits on the stair lift then activates it to bring themselves up or down stairs. They provide a safe way for older people to travel up or down stairs independently. The primary drawback of a stair lift is similar to other types of powered devices: reduced physical activity in older individuals can potentially lead to further decline in their remaining strength, and these devices are confined to the specific installation location.

To summarize, the main disadvantage of powered assistive devices are their low mobility and the user's inability to exercise their own muscle. They are more suitable for reducing the workload of caretakers in nursing homes than promoting the independence of the user.

1.3 Robotic Exoskeleton

A robotic exoskeleton, also known as a powered exoskeleton, is a wearable device that enhances the strength, endurance, and mobility of a person. It is a type of exoskeleton that uses powered motors or other types of actuators to provide assistance to the user's natural movements.

Robotic exoskeletons can be used for a variety of applications, including medical rehabilitation, disaster response, and industrial work. In medical rehabilitation, they are used to help patients recover from injuries or disabilities by providing support to weakened or paralyzed muscles. In disaster response, they can help rescuers carry heavy loads or traverse difficult terrains. In industrial settings, they can be used to reduce worker fatigue and prevent injuries from repetitive motions.

Commercial lower extremity exoskeletons, including HAL (CYBERDYNE, INC., Ibaraki, Japan) [22], ReWalk Personal (ReWalk Robotics, Inc., MA, USA) [23], Ekso NR (Ekso Bionics Holdings Inc., CA, USA) [24], and REX (REX Bionics Inc., MA, USA) [25] have been developed to assist paraplegics, stroke victims and other paralyzed or semi-paralyzed people to stand up, sit down, and walk independently. They enabled the disabled to achieve impressive feats such as completing a marathon. Currently, these devices are being deployed in medical facilities to support patients and health professionals in rehabilitation processes.

Studies on knee exoskeleton in the literature found them to be beneficial for ADL assistance. In [26], a knee exoskeleton was developed to assist individuals with poststroke hemiparesis. The force from the motor was transmitted to the knee joint using a belt drive and a linear guide. A fiberglass beam was added to function as a spring between the linear guide and the knee joint. Experiments with able-bodied participants showed that the device was beneficial in assisting STS action. Another study [27] evaluated the effectiveness of a lower limb exoskeleton for SC assist in healthy young persons. The found that metabolic costs, namely net oxygen cost and total heart beats were reduced with assistance without affecting climbing speeds. These studies shows that exoskeleton is a promising technology for ADL assistance.

However, despite their usefulness and effectiveness, there are two main issues with physical human-robot interaction (pHRI) in current lower-limb exoskeletons: human-robot misalignment, and increased weight and inertia. These issues make

Figure 1.5: A person wearing the ReWalk Personal exoskeleton [23].

exoskeleton uncomfortable and even potentially dangerous for its users.

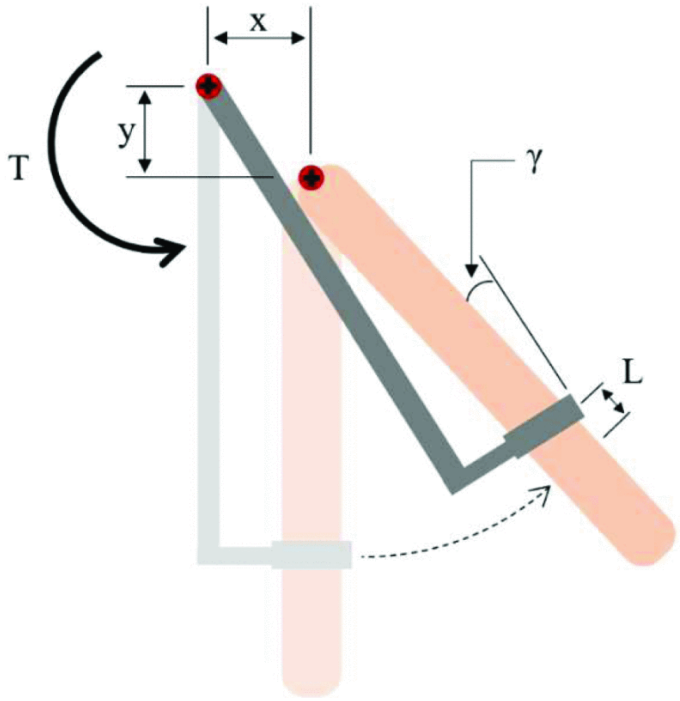

Figure 1.6: Misalignment between human joint and robot joint causing slip and undesirable force, resulting in discomfort. From [31]. ©2020 IEEE

1.3.1 Human-Robot Misalignment

Most lower-extremities wearable robots utilize simple revolute joints as the knee joint. In contrast, while the human knee joint is functionally similar to revolute joints, its movements are much more complex. The mismatch between the kinematics of wearable robot and its wearer results in an undesired misalignment as shown in Fig. 1.6. The resulting misalignment may cause discomfort due to abrasion [28–33], or unintended load which may cause injuries such as muscle damage or internal bleeding [29, 31, 34, 35]. An assistive device with low comfort may also cause the user to abandon the equipment [36]. Lastly, joint misalignment also have a negative effect on metabolic consumption as the user has to adapt to the exoskeleton instead of the opposite [37]. An ergonomic knee joint mechanism based on biomechanics of the knee may be able to reduce these concerns.

In the human knee joint, the tibiofemoral joint surface has a unique combination of rolling and sliding of the tibia on the femur [38–40]. First, the shape of the femoral condyle is not circular: several mathematical models have been proposed including segments of circles [38], and oval [40]. Second, there are four main ligaments in

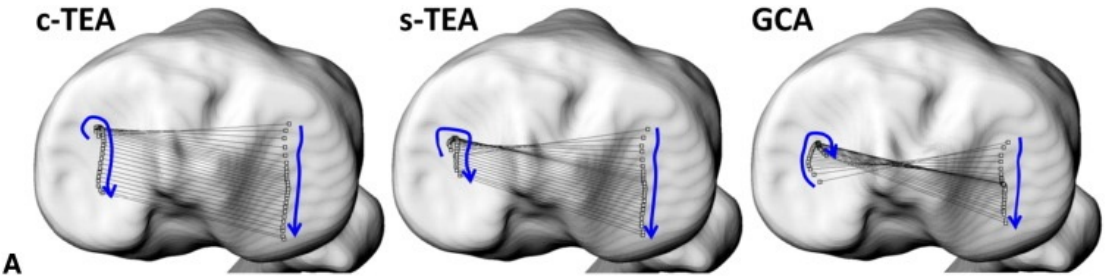

Figure 1.7: Trajectory of medial and lateral femoral condyles relative to the tibia during a flexion motion. Internal rotation of the knee is shown through three different anatomical axes. From [43].

the knee, namely the Anterior Cruciate Ligament (ACL), the Posterior Cruciate Ligament (PCL), the Medial Collateral Ligament (MDL), and the Lateral Collateral Ligament (LDL) as shown in Fig. 1.8. These ligaments affect the percentage of rolling-sliding ratio of the knee. Additionally, the femoral condyle have a different shape on the medial and lateral side, resulting in an internal rotation during the flexion motion of the knee [38, 41–43]. This internal rotation can be clearly seen in Fig. 1.7, where three anatomical axes in the femur are shown to undergo an internal rotation relative to the tibia.

Extensive research has been conducted on the kinematics of the knee, and several knee models have been proposed in the literature for total knee arthroplasty (TKA). TKA is a surgical procedure that involves replacing a damaged or diseased knee joint with an artificial joint. Employing a knee joint model for TKA enables surgeons to ascertain the optimal position, size, and alignment of the artificial joint components based on each patient's individual anatomy. In the subsequent sections, a selection of models from the literature will be introduced.

Instant Center of Rotation

A body undergoing a planar movement other than pure translation has a point that has zero velocity called instant center of rotation (ICR) at any instant. The path traced by the ICR is called a centrode. Previous studies found the the centrode of the tibia is a J-shaped curved path [40] as shown in Fig. 1.9.

There are two different approaches for determining the instant center of rotation of a mechanism: the tangent method and the Reuleaux method.

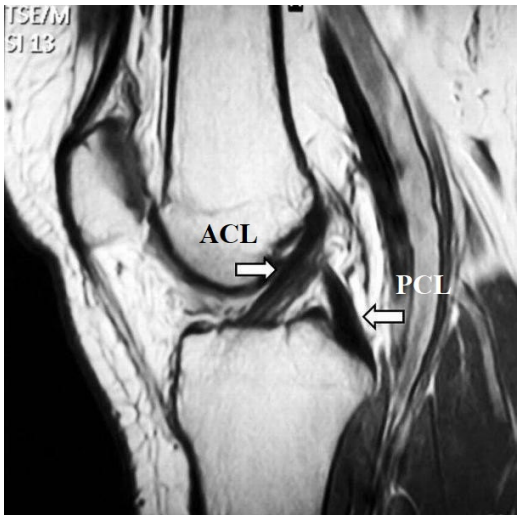

Figure 1.8: An MRI image showing the ACL and PCL, as well as the femoral condyle in the sagittal plane. The anterior side is to the left [44].

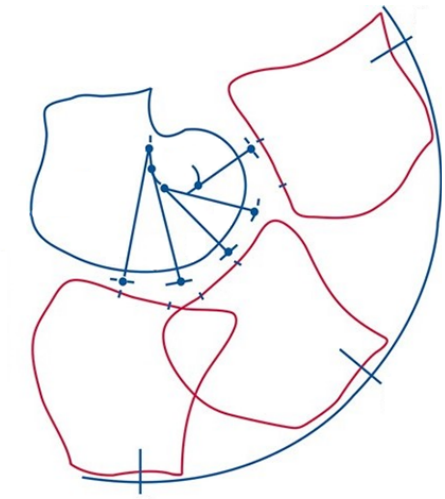

Figure 1.9: Positions of knee ICR at different knee positions, tracing a J-shaped centrode [40].

The tangent method involves drawing a tangent to the path of motion of a point on the moving link of the mechanism. The intersection of the tangent line with the corresponding tangent line from another moving link of the mechanism gives the ICR. This method is based on the fact that the relative motion between two links of a mechanism is always along a tangent to the path of motion of a point on the moving link. However, the tangent method is very difficult to apply in practice because instantaneous velocity is challenging to obtain [45].

In contrast, the Reuleaux method estimates the direction of instantaneous velocity by drawing a line between sequential positions, resulting in circles around the pivots of each link of the mechanism. The instant center of rotation is the intersection point of the common tangent to any two circles. This method is based on the fact that the motion of any link in a mechanism is equivalent to the rolling motion of a circle without slipping on another circle. The Reuleaux method is prone to measurement error, especially due to the fact that the movement of a human knee is not perfectly planar [45].

To summarize, the ICR model assumes the motion of the knee to be a planar motion. The main disadvantages of this model are that it ignores the internal

rotation of the tibia, and calculation of the ICR is susceptible to noisy measurements. As a result, the calculated ICR values may exhibit substantial discrepancies between each measurements.

Instantaneous Helical Axis

A generalization of the concept of ICR to a three dimensional space, the Instantaneous Helical Axis (IHA) describes the instantaneous motion of a rigid body undergoing a complex motion, such as a combination of translation and rotation. The IHA is the axis around which a rigid body appears to rotate at any given instant, and it represents the direction and rate of change of the body's angular velocity vector.

Chasles' theorem, named after French mathematician Michel Chasles, states that any rigid body motion can be described as a combination of a translation along a straight line and a rotation about an axis that is parallel to that line. This means that the motion of a rigid body can be completely characterized by specifying the distance and direction of the translation, as well as the orientation and location of the helical axis [46]. The plane traced by the IHA is called an axoid [45].

While the IHA can describe the movement of the knee most accurately in theory, it also suffers from noisy measurement similar to its planar counterpart. Furthermore, a previous study has found that an external force acting on the knee can result in a greatly different axoids [47], making measurement of the knee axoid extremely challenging.

Functional Axis

A simplified description of the motion of the knee usually adopted by surgeons in TKA without requiring deep understanding of kinematics. The movement of the knee is described as simultaneous rotation about two fixed axes: the flexion-extension axis (FEA) in the posterior femoral condyles and the longitudinal axis (LRA) in the tibia. In this model, the condyle is assumed to be a cylinder. The FEA is defined as the axis in the femur which has a constant distance to the tibia, since the center of a cylinder on a planar surface always has the same distance to the surface regardless of whether it is rolling, sliding, or a combination of both. Internal rotation of the knee is modeled as rotational motion on the LRA. This model can

adequately approximate the kinematics of the knee only between approximately 0° to 60°, where the shape of the condyle is relatively circular [48].

Ergonomic Mechanisms

One of the simpler mechanisms aimed to improve pHRI is a serial revolute joint such as in [49]. The mechanism is also present in many commercial off-the-shelf knee braces. The mechanism consists of three links: thigh, knee, and shank. Two gear inside the knee part make the angle between the thigh and the knee, and the knee and the shank equal. In this mechanism, the ICR is at the center of the knee part. During knee flexion, the ICR moves backward and upwards, which is different from the J-shaped centrode of natural knees.

A more complex approach is the four-bar linkage, which is one of the earliest knee mechanisms utilized in prosthetic [50]. The goal of utilizing the four-bar linkage in lower limb prostheses was to increase stability and achieve knee lock in the stance phase of walking.

Four-bar linkage mechanisms have also been applied to simulate various aspects of knee joint, including the ACL and PCL ligaments [51] shown in Fig. 1.10, the shape of the condyle [52], and the centrode and axoid of the knee [32, 53, 54]. Zavatsky and O'Connor [51] found that there is minimal change in length of the ligaments during knee flexion. They proposed that stiff bar model is a reasonable simplification of the human knee. Another group of researcher optimized a four-bar linkage to the shape of the condyle [52]. Lastly, various studies including [32, 53, 54] replicated the centroid or axoid of the human knee using a four-bar linkage. They used optimization techniques such as genetic algorithm (GA) or particle swarm optimization to optimize the initial position of four bar linkages. They found that four-bar linkage has a significant improvement over simple revolute joints and polycentric serial revolute joints [53].

Although a planar four-bar linkage is an improvement over simpler mechanisms, it cannot account for the internal/external rotation of the tibia. In response, researchers in the study [55] proposed a 2-degrees-of-freedom (DoF) humanoid dual cross four-bar mechanism, which not only utilizes the four-bar linkage to allow for ICR translation, but also incorporates a set of adaptive roller mechanisms to allow for internal rotation. The researchers suggested that a dual asymmetric four-bar

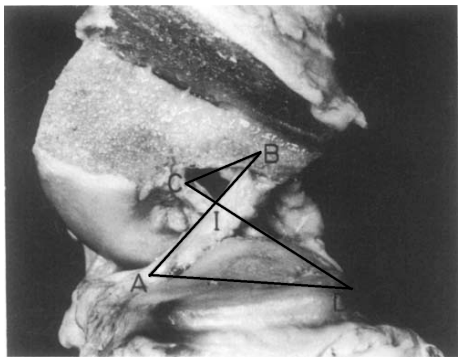

Figure 1.10: A crossed four-bar linkage mechanism overlaid on a sagittal view of the human knee [51]

linkage or a roller mechanism could be adopted to enable internal rotation, thus providing greater flexibility and precision in the design of exoskeletons.

Another solution to reduce kinematic incompatibility is by including additional passive compensation joints to compensate for the misalignment [28, 56]. One such example is the adoption of compliant mechanisms such as the Schmidt coupling, which allows ICR translation in the Assist-On Knee exoskeleton [57] shown in Fig. 1.12. A Schmidt coupling is a coupling which allows radial displacement between two shafts. The mechanism consists of seven rigid bodies: three rotational rings and two connecting links between each pair of rings as shown in Fig. 1.11. The Schmidt coupling was driven by a Bowden cable, which is connected to a motor at the hip. Since the Schmidt coupling self aligns the mechanical joint to the knee ICR, the device can always adjust itself in the sagittal plane to the user despite the differences between individuals. Conversely, since the Schmidt coupling allows free translational motion between the femur and the tibia, it cannot provide weight-bearing support, and the human joint needs to bear all the added weight of the exoskeleton. This may add more burden to the user, thereby reducing the comfort of the device. Electromyography (EMG) signal levels showed that the exoskeleton was effective in reducing muscle activity during STS.

Another group of researchers also took a compliant approach by developing a multiarticular soft exosuit for gait assistance [58]. The leg component of the exosuit is mostly constructed of textile. Therefore, the device easily adjusts to the user, with very low weight and little to no effect on kinematics compared to the rigid exoskeleton. The suit is driven by Bowden cables, which are connected between the

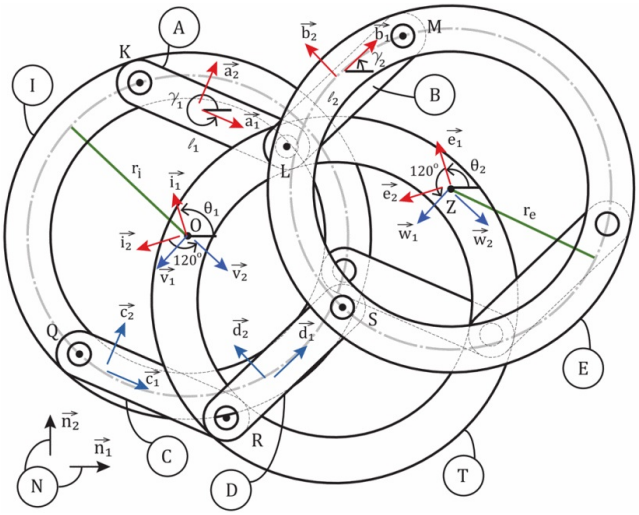

Figure 1.11: Schematic diagram of Schmidt coupling [57]. ©2011 IEEE

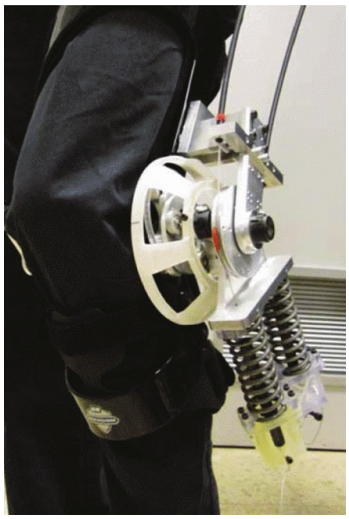

Figure 1.12: The Assist-On Knee exoskeleton [57]. ©2011 IEEE

hip and both heels. This allows one Bowden cable to induce torque on both the hip and the ankle simultaneously. Experiment results showed that the exosuit reduces the metabolic cost of walking on healthy subjects. Similar to AssistOn-Knee, the soft exosuit cannot provide any weight-bearing assistance.

In summary, several studies in the literature have suggested different ergonomic mechanisms to address the issue of misalignment between humans and robots. One such approach involves the use of rigid components that enable weight-bearing, albeit at the expense of some minor misalignment. Conversely, more compliant mechanisms are designed to allow a wearable device to conform fully to the biomechanics of the user, although this may come at the cost of sacrificing its weight-bearing capabilities.

Support Design

Another potential cause of human-robot misalignment is the mechanical support equipment that connects the wearable device to the user. They are responsible for ensuring the correct positioning of the exoskeleton on the human body and transmitting assistive force or torque from the assistive device to the user. They should also be comfortable for the user and allow the device to be easily worn and removed [28].

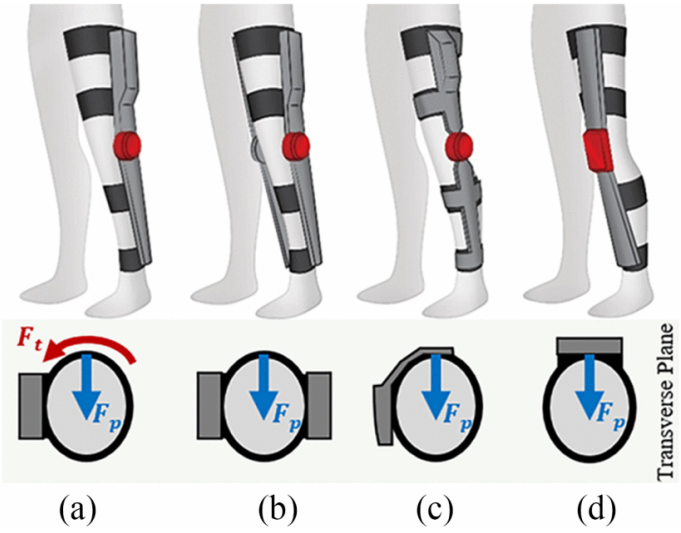

Figure 1.13: Illustration of different knee exoskeleton layouts. F_p represents transmitted force, and F_t represents undesired twisting force. (a) Lateral-support layout (b) Two-side-support layout (c) Stiff lateral-support layout (d) Anterior-support layout [59]. ©2011 IEEE

In the literature, most exoskeletons use a combination of stiff and soft materials as their connective components. Stiff equipment, such as braces or cuffs, minimizes relative displacement between the human and robot, enabling better force transmission. However, these stiff components are often uncomfortable as they do not allow the muscles to deform naturally during muscle contraction. Moreover, they may cause pain when intense pressure is applied to the human limb due to assistive force. On the other hand, soft components like belts, straps, or harnesses are frequently used to fasten the wearable device to the user. These components can freely deform to the user's contour, allowing the exoskeleton to be securely fixed to the user. However, the deformability of these components may also lead to misalignment, create undesired torque, or reduce force transmission efficiency.

The layout of the knee joint exoskeleton is also a crucial consideration in support design. A unilateral exoskeleton with soft support can exert an undesired twisting force [59, 60], as shown in Fig. 1.13. This further contributes to misalignment and discomfort in the device. To address this issue, several solutions can be considered, such as adopting a two-side-support layout, using stiff support braces, or supporting on the anterior or posterior side of the leg. However, each solution comes with its own challenges: a two-side-support layout needs to account for the internal rotation

of the knee, stiff braces may cause additional discomfort, and implementing anterior support is considerably more difficult than other layouts.

1.3.2 Weight and Inertia

Traditional exoskeletons are commonly equipped with electric motors to act as their actuators. These motors play an important role in the functioning of the exoskeleton, as they convert electrical energy into mechanical energy by using the interaction between an electric current and a magnetic field to generate torque. Despite their usefulness, however, these motors can be heavy due to their construction and the materials used in their manufacturing. The weight of a motor is typically proportional to its power output, with larger and more powerful motors tending to be heavier. Consequently, exoskeletons relying on electromagnetic motors tend to be heavier compared to other types of exoskeletons. For example, each electrically actuated joint in the BLEEX 2 exoskeleton weighs as much as 4.1 kg, doubling that of hydraulically actuated joint in their previous BLEEX exoskeleton [61]. Table 1.1 summarizes the weights and peak torque of recent knee exoskeletons. The weights of other support equipment such as the power source, battery, pump, or compressor are not included unless specified.

The developers of motor-based exoskeletons claimed that the added weight of the exoskeleton is not a a major concern as the exoskeleton can bear its own weight. However, the added weight can have other effects on its performance. Specifically, the added weight can result in increased inertia and moment of inertia. This means that the exoskeleton will require more force to start and stop moving, as well as to change direction, because of the increased mass of the motor. In other words, the exoskeleton may feel less responsive to the user, requiring them to adapt to the movement of the exoskeleton instead of the opposite.

To better understand the effects of added weight and moment of inertia on the human body, a study was conducted in [62]. The researchers attached several configurations of mass to the participant's lower extremity to determine the effects of added weight and moment of inertia during walking. The results were compared to a baseline setup which has a mean of 2.0 kg added mass, and the researchers found that increasing the moment of inertia by 5% without increasing the weight resulted in an increase in energy cost of 3.4%. They also found that increasing the

Table 1.1: Weight and peak torque of recent knee exoskeletons.

Study	Transmission	Actuator	Peak torque [N m]	Weight [kg]	Torque/Weight [N m kg^{-1}]
KNEXO [63]	Pneumatic	Pleated PAM	75	4.5	16.67
AssistOn-Knee [57]	Bowden cable	External motor	780	1.4	557.14
Kim et al. [54]	Electrical	Motor (with battery)	38	3.5	10.86
Witte et al. [64]	Bowden cable	External motor	120	0.76	157.89
Wang et al. [59]	Electrical	Motor	16	1.82	8.79
Sarkisian et al. [60]	Electrical	Motor	120	2.5	48
Lee et al. [65]	Electrical	Motor	17.4	1.5	11.6
Rituraj et al. [66]	Hydraulic	Cylinder	100	2.8	35.71

weight of lower extremities by 5% without increasing moment of inertia increased energy cost by 4.0%.

Another study by Liu et al. [67] evaluated the effects of weight distribution of exoskeletons on muscle activities. They created four knee exoskeletons using identical components, with a different motor and gear box positioning and test them on five able-bodied participants in various activities. They found that muscle activities varied among weight distributions and movements, and no weight distribution is optimal for all activities.

One solution to reduce the added weight to the body is by utilizing a remote actuation system, positioning the support actuation system and power source externally. The exoskeleton needs to be tethered to the remote actuation system to operate. While this reduces the mobility of the device, the reduced weight makes the exoskeleton suitable for applications in limited areas such as rehabilitation. Examples of power transmission for exoskeletons include pneumatic, hydraulic, and Bowden cable systems [57, 63, 64, 66, 68, 69].

Among the remote actuation system for exoskeletons, Bowden cable systems have the highest peak-torque-per-weight ratio due to the powerful external system as shown in Table 1.1. This is required to overcome the significant friction of the Bowden cable, where force transmission efficiency may be as low as 50% [69, 70]. Moreover, Bowden cable friction is also nonlinear, depending on the curvature of the cable, making precise control of the Bowden cable a challenge [68–70]. On the other hand, a pneumatic remote actuation system offers high power density and is inherently compliant, which can be beneficial in pHRI. The main disadvantage of a pneumatic remote actuation system is nonlinear control and a small achievable bandwidth [70]. Finally, hydraulic remote actuation systems offer the highest power density [71] and high bandwidth [70], making them suitable for wearable robots.

Traditional hydraulic actuators, such as hydraulic motors or cylinders, are often made from metal, making them heavy. To further mitigate the effects of added weight and inertia, designers may consider alternative actuators such as a hydraulic artificial muscle (HAM), which is much lighter than a comparable electric motor or hydraulic cylinders, thanks to its excellent power-to-weight ratio [72, 73]. Hydraulic actuators also allow the application of a remote actuation system, reducing inertia and moment of inertia.

1.4 Hydraulic System

Hydraulic actuators have been employed in heavy machinery for a long time owing to their large force output, high force and power density, and good impact resistance [71, 74, 75]. These advantages make them suitable for tough robotic applications [76–79], mobile robots [80–83], and wearable robots [84, 85]. Hydraulic actuators also have a potential to be adopted in other multi-degree-of-freedom mechanical systems. In addition, hydraulic power allows application of lighter soft hydraulic actuators as HAMs. However, the main challenges of hydraulic power in mobile robots and wearable robots are the hydraulic supply system, weights of various hydraulic components and power consumption. Reducing size and weight in addition to increasing power efficiency will improve operational range and duration of mobile and wearable hydraulic robots, both of which are crucial in actual application.

1.4.1 Centralized Hydraulic System

A traditional centralized hydraulic system is a type of hydraulic power system that uses a central pump to generate hydraulic fluid pressure. This system typically consists of a pump, a hydraulic reservoir, valves, and actuators. The pump creates pressure by forcing hydraulic fluid from the reservoir through the system's pipes and valves, which then actuate hydraulic cylinders, motors, or other components. The central pump is usually powered by an electric motor or an internal combustion engine. The hydraulic fluid used in the system is typically oil-based, and it is stored in the reservoir when not in use. The hydraulic system is typically used in heavy machinery, such as construction equipment and industrial machinery, where high levels of power and control are required.

Fundamentally, hydraulic systems are classified into mobile hydraulics and industrial hydraulics [78, 86]. In mobile hydraulics, several functions have been employed using a single pump, and the flow and pressure demands vary considerably between functions. The components in mobile hydraulics were integrated as a single all-in-one inclusive system. In contrast, industrial hydraulics are placed in stationary systems where hydraulic power is supplied from a large hydraulic infrastructure. Recent research efforts focused on mobile hydraulics with the primary concerns of energy efficiency, weight, static and dynamic behavior, operability, and controlability [78, 86, 87].

In general, most current mobile hydraulic systems are operated with a fixed displacement pump and open-center valves [86]. In this type of system, the fixed displacement pump provides a constant flow to all actuators. Comparatively, open-center systems are less expensive owing to the relatively low cost of fixed displacement pumps. Moreover, they are simple and robust. Nonetheless, they are inefficient and suffer from load interference, where a load at an actuator can influence the behavior in other actuators.

An alternative to fixed displacement systems are constant pressure systems, which uses a variable displacement pump to provide a constant pressure to the hydraulic system. In constant pressure systems, the pressure at the hydraulic pump remains constant owing to the pressure-limiting valve. This eliminates the issue of load interference. However, they are not more efficient than open-center systems.

Both open center systems and constant pressure systems are considered as a valve-controlled system, where the centralized pump provides a constant flow or pressure, and the actuators are controlled using control valves. This type of system is inefficient because the pump has to be continuously operated at maximum pressure even if the control action is not required [88–90]. Moreover, they suffer from throttling losses that are inherent to resistance control [87].

Lastly, it has been mentioned in the literature that in conventional valve-controlled hydraulic systems, where hydraulic pressure or constant flow is supplied from a central hydraulic unit and controlled through a valve, the hydraulic unit runs continuously, even when not active, leading to a lower efficiency [85, 88–90].

1.4.2 Electrohydraulic Actuator

To improve the efficiency of traditional hydraulic systems, throttleless circuits have been proposed for eliminating the control valves and improving the power efficiency [87]. An example of a throttleless system is an electrohydraulic actuator (EHA) that incorporates all the hydraulic components, including the pump, motor, tank, and actuator in a single closed unit. The EHAs are pump-controlled; each unit can be independently activated as required, resulting in a higher power efficiency [77, 85, 88–90]. The EHA is a pump-controlled system, and pressurized fluid is only used for transmission between the motor and actuator. In robotic applications, EHAs are often utilized when smaller sizes and weight-to-power ratios are essential,

such as in prostheses or exoskeletons [84, 90].

In systems with a higher number of DoFs, all EHAs operate in parallel with each other. This is an advantage for aircraft applications when each actuator is positioned in a different part of the aircraft since piping from a centralized supply unit is then eliminated [88, 89]. On the other hand, in robots, where actuators are positioned close to each other, the weight of the piping is negligible. However, the redundant hydraulic components of each EHA, particularly pumps and motors, result in an excessive cost and weight of the entire system.

1.4.3 Alternating Pressure

Another throttleless hydraulic system is alternating flow hydraulics (AFH) [91, 92], which differs from traditional hydraulic systems by utilizing periodic alternating flow instead of unidirectional flow. The AFH system operates in a closed circuit, transmitting power without any net flow or throttling losses. This unique characteristic distinguishes AFH from conventional hydraulic systems. AFH often operates in a polyphase configuration, with three-phase being the most widely used. However, despite the absence of throttling losses, the efficiency of AFH is still relatively poor.

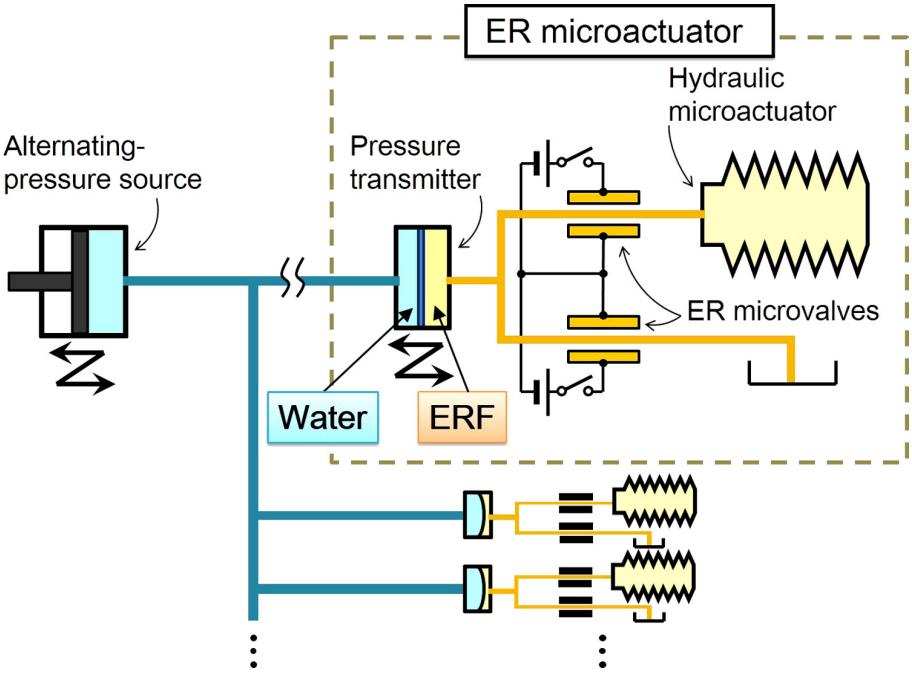

Figure 1.14: Schematic of an ER microactuator system with an alternating pressure source [93].

Recently, another type of alternating pressure system using an alternating pressure source with a synchronized valve system has been previously proposed for microactuators [93, 94]. In this system, an alternating pressure is supplied to all actuators simultaneously. Control valves, which are directly connected to the actuators, open and close in synchronization with the pump. For example, to elongate the actuator, the valve opens during the pressurized period and closes during the suction period. The schematic of the alternating pressure source is shown in Fig. 1.14.

With the alternating pressure system, the piping is simplified and only a simple on-off valve is required, rather than the complex 3/3 flow control valve required to achieve the same functionality as the traditional single-acting cylinder system. In both studies, an electro-rheological fluid, controlled with flexible electro-rheological microvalves, was utilized as the hydraulic fluid. They achieved independent motion of the two actuators. However, as the system was designed for a microactuator, its functionality as a hydraulic supply system is very limited: neither pressure nor volume can be controlled, and the input peak-to-peak pressure was only 110 kPa which is much lower than conventional hydraulic systems.

1.4.4 Hydraulic Fluid

Hydraulic fluid is a type of fluid used in hydraulic systems. Its primary function is to transmit power from the pump to the actuator in the hydraulic system. It is used to create pressure that drives the movement of the hydraulic components, such as cylinders, motors, and valves. The hydraulic fluid is pressurized by the pump and then directed to the hydraulic components through hoses, pipes, and valves. The fluid then creates a force that moves the actuator, producing the desired motion. Hydraulic fluid also provides several important functions, including lubrication, heat transfer, and protection against corrosion and wear. Hydraulic fluid can be made from a variety of materials, including mineral oils, synthetic oils, water, and water-based fluids.

Mineral oil, in particular, is the most popular hydraulic. It is typically used as a hydraulic fluid in high-pressure applications where efficiency and power output are crucial. Oil has excellent lubrication properties, which can reduce wear and tear on the system. Additionally, oil also provides good resistance to oxidation and

corrosion, which can prolong the lifespan of the system.

However, oil also has some disadvantages. It can be toxic and harmful to the environment if not disposed of properly. Oil is also hazardous to human: it can produce harmful vapors and fumes, and may cause irritation or burns when come into contact with skin or eye. Moreover, oil is notorious for being difficult to clean, making it unsuitable for wearable devices. Lastly, oil is also a major fire hazard [74, 95, 96].

Water, on the other hand, is often used as a hydraulic fluid in low-pressure applications where cost and environmental impact are important factors. First, high flow rate can be achieved with relatively small cross-sections without large pressure loss due to the low viscosity of water. Moreover, it is readily available and less expensive than oil. Water is also non-toxic and environmentally friendly, which makes it a popular choice for systems that operate in sensitive environments. Additionally, water does not produce harmful vapors or fumes, which can be beneficial for the safety of users [74, 95, 97, 98].

However, water has some disadvantages that must be considered. It can cause corrosion of metal components in the hydraulic system, which can lead to increased maintenance costs. Water also has poor lubrication properties, which can lead to increased wear and tear on the system. Lastly, water has a limited range of working temperature [74].

To summarize, mineral oil is commonly utilized in traditional hydraulic systems due to its exceptional lubrication properties, which reduce wear and tear on the system. Additionally, it offers good resistance to oxidation and corrosion, thereby extending the lifespan of the system. However, it poses hazards to human health by emitting toxic vapors and fumes, as well as causing irritation or burns. Moreover, mineral oil is challenging to clean effectively.

In contrast, water presents several advantages. It is easily accessible and available at a low cost. Furthermore, water is non-toxic, and any leakage will eventually evaporate without leaving behind dirty residues or increasing the risk of fire hazards. However, water has some drawbacks, including a tendency to promote corrosion and rust, inadequate lubrication properties, and a limited range of working temperatures.

For wearable robot applications where the device is intended to be in constant contact with a human and operate at lower pressures, water can be a superior choice due to its superior safety and ease of cleaning. Compared to oil-based hydraulic

fluids, water is non-toxic, which is essential for ensuring the safety of the user. Additionally, water is easy to clean with minimal effort, whereas mineral oil is notorious for being difficult to clean. These factors make water a suitable choice for wearable robot applications where safety and ease of maintenance are critical considerations. The main disadvantage of water which is corrosion can be easily avoided by selecting a suitable components.

1.5 Objective

The objective of this study is to address discomfort in knee exoskeletons caused by joint axis misalignment, excessive weight, and inertia, with the aim of assisting older people with ADLs. To achieve this goal, three approaches are taken:

1. Adoption of a crossed four-bar linkage mechanism instead of a simple revolute joint for the knee joint. While a revolute joint has a fixed ICR at the center of the joint, the ICR of a crossed four-bar linkage mechanism exists at the intersection of the links, creating a curved centrode that mimics the biomechanics of the human knee joint. This better approximation of knee biomechanics reduces misalignment due to kinematic incompatibility commonly found in exoskeletons.

2. Adoption of lightweight hydraulic actuators instead of electrical motors to minimize the added weight and inertia on the limb is an essential aspect of this study. Hydraulic actuators are known for their high power-to-weight ratio, which is orders of magnitude higher than that of electric motors. In particular, the rubber-based HAM used in this study exhibits a very high power-to-weight ratio even among other hydraulic actuators, contributing to a lighter exoskeleton and alleviating discomfort for the user. Moreover, the unique force-contraction characteristics of the HAM are exploited using the geometry of the linkage mechanism to generate the required torque profile to support ADLs.

3. Streamlining of hydraulic system components and reducing hydraulic energy loss for multi-DoF hydraulic systems. Traditional hydraulic systems typically require large, heavy, and inefficient hydraulic supply units, whereas EHAs

are more efficient but limited to one DoF. To address this issue, a novel hydraulic system utilizing channel switching for multi-DoF hydraulic systems has been proposed. This channel switching system eliminates the need for large and complex valves and return lines used for pressure and volume control, while also reducing inherent throttling losses associated with valve control systems. These improvements make hydraulic systems more suitable for multi-DoF wearable devices.

By incorporating these approaches, the study aims to enhance the comfort and usability of knee exoskeletons, particularly for older individuals during their daily activities.

The scope of this study is limited to the knee joint exoskeleton worn by the user. As such, the weight consideration does not include other components such as the power source, battery, pump, or hydraulic power unit. The focus is solely on the weight of the knee joint exoskeleton itself and its related support equipment, excluding the weight of external components required for the overall functioning of the system.

1.6 Thesis Structure

The structure of this thesis is organized as follows:

Chapter 1 gives the background of the research. The difficulties of the elderly during ADLs are briefly discussed. A brief summary of related assistive devices is presented, describing different approaches for ADL assistance and highlighting the advantages of robotics exoskeletons compared to previous approaches. The issues of current exoskeleton is also discussed, and potential solutions to the issues in the literature is also presented. Hydraulic systems for multi-DoF systems were also briefly discussed in the context of hydraulic-powered wearable exoskeletons. Lastly, the objectives of this research and the structure of this thesis is outlined.

Chapter 2 presents a single-DoF STS-assist exoskeleton, which utilizes a four-bar linkage mechanism and a HAM. The chapter serves as a proof-of-concept, demonstrating the effectiveness of combining the four-bar linkage mechanism and the HAM for STS assistance.

In Chapter 3, novel hydraulic control algorithms for multi-DoF hydraulic sys-

tems are introduced. These algorithms aim to enhance the capabilities of hydraulic-powered wearable devices. By increasing the number of supported degrees of freedom, the exoskeleton can provide assistance for a broader range of movements.

Chapter 4 builds upon the ideas proposed in Chapters 2 and 3. This chapter combines the concepts to develop a multi-DoF powered exoskeleton for SC assistance. The integration of the four-bar linkage mechanism, the HAM, and the hydraulic control algorithms results in an exoskeleton capable of providing assistance for sit-to-stand and other complex ADLs.

Chapter 5 summarizes the key findings of the thesis and discusses their implications. It provides a comprehensive overview of the research conducted and highlights the contributions made by the proposed approaches. Additionally, this chapter explores potential avenues for further research and development in the field of assistive robotics.

The relationship between each chapter is illustrated in Fig. 1.15.

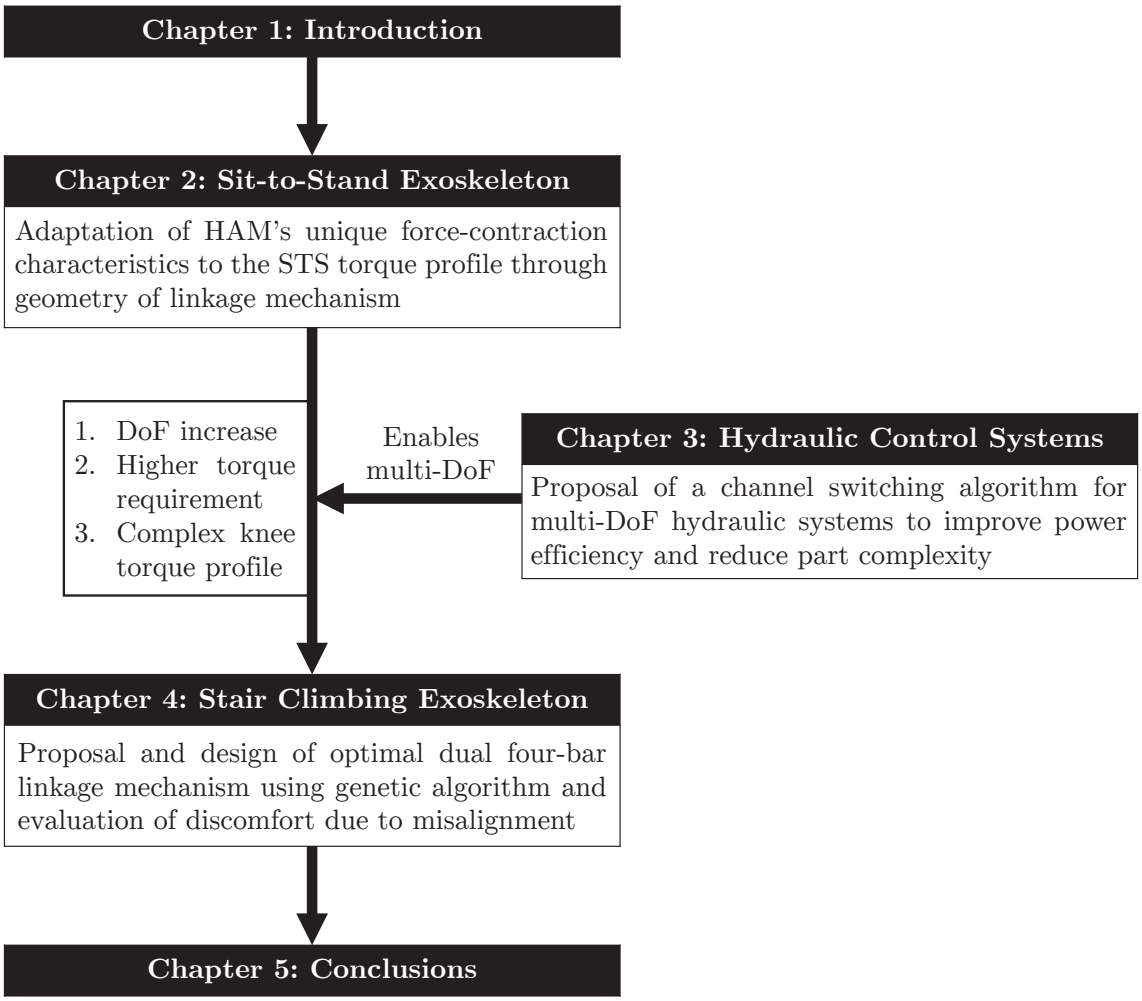

Figure 1.15: The relationship between chapters of this thesis.

1.7 Chapter Summary

Falls represent a significant health risk for older individuals, resulting in a high rate of morbidity and mortality. Many of these falls occur during ADLs, especially STS and SC, which has led to the development of various assistive devices. A promising technology for ADL assistance is exoskeletons. Studies have shown that they are effective at supporting various activities and are more mobile than traditional powered devices. However, there are differences between human biomechanics and exoskeletons, and the added weight and inertia can cause discomfort to the user. Accordingly, this thesis will study powered exoskeletons for ADL assistance with enhanced comfort by adopting an ergonomic mechanism for the knee joint to reduce human-robot misalignment, and reducing the weight of the proposed device by

adopting lightweight hydraulic actuators. Finally, a hydraulic system for multi-DoF exoskeleton with reduced hydraulic losses will be proposed.

Chapter 2

Sit-to-stand Exoskeleton

This chapter introduces a bioinspired STS-assist exoskeleton that utilizes an ergonomic four-bar linkage and HAM. The proposed device takes advantage of the distinctive force-displacement characteristics of the HAM and the geometries of the linkage mechanism to generate the necessary torque for an STS motion without relying on a complex control system. To evaluate the efficacy of the proposed device, two experiments were conducted. Firstly, the torque output of the device was measured to confirm its mechanical capabilities. Secondly, an experiment was performed on a participant to validate its effectiveness in assisting an STS motion. The work presented in this chapter was partially published in [99].

2.1 Device Proposal

2.1.1 Hydraulic Artificial Muscle

An actuator is an essential part of a powered wearable device that allows it to move and support the user. Other than power, weight and compliance are two main characteristics that are especially important in wearable applications. A heavy actuator will introduce additional inertia and moment of inertia to the user's limbs and either hinder the intended movement [37] or require a fast and complex control system to counteract. Previous studies have utilized Bowden cable [57, 58] and pneumatic artificial muscle [58, 63] with power units attached to the torso. Compliance is also very important to reduce rigidity and improve comfort. A compliant actuator will be intrinsically beneficial in this regard. For the reasons above, the HAM which has

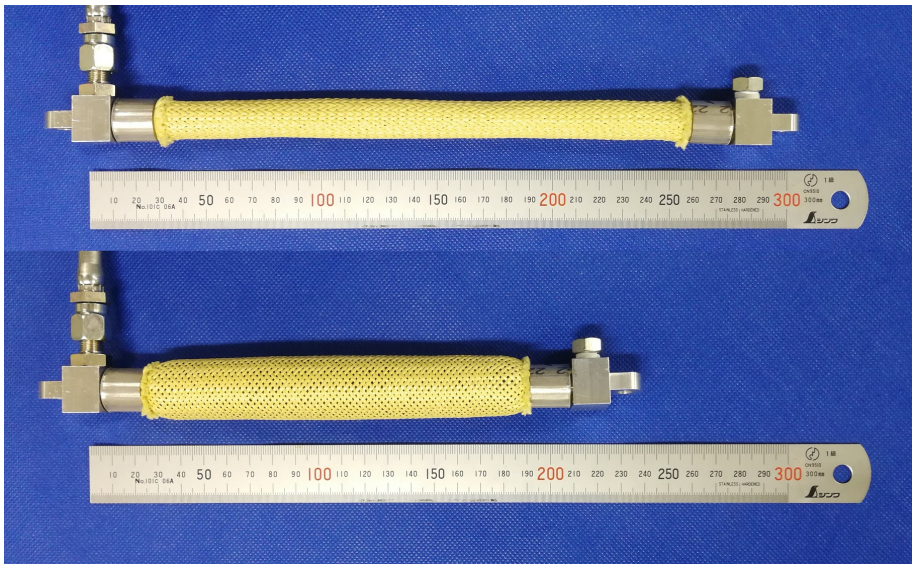

Figure 2.1: Photograph of a HAM with 25° braiding angle in the rest state and with 3 MPA applied pressure.

both of the desired characteristics is utilized.

A HAM, shown in Fig. 2.1, is a hydraulic contracting actuator. It is based on McKibben artificial muscle, which was first developed in the 1950s for use in artificial limbs and orthoses such as [100]. Compared to similar-sized hydraulic cylinders, a HAM's maximum output force is up to twice or thrice that of a cylinder while being much lighter due to being a hollow rubber shell. Its dynamic range is similar to that of a human muscle [101]. It is also compliant due to its main component being rubber, which makes it suitable for wearable and welfare applications.

A HAM consists of three main components: an outer sleeve, an inner rubber tubing, and fittings on both ends as shown in Fig. 2.2. The sleeve is the main component that converts radial expansion into axial contraction. When pressure is applied to the inner tube, it inflates radially while the length of each individual strands of the sleeve remain constants. Therefore, the braiding angle of the sleeve widens to accommodate the increased tubing radius and generates contraction in the axial direction

The HAMs used in this study have an outer tubing diameter of 11 mm, and a braiding angle of 25° and 30°. Other properties of the HAM are shown in Table 2.1.

Compared to earlier HAMs in the literature [72, 73], the HAM in this study operates at a comparable pressure while being significantly smaller at the cost of

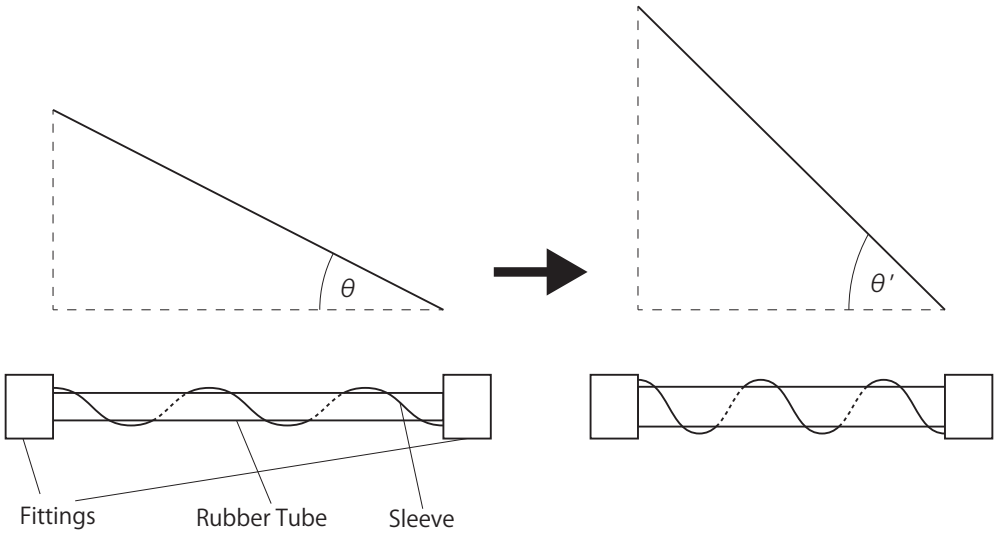

Figure 2.2: Diagram of a HAM in unpressurized and pressurized state. The radial expansion of the inner tube causes the braiding angle to widen, resulting in axial contraction.

Table 2.1: Properties of the HAM used in this section.

Parameter	Value
Rest length	220 mm
Maximum pressure	5 MPa
Maximum contraction ratio	29.5%
Inner tubing diameter	8 mm
Outer tubing diameter	11 mm
Sleeve Diameter	12 mm
Sleeve material	Kevlar
Initial braiding angle	25°, 30°
Dry weight (including fittings)	Approx. 160 g

having a lower contraction force. Both studies also used 25° and 30° braiding angles and obtained similar maximum contraction ratios. Both studies used Force Density per Mass (FDM) and Energy Density per Mass (EDM) functions [102] shown in Eq. 2.1 and Eq. 2.2 to evaluate the performance of the HAMs. While EDM is more suitable for the evaluation of HAMs due to contraction force being a function of contraction, FDM is also included for completeness.

Table 2.2: Comparisons of hydraulic actuators.

	This HAM	Morita et al. [73]	Mori et al. [72]	JIS Cylinder [73]
Diameter [mm]	12	17	40	40
Dry Weight [kg]	0.160	0.252	3.0	5.84
Stroke [mm]	66	120	140	120
Pressure [MPa]	5	5	4	21
Max Force [kN]	5.0	8.8	28	26.4
FDM [kN/kg]	15.6	17.5	4.67	4.52
EDM [kJ/kg]	0.52	1.05	0.327	0.542

$$\text{FDM} = \frac{F}{m} \tag{2.1}$$

$$\text{EDM} = \frac{1}{m}\int F dx \tag{2.2}$$

where:
F is actuator force,
m is mass of the actuator, and
x is stroke of the actuator.

Following [73], the mass of the HAMs is doubled to account for antagonistic configuration in bidirectional applications for FDM and EDM calculation. The HAM used in this study exhibited a similar FDM and lower EDM compared to [73]. However, their HAM is also roughly twice as long. This improves EDM as the weight of the fittings is constant regardless of its length. Full comparisons of hydraulic actuators are shown in Table 2.2.

Theoretical Model

The theoretical contraction force of an ideal HAM can be derived from the relationship between inflation pressure and the braiding angle of the outer sleeve. It was given by Schulte as a function of braiding angle with correction terms for tubing elasticity and internal frictions in [103] as follows:

$$\begin{aligned} F =& \frac{\pi D^2 P}{4}\left(3\cos^2\phi - 1\right) + \pi D k_e \left(l\sin\phi - \frac{\pi\cos^2\phi}{\sin\phi}\left(D\sin\phi - d_0\right)\right) \\ & - \pi L D (P - P_i)\left(u_s + u_{st}\right)\sin\phi \end{aligned} \tag{2.3}$$

where:

F is contraction force,

ϕ is braiding angle,

D is diameter of tubing when $\phi = 90°$,

P is internal pressure,

k_e is elastic constant of the inner tubing,

l is length of the artificial muscle,

d_0 is diameter of tubing at rest length,

u_s is coefficient of friction between the strands of the helical sleeve,

u_{st} is coefficient of friction between the strands of the sleeving and the inner tube, and

P_i is pressure required to inflate the unconstrained inner tube to a diameter equivalent to the device diameter at any value of ϕ.

However, Schulte also noted in his work that "Unfortunately, the terms contain factors that are ϕ dependent; k, u_s, and u_{st} are probably nonlinear, and somewhat difficult to determine experimentally."

Ignoring the correction terms, Eq. 2.3 can also be rewritten as a function of contraction as

$$F = \frac{\pi {d_0}^2 P}{4} \frac{1}{\sin^2 \phi_0} \left(3 \left(1 - \varepsilon\right)^2 \cos^2 \phi_0 - 1\right), \tag{2.4}$$

where:

ϕ_0 is initial braiding angle, and

ε is contraction ratio.

The maximum theoretical contraction is found at $\phi = \arctan \sqrt{2}$ or 54.74° regardless of the initial braiding angle [104]. This is because at this angle, the HAM has the maximum volume; contracting the HAM beyond this point produces negative theoretical contraction force. In reality, the HAM buckles beyond maximum contraction length and becomes unpredictable. The maximum contraction $\varepsilon_{\max}$ is given by

$$\varepsilon_{\max} = 1 - \frac{1}{\sqrt{3} \cos \phi}. \tag{2.5}$$

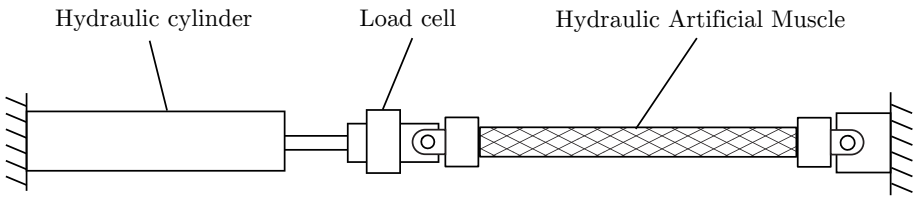

Figure 2.3: Experiment setup of HAM force-contraction relationship experiment.

The maximum contraction force is found at rest length and can be found by equating $\varepsilon = 0$ which results in

$$F = \frac{\pi {d_0}^2 P}{4} \left(\frac{3}{\tan^2 \phi_0} - \frac{1}{\sin^2 \phi_0} \right). \tag{2.6}$$

Experimental Data

An experiment was conducted to measure the actual contraction force relationship of the HAM. The HAM was initially fixed on one end, and the other end was fixed to a load cell, which is fixed to a hydraulic cylinder rod as shown in Fig. 2.3. The experimental methodology is as follows:

1. The hydraulic cylinder rod is adjusted so that the HAM is at its neutral length.
2. Hydraulic pressure is applied to the HAM.
3. The hydraulic cylinder is extended until the measured contraction force is reduced to zero.
4. The hydraulic cylinder contracts to its initial length.
5. The hydraulic cylinder is extended again until the contraction force reduces to zero.

The comparisons between theoretical and experimental force output are shown in Fig. 2.4. It can be seen that the maximum contraction force predicted by the simplified Schulte's model agrees well with the experiment results especially at higher pressure, where the effect of tube elasticity is minimized. However, as the simplified model completely disregards the inner rubber tube, it cannot explain why maximum contraction increases with pressure, or the discrepancy between theoretical

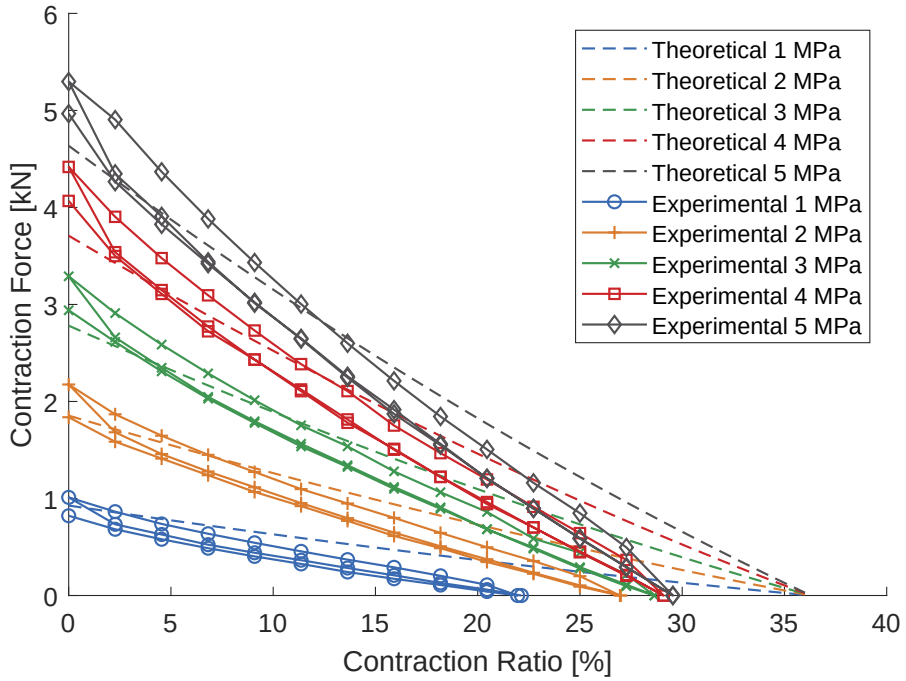

Figure 2.4: Theoretical and experimental $F - \varepsilon$ relationship of the 25° HAM.

and experimental contraction ratio. Furthermore, it cannot explain the different stress-strain curves between loading and unloading of the HAM, which stems from rubber elastic hysteresis.

Rubber is a material with unique properties such as a high degree of deformability, nonlinear stress-strain curve, incompressibility, and hysteresis due to internal friction [105]. These characteristics, especially hysteresis, results in minor deviations from the ideal theoretical model. When the HAM is fixed at rest length and hydraulic pressure is applied, the first cycle will have a relatively lower contraction force due to virgin hardness of the rubber [106]. Later cycles exhibit constant hysteresis curve until pressure is released.

Braiding Angle

From Eq. 2.4, it can be inferred that parameters that affect maximum contraction force are pressure, diameter, and initial braiding angle. The initial braiding angle, in particular, also affects the maximum contraction ratio. The effects of the initial braiding angle are shown in Fig. 2.5 and Fig. 2.6.

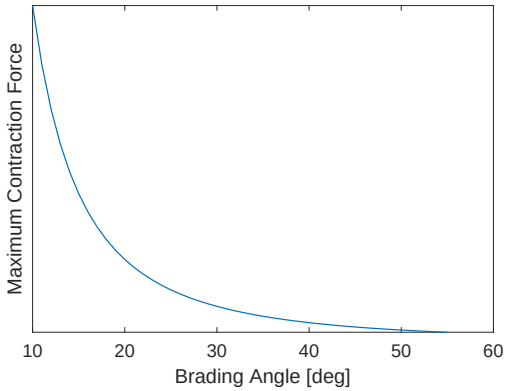

Figure 2.5: Relationship between maximum contraction force and braiding angle.

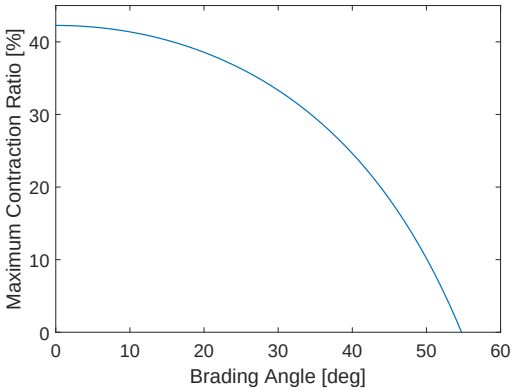

Figure 2.6: Relationship between maximum contraction ratio and braiding angle.

Figure 2.7: Photograph of both HAMs. The 25° HAM is shown on top, and the 30° HAM is shown on the bottom.

In theory, a HAM with a smaller initial braiding angle is expected to generate a higher contraction force and contraction ratio. In practice, a HAM with a wider braiding angle tends to be more durable and able to withstand higher pressure. The wider angle provides more robustness and structural stability to the muscle, making it less prone to damage or failure. Conversely, a contraction ratio that is too small may not be feasible in practical applications due to lower durability and other issues such as ballooning.

Two HAMs with similar materials and constructs were examined to verify the effects of the initial braiding angle. The contraction force was measured with the HAMs fixed at rest length. Both HAMs started leaking at the fittings crimp above 5 MPa. Hence, the HAM with 25° braiding angle was selected for application in the proposed device due to higher force output and larger range. The relationships between contraction forces and pressure are shown in Fig. 2.8.

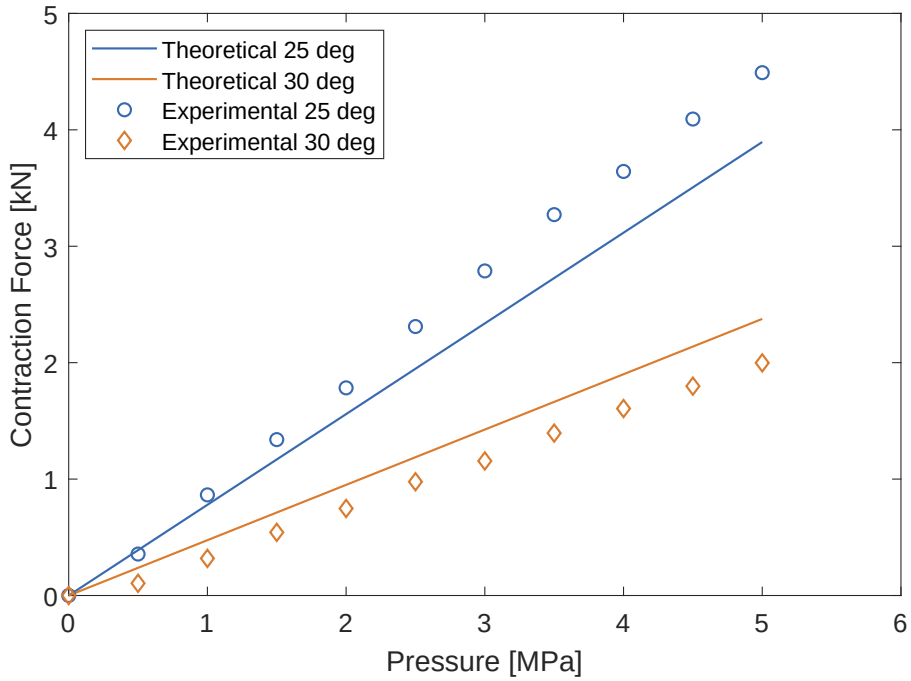

Figure 2.8: Relationships between contraction force and pressure at rest length of HAMs with 25° and 30° initial braiding angle during inflation.

Sleeve Looseness

Another inconsistency between the theoretical model and experimental results is the maximum contraction ratio. This also happened in many studies in the literature, which cited friction between the sleeve and the rubber tube as the factor preventing the braiding angle from reaching the critical angle of 54.74° [106]. However, in the experiment, the braiding angle of 54° was reached at maximum contraction. This contradicts with previous literature, and another explanation is needed.

One possible reason why the theoretical model overpredicts the maximum contraction may be the looseness in the sleeve; it is not in a stretched condition in the rest state, and the effective diameter of the sleeve may be larger as shown in Fig. 2.9. This also affects the maximum contraction ratio, as the effective initial braiding angle will also be larger, resulting in a lower maximum contraction ratio as explained in the previous section. While the increased radius has a positive impact on contraction force, it is offset by the increased braiding angle, resulting in reduced contraction force.

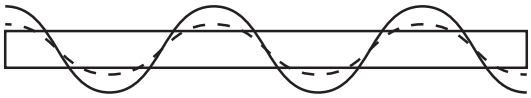

Figure 2.9: Designed and real sleeve of a HAM. The dashed line represents the ideal sleeve, whereas the solid line represents a slacked sleeve in a real HAM.

To find the effective diameter, the outer diameter of the HAM with applied pressure was measured both when fixed at neutral length and without load. At neutral length, the measured diameter was 18 mm. At 29.5% contraction, the outer diameter increased to 26 mm.

The turn number of an ideal HAM can be found through a geometric relationship between length, diameter, and braiding angle as shown in Eq. 2.7

$$n = \frac{l_0 \tan \phi_0}{\pi d_0} \tag{2.7}$$

where:

n_t is number of turns a sleeve strand makes around the HAM throughout its length, and

l_0 is the rest length of the device.

In a real HAM where the sleeve is loose, the braiding angle widens to accommodate the added length of the sleeve, whereas the turn number stays constant due to being fixed by the fittings at both ends. Substituting the measured effective diameter into Eq. 2.7, the effective initial braiding angle can be found as follows.

$$\phi_e = \arctan\left(\frac{d_e \tan \phi_0}{d_0}\right) \tag{2.8}$$

where:

ϕ_e is effective braiding angle, and

d_e is effective diameter of tubing at rest length

Alternatively, the effective braiding angle can also be calculated from the maximum contraction ratio. Assuming the braiding angle of the HAM at maximum contraction is 54.74°, the length of a sleeve strand is

Table 2.3: Comparisons between the ideal model, the loose sleeve model, and experiment results for HAM with 25° braiding angle.

Model	Ideal	Sleeve	Experiment
Maximum contraction force (kN)	4.64	3.96	4.49
Maximum contraction ratio (%)	36.3	29.8	29.5
Diameter at rest length (mm)	12.5	17.8	17.8
Diameter at maximum contraction (mm)	23.2	25.6	26.0
Braiding Angle	25°	34.67°	N/A

$$s_e = \left(\frac{l_0}{\cos\phi_0}\right)\left(\frac{1-\varepsilon_{\max}}{1-\varepsilon_{\max,e}}\right), \tag{2.9}$$

where:

s_e is length of a sleeve strand, and

$\varepsilon_{\max,e}$ is measured maximum contraction ratio.

The effective braiding angle and diameter can then be calculated as shown in Eq. 2.10 and 2.11

$$\phi_e = \arccos\left(\frac{l_0}{s_e}\right) \tag{2.10}$$

$$d_e = \frac{s_e \sin\phi_e}{n\pi} \tag{2.11}$$

The force-contraction relationship and the maximum contraction force with sleeve looseness can be found by substituting ϕ_e and d_e into Eq. 2.4 and Eq. 2.6. Comparisons between the ideal model, the loose sleeve model, and experiment results for 25° and 30° braiding angle are shown in Table 2.3 and 2.4.

It can be seen that the loose sleeve model gives a more accurate prediction for both HAMs. Naturally, as the loose sleeve model also ignores the rubber tune similar to the ideal model, other characteristics such as hysteresis are still not accounted for.

Table 2.4: Comparisons between the ideal model, the loose sleeve model, and experiment results for HAM with 30° braiding angle.

Model	Ideal	Sleeve	Experiment
Maximum contraction force (kN)	2.83	2.27	2.00
Maximum contraction ratio (%)	33.3	25.6	23.4
Diameter at rest length (mm)	12.5	16.9	16.9
Braiding Angle	30°	39.11°	N/A

2.1.2 Polycentric Joint

Several biomechanical compliant knee joint mechanisms have been explored in Chapter 1. In this section, a knee joint mechanism based on the four-bar linkage is selected for its simplicity and weight-bearing capability. Moreover, a rigid mechanism is preferable as the HAM is a contracting actuator, and connecting a HAM to an unconstrained joint may result in slippage or unnecessary load to the human knee joint.

Various types of four-bar linkage knee mechanisms have been previously proposed with different design goals such as improving knee stability for the prosthesis [50]. A biomimetic joint was proposed in [51] by emulating ACL and PCL ligaments. The authors analyzed the lengths of the ligaments and concluded that it is reasonable to model them as stiff bars. The concept was then further developed in [52] by using a recursive optimizing method to adjust linkage lengths and recreate the shape of the condyle.

The four-bar linkage mechanism has a curved centrode which is a better approximation of the human knee compared to revolute joint with a fixed ICR. The centrodes of the mechanism proposed in [51] and [52] from 0° to 110° are calculated and shown in Fig. 2.10 for comparison purposes. The centrode for both mechanisms can be calculated using the same equations, which will be explained in detail in Section 2.2.2.

In this thesis, a four-bar linkage based on the design proposed in [52] is adopted.

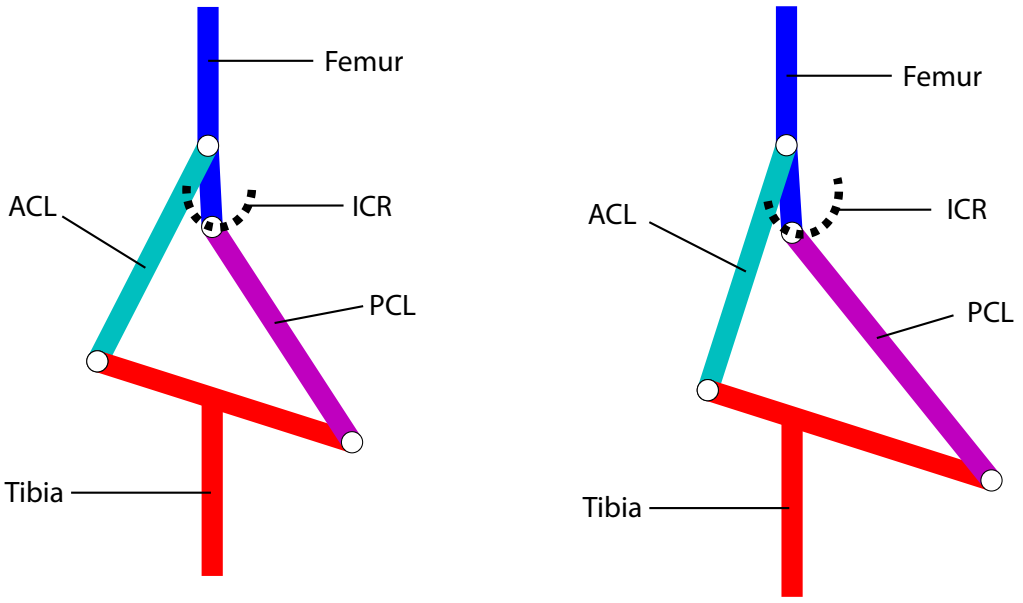

(a) The four-bar linkage proposed by Zavatsky et al. [51].

(b) The four-bar linkage proposed by Karami et al. [52].

Figure 2.10: Knee centrodes of the Zavatsky and Karami models. The ICR moves from left to right, and its paths are shown as black dotted lines.

2.1.3 Outline of the Proposed Mechanism

In this chapter, a bioinspired knee orthosis is proposed. Mechanisms utilized in the device operates in the same fashion as real human knee joint. First, the ligaments in the knee are replicated with a four-bar linkage. Second, the quadriceps femoris muscles are replicated with a HAM. The HAM is placed on the anterior side of the thigh alongside the femur, similarly to a real human leg.

The outline of the device is shown in Fig. 2.11. The modifications to the previous mechanisms are as follows. First, the femur part, shown in blue in Fig. 2.11, was extended along the length of the human thigh and in the anterior direction to improve the torque generated by the HAM. Next, the tibia part, shown in red, was incorporated with the Angled Bar to adjust and increase the generated torque similar to the patella in the human knee. Finally, the HAM, shown as the yellow line, is connected between the hip and shank to act as an extensor.

To simplify the control system, only a constant pressure will be applied to the HAM. Torque output of the device will be obtained through the geometry of the

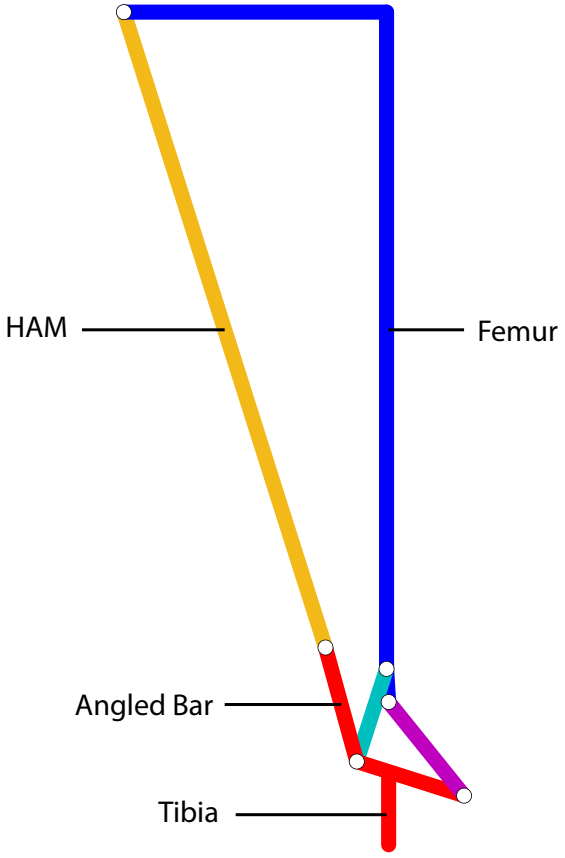

Figure 2.11: Outline of the proposed device.

device and the characteristics of the HAM. The design of the device, particularly the optimal values of each dimension will be discussed in detail in Section 2.2.2.

2.2 Mechanism Design

In this section, the design process of the proposed device is explained. First, modeling and calculation of the human body and STS action are discussed. The required torque as a function of the position of the knee joint was calculated. Second, the Angled Bar is proposed, and the effects of each design parameters are examined. Next, to find the optimal values for parameters discussed previously, analytical and numerical methods are explored. Finally, the designing process of the real device is explained.

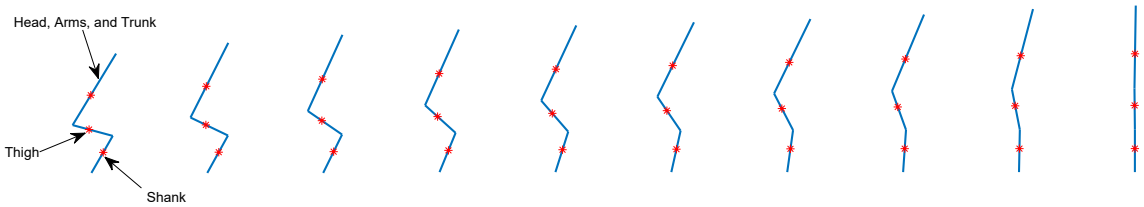

Figure 2.12: STS model used in this study. The red asterisks show the center of mass of each link.

Table 2.5: Body parameters [107, 108].

Section	Length [m]	Mass [kg]	I [kg cm^2]	CoM [m]
HAT	0.8494	44.00	25404	0.3553
Thigh	0.4222	20.72	3998	0.2491
Shank	0.4340	6.32	742	0.2405

2.2.1 Sit-to-Stand Model

To obtain the torque at the knee joint during STS to be used as a design target, the STS model was developed based on data from the literature. First, the reference male human body was modeled as three rigid bars. Next, joint angular positions approximations as a function of time based on positional data in the literature were used to calculate position as a function of knee joint angle. Finally, the torque developed in each joint was calculated through inverse dynamics equations.

The body was modeled as three rigid bars in a serial RRR configuration as shown in Fig. 2.12. Body parameters were based on data published in [107, 108]. Namely, the male body model with 73.0 kg weight and 1.741 m height was used. The arms in the head, arms, and trunk (HAT) section were modeled as folded across the chest. The values for each parameter are given in Table 2.5. Center of Mass (CoM) is measured from the previous section.

Next, kinematics model was calculated. Ankle and knee joint trajectories were modeled as cubic polynomials in joint space with initial and final positions based on data published in [12]. The hip angle was then calculated so that CoM is directly over the heel at all times. The resulting joint positions as functions of time are shown in Fig. 2.13.

The minimum torque required for STS can be calculated as torques required to

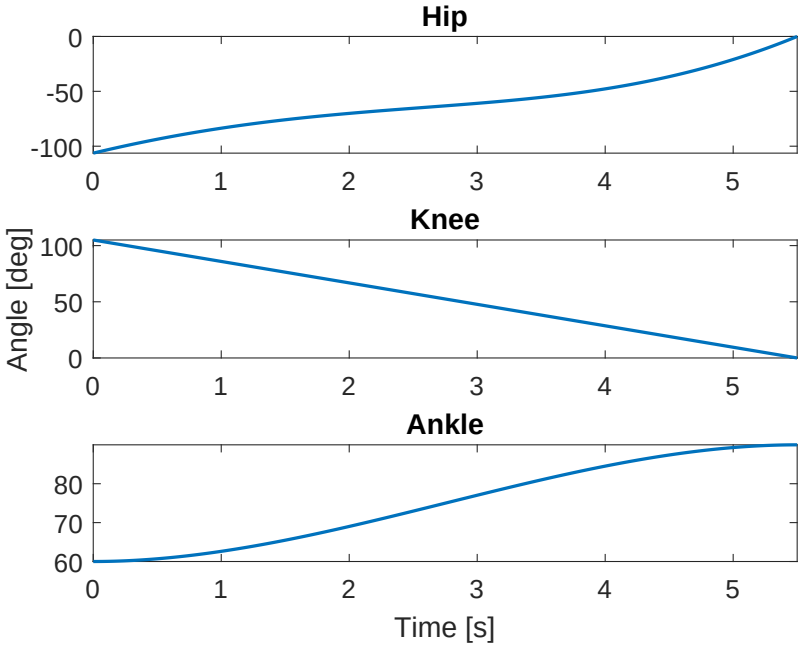

Figure 2.13: Ankle, knee, and hip joint positions as functions of time in natural STS motion.

offset torque due to gravity, while torque required for STS action at natural speed can be calculated using Newton-Euler equations. However, the torque due to angular velocity and angular acceleration were found to be negligible and have minimal effect on the overall torque. This shows that the method of normalizing STS torque using body mass employed in earlier studies was a reasonable approximation.

The maximum knee joint torque was 72.49 Nm per leg at seat-off and decreased as the joint angle became larger. This translates to 0.99 Nm/kg body mass per leg or 1.14 Nm kg^{-1} m^{-1} with respect to body-weight times height. The model agreed with the literature, which reported a peak of 0.9 Nm/kg body mass per leg [11] or 1.17 Nm kg^{-1} m^{-1} with respect to body-weight times height [109], and maximum torque is reached at seat-off [11, 12, 109, 110]. The resulting torques are shown in Fig. 2.14.

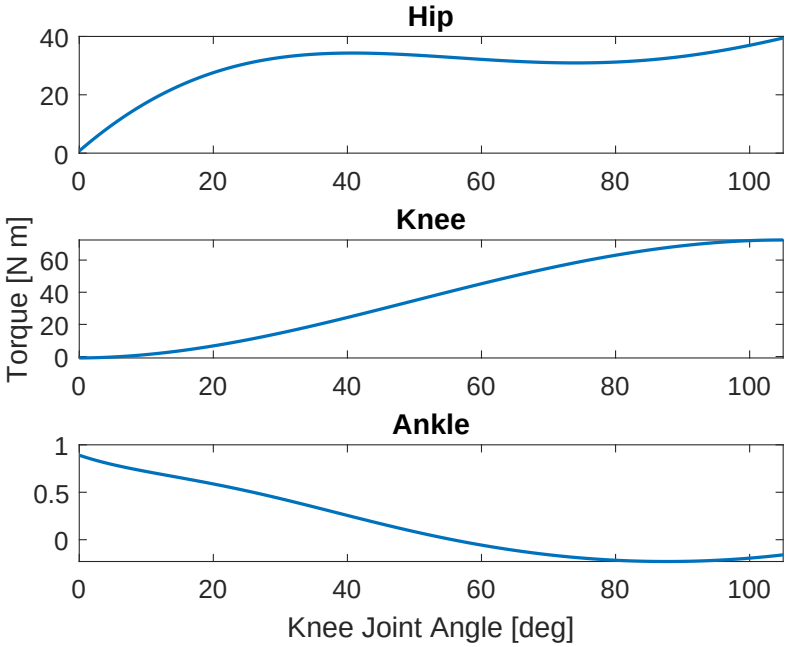

Figure 2.14: Ankle, knee, and hip joint torque as functions of knee joint position in natural STS motion.

2.2.2 Angled Bar

While it is possible to simply attach the HAM to the four-bar linkage, the resulting device will have poor performance for two main reasons. First, the torque output will be low due to the short "lever" vector. In this regard, the Angled Bar is functionally similar to the patella in the human knee. Second, as the knee moves in flexion direction, the HAM also moves closer to the ICR of the shank until it crosses over as shown in Fig. 2.15, which results in negative torque output.

To increase the torque output and improve the active range of motion, the Angled Bar is proposed. Link BC is extended to point E, where it is attached to the HAM as shown in Fig. 2.16. The bar is angled by ψ to adjust the shape of the output torque curve and improve the range of motion.

First, let us examine the linkage mechanism. Let point A be the origin of the coordinate system, with the knee joint angle defined as 0° at full extension, and increases in the flexion direction.

The difference between the knee joint angle θ_{knee} and θ_2 is equal to the initial

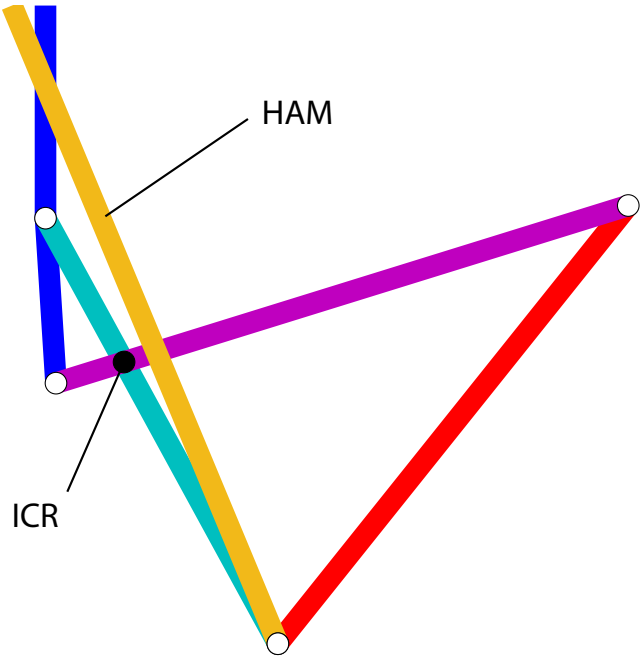

Figure 2.15: Positions of the HAM and linkages without the Angled Bar at 70° knee joint angle. The HAM crosses over the ICR of the knee joint, generating negative torque. The anterior direction is to the left.

angle of θ_2 at $\theta_{\text{knee}} = 0°$, which is defined as $\theta_{2,0}$.

$$\theta_{\text{knee}} = \theta_2 - \theta_i \tag{2.12}$$

The angle θ_1 as a function of θ_2 can be found from a solution of Eq. 2.13.

$$(K_1 - K_2)\tan^2\left(\frac{\theta_1}{2}\right) - 2K_3\tan\left(\frac{\theta_1}{2}\right) + K_1 + K_2 = 0 \tag{2.13}$$

where:

r_1 is length of link AB,
r_2 is length of link BC,
r_3 is length of link CD,
K_1 is ${r_3}^2 - {r_1}^2 - (x_D - r_2\cos\theta_2)^2 - (y_D - r_2\sin\theta_2)^2$,
K_2 is $2\,r_1\,(x_D - r_2\cos\theta_2)$, and
K_3 is $2\,r_1\,(y_D - r_2\sin\theta_2)$

which will allow the x and y coordinates of points B, C, and E to be obtained at any given θ_2 value, where l_1 is length of the Angled Bar.

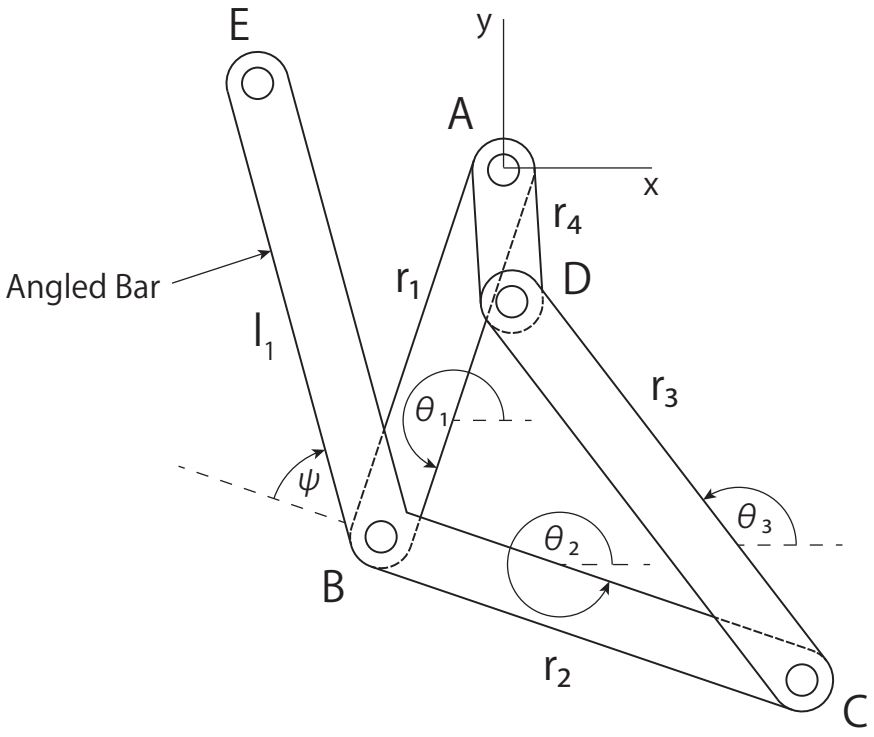

Figure 2.16: The four-bar linkage knee mechanism with the Angled Bar.

$$x_B = x_A + r_1 \cos\theta_1 \tag{2.14}$$

$$y_B = y_A + r_1 \sin\theta_1 \tag{2.15}$$

$$x_C = x_B + r_2 \cos\theta_2 \tag{2.16}$$

$$y_C = y_B + r_2 \sin\theta_2 \tag{2.17}$$

$$x_E = x_B + l_1 \cos(\theta_2 + \pi + \psi) \tag{2.18}$$

$$y_E = y_B + l_1 \sin(\theta_2 + \pi + \psi) \tag{2.19}$$

The ICR of link BC, which is also the ICR of the shank, is located at the intersection [111] between link AB and CD.

$$x_{\mathrm{ICR}} = \frac{(x_A y_B - y_A x_B)(x_C - x_D) - (x_A - x_B)(x_C y_D - y_C x_D)}{(x_A - x_B)(y_C - y_D) - (y_A - y_B)(x_C - x_D)} \tag{2.20}$$

$$y_{\mathrm{ICR}} = \frac{(x_A y_B - y_A x_B)(y_C - y_D) - (y_A - y_B)(x_C y_D - y_C x_D)}{(x_A - x_B)(y_C - y_D) - (y_A - y_B)(x_C - x_D)} \tag{2.21}$$

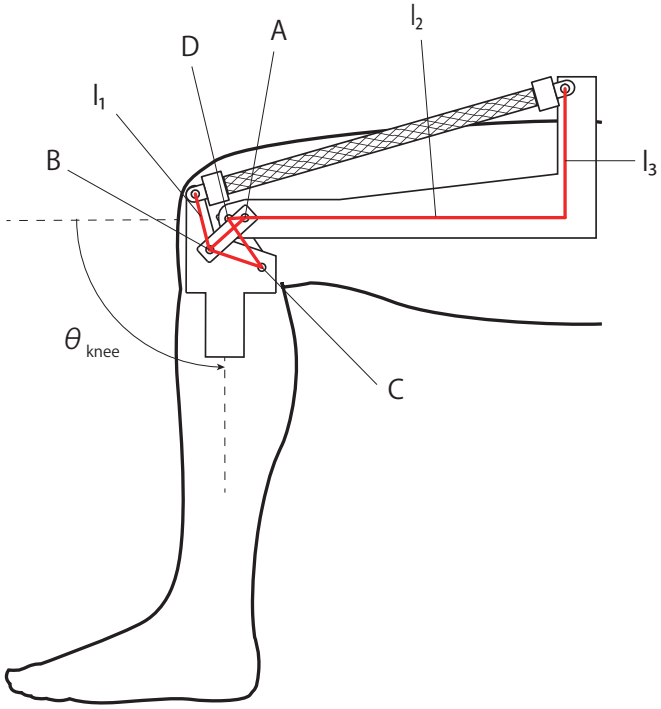

Figure 2.17: Drawing of the device imposed on a human leg.

A HAM is attached between the knee and hip on the anterior side of the thigh, similar to the quadriceps muscles which act as extensor in the human knee joint as shown in Fig. 2.17. The torque output, T, of the device can then be calculated using the coordinates of both ends of the HAM and ICR.

$$T = F\frac{|(l_2 - y_E)x_{\mathrm{IC}} - (l_3 - x_E)y_{\mathrm{IC}} + l_3 y_E - l_2 x_E|}{\sqrt{(l_2 - y_E)^2 + (l_3 - x_E)^2}} \tag{2.22}$$

where l_2 and l_3 are y and x coordinates of the fixed and of the HAM, respectively.

From Fig. 2.16 and Fig. 2.17, parameters that affect the performance of the device are l_1, l_2, l_3, and ψ. The effects of each parameter are discussed below.

Parameter l_1 corresponds to the length of link BE in Fig. 2.16. Since torque is the cross product of position vector and force vector increasing the length of l_1 also increases the length of the position vector, which results in larger torque output. Moreover, longer l_1 also results in a wider range of motion. However, the maximum length of l_1 is limited by the stroke of the actuator, therefore the optimal l_1 value also depends on other variables.

Parameter l_2 and l_3 correspond to the thigh segment of the device. The optimal

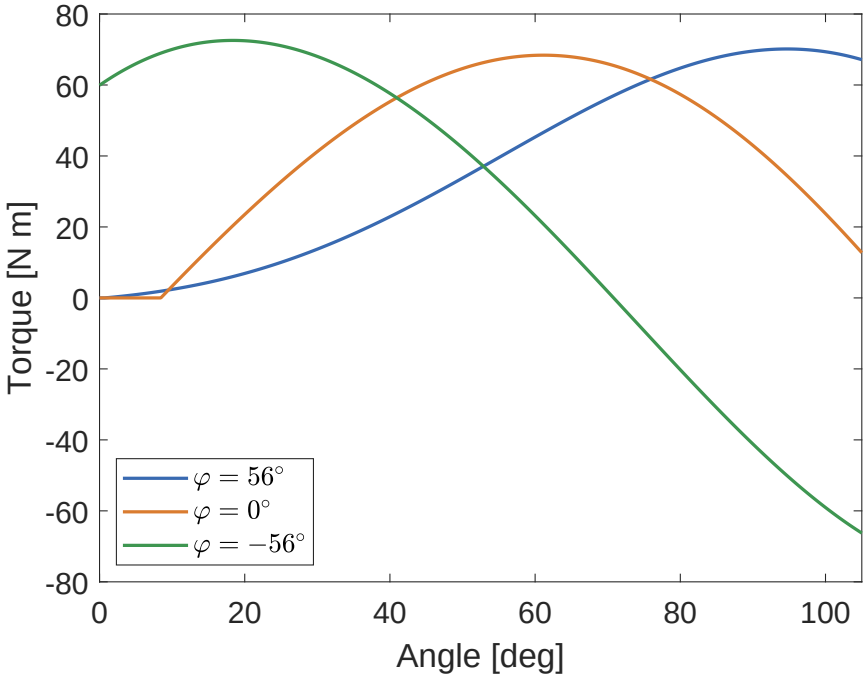

Figure 2.18: Resulting torque curve with positive, negative, and zero ψ values.

l_2 value largely depends on the length of the HAM. l_3, on the other hand, should be maximized to prevent the HAM from crossing the IC.

Lastly, parameter ψ corresponds to the initial angle of the Angled Bar. It determines the perpendicular distance between point E and ICR, which is correlated to the shape of the output torque curve as illustrated in Fig. 2.18. Generally, positive ψ values lead to torque curve peaks at larger joint angles, whereas negative ψ values lead to opposite results.

2.2.3 Artificial Muscle Model

As discussed in Section 2.1.1, the force-contraction relationship of the HAM predicted using theoretical models are inaccurate and do not account for hysteresis. However, as the proposed device is designed to operate at constant pressure, it is possible to approximate the HAM's force-contraction relationship as a linear function. Therefore, for design purposes, a least-squares regression was performed on the unloading contraction force curve to find the linear relation at a particular pressure. Both the loading and initial curves are ignored as the device is designed to utilize

the unloading part alone.

$$F = \beta_0 + \beta_1 \varepsilon + e \tag{2.23}$$

where:

β_0 is vertical intercept, or the maximum contraction force,

β_1 is regression coefficient, and

e is regression error term.

The maximum contraction ratio of the HAM is found at x-intercept

$$\varepsilon_{\max} = -\frac{\beta_0}{\beta_1} \tag{2.24}$$

Stiffness beyond maximum contraction ratio was ignored due to unpredictably in buckling, and the force output was assumed to be zero. This also prevents the optimization method from using the HAM as an extending actuator. Finally, the force-contraction relationship of the HAM used during the design process is described by Eq. 2.25.

$$F(\varepsilon) = \begin{cases} \beta_0 + \beta_1 \varepsilon & \text{if } 0 \leq \varepsilon < \varepsilon_{\max} \\ 0 & \text{if } \varepsilon \geq \varepsilon_{\max} \end{cases} \tag{2.25}$$

Contraction force beyond rest length was undefined. The force-contraction ratio relationship of the modeled HAM is shown in Fig. 2.19

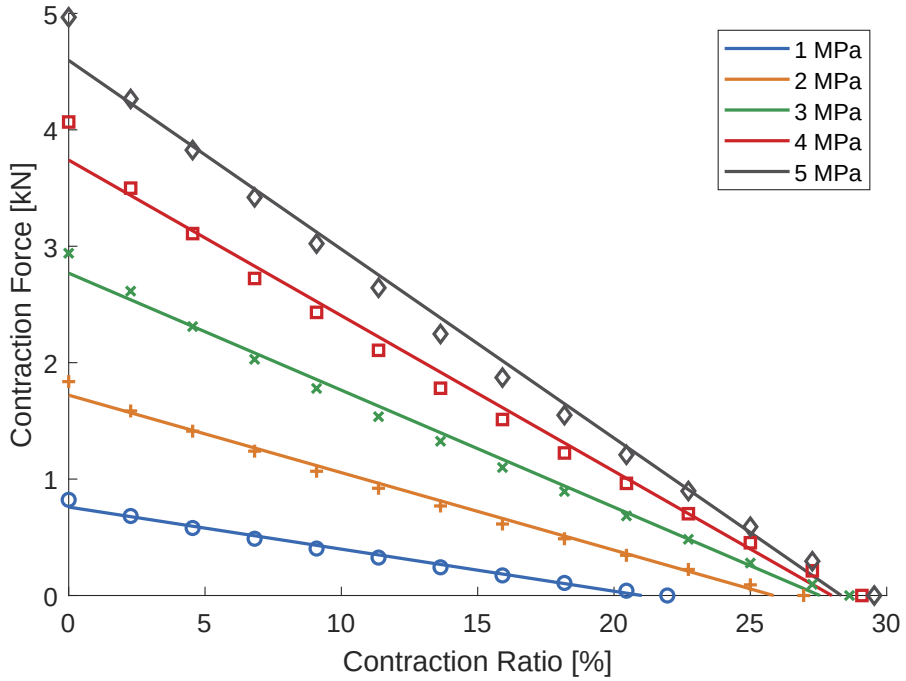

Figure 2.19: $F - \varepsilon$ relationship of the HAM used during the design process.

2.2.4 Optimization

The torque output of the device (T) can be rewritten as a function of θ_{knee} by substituting the values of each point as a function of θ_{knee} into Eq. 2.22. The contraction force (F_{HAM}) can also be approximated as a function of contraction, which can be calculated from the rest length of the HAM, the regression coefficients β_0 and β_1, and the position of point E.

$$T = f(\theta_{\text{knee}}, l_1, l_2, l_3, \psi, l_0, \beta_0, \beta_1) \tag{2.26}$$

The required torque obtained from the STS model can also be expressed as a function of θ_{knee} and body parameters. This enables the use of an optimization method to optimize the design parameters of the Angled Bar. While other algorithms such as Gradient Descent can also be utilized to find a local minimum, Grid Search was selected due to the low number of parameters, and it is guaranteed to converge to the global minimum given an appropriate grid size. The cost function utilized was root-mean-square error (RMSE), which was defined as

$$\text{RMSE} = \sqrt{\frac{1}{n}\sum_{i=1}^{n}(T_{\text{req},i} - T_i)^2}. \tag{2.27}$$

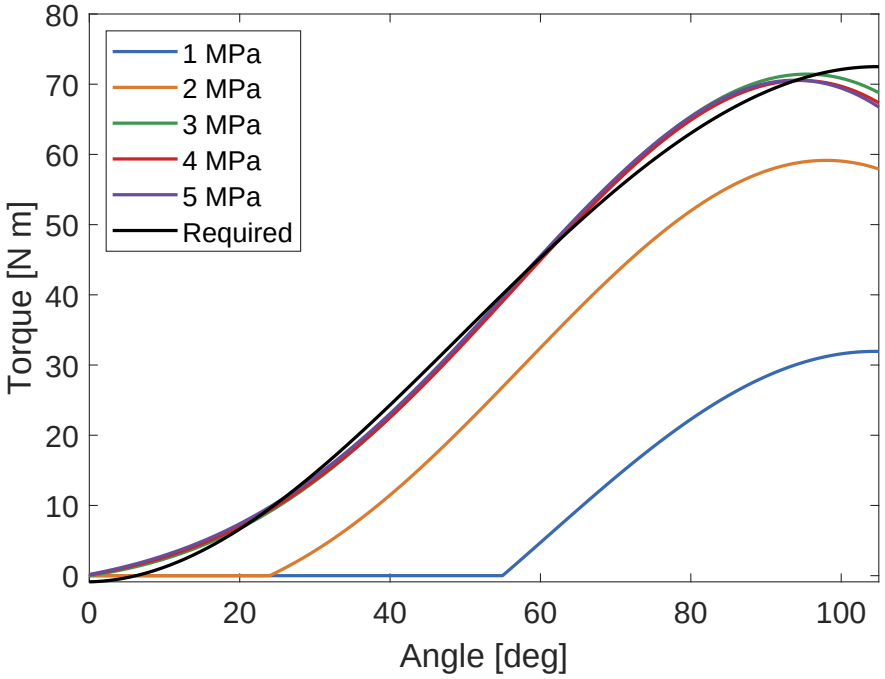

Figure 2.20: Optimal torque output results found through numerical analysis at 2 MPa, 3 MPa, 4 MPa, and 5 MPa.

where:

n is number of sampled points,

$T_{req,i}$ is required torque at knee joint shown in Fig. 2.14 at point i, and

T_i is torque generated using selected parameters at point i.

Every integer values of l_1, l_2 and l_3 within the interval [0, 100], [250, 350], and [0, 100] mm respectively were used. The maximum l_3 value of 100 mm was given due to design constraints. The upper limit of ψ was found analytically and ψ between 0° to 71° were utilized.

Optimal values were found for hydraulic pressures of 2 MPa, 3 MPa, 4 MPa, and 5 MPa. Results above 3 MPa showed no significant improvements as illustrated in Fig. 2.20, thus 3 MPa was selected safety, reliability, and lower pump requirements. Each parameter's effect on the RMSE is shown in Fig. 2.21-2.24.

In addition, a similar designed method was also performed with hydraulic cylinders as actuators. Two cylinders were modeled for comparisons. First, a hydraulic cylinder with an 11 mm piston diameter, which is the same size as the HAM's initial diameter, operated at 3 MPa. For simplicity, the piston rod was ignored, which

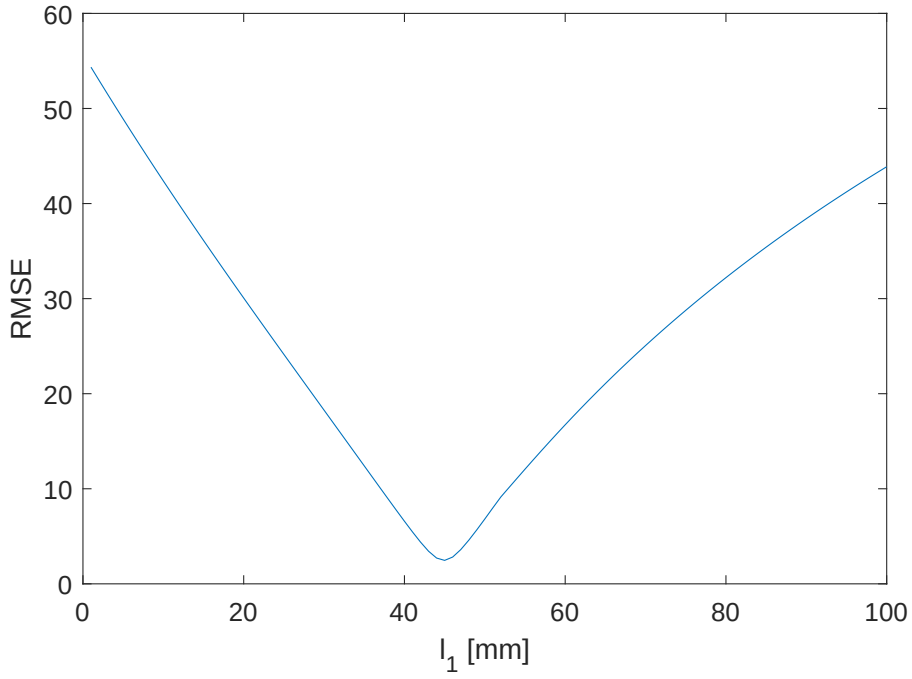

Figure 2.21: The RMSE about optimal point with different l_1.

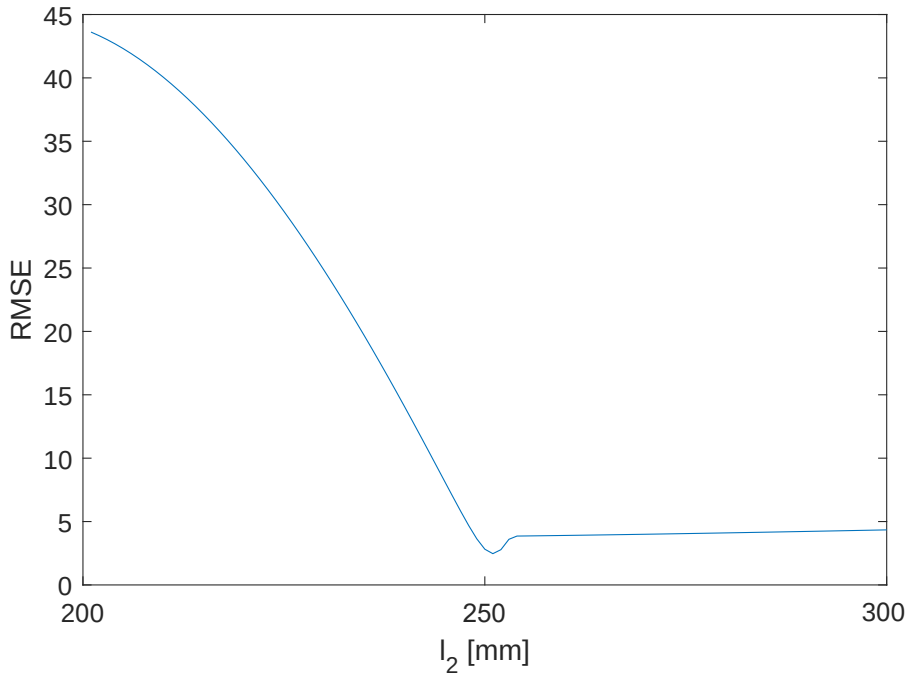

Figure 2.22: The RMSE about optimal point with different l_2.

results in 285 N constant contraction force. Second, a hydraulic cylinder with a constant 2769 N contraction force, which is equal to the HAM's maximum contraction

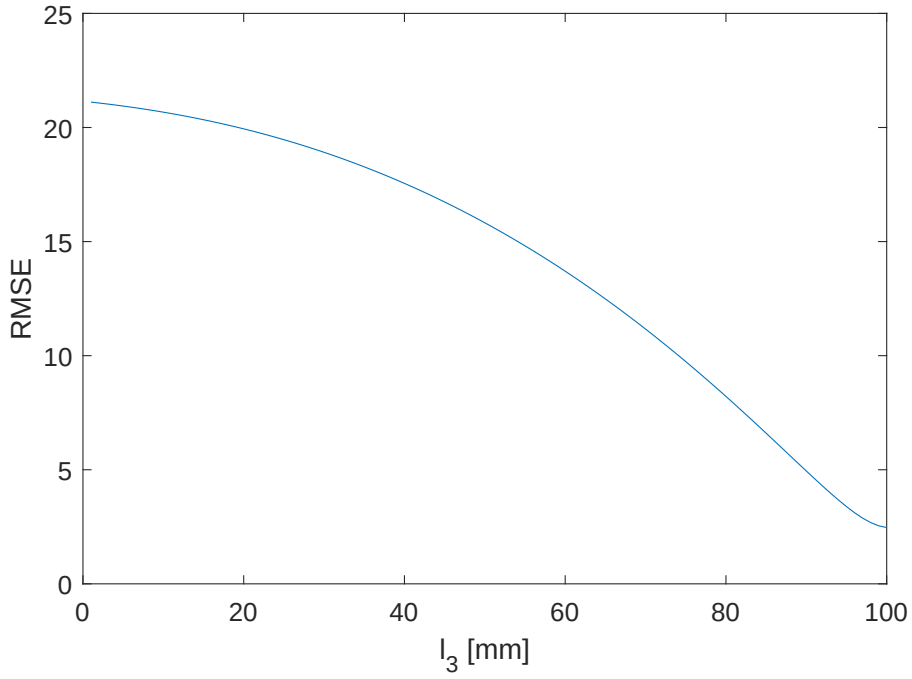

Figure 2.23: The RMSE about optimal point with different l_3.

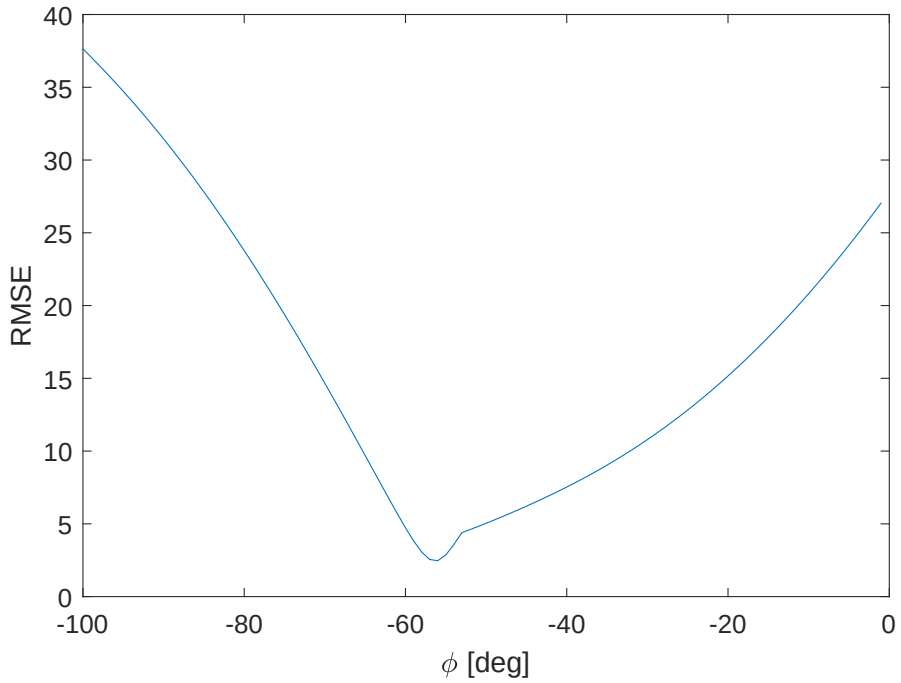

Figure 2.24: The RMSE about optimal point with different ψ.

force at 3 MPa. This cylinder has 34 mm at 3 MPa hydraulic pressure, and again, the piston rod is ignored.

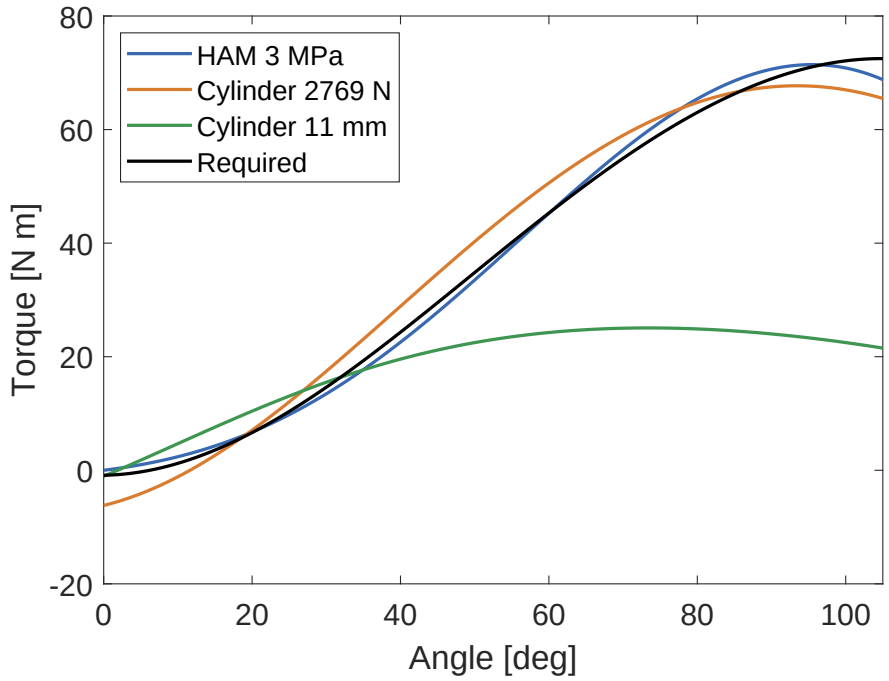

Figure 2.25: Optimal torque output results found through numerical analysis hydraulic cylinders compared to HAM.

The results are shown in Fig. 2.25. The 11 mm cylinder has a much lower force output than HAM, which results in a much lower torque output than required. The 2769 N cylinder, in contrast, has a lower peak torque and negative torque at low knee joint angles, which may hinder the STS action. Moreover, the 2769 N cylinder has a piston diameter of 34 mm, which is much larger, and possibly heavier than the HAM equivalent. Lastly, the hydraulic cylinder is also not compliant, which negatively affects the pHRI of the resulting device.

The superior results of the HAM were achieved due to its high peak contraction force, and its unique force-contraction relationship. In other words, the HAM and optimized linkage design realize the required torque-angle properties without complicated hydraulic pressure control but only by keeping constant pressure. This makes the hydraulic control system very simple and practical.

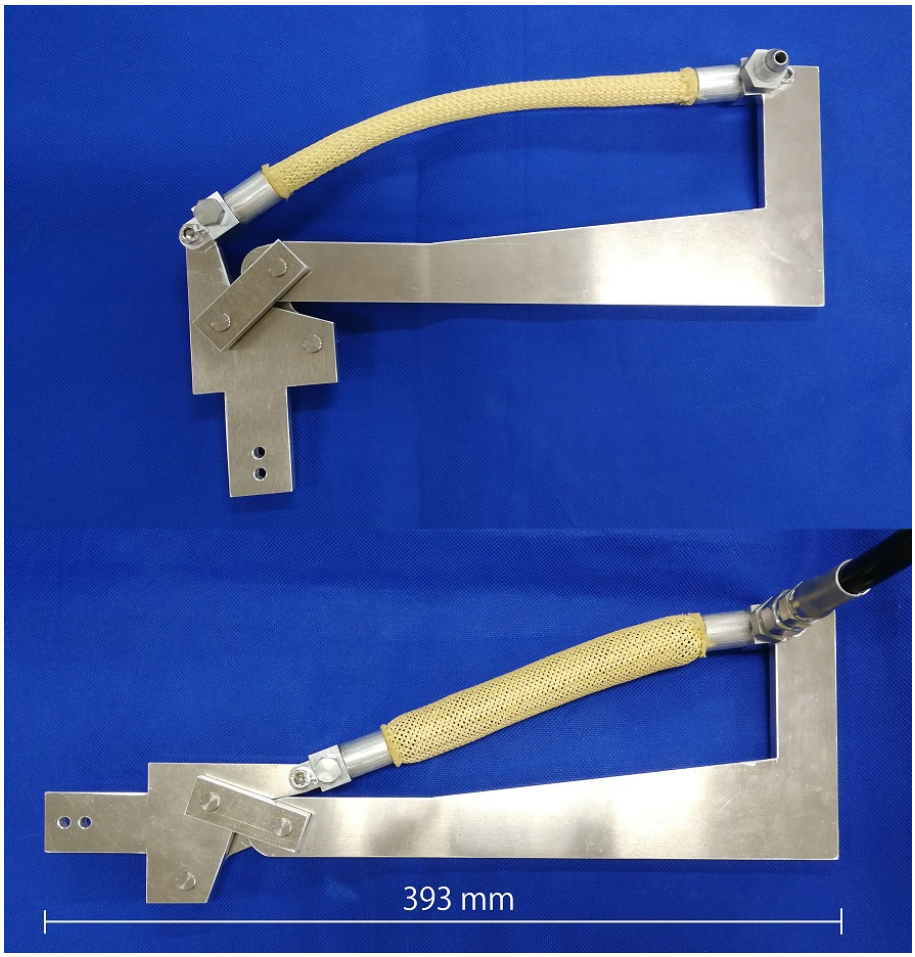

Figure 2.26: Photograph of the experimental device in unpressurized state and with 3 MPa applied pressure [99].

2.3 Experiments

Two experiments were conducted to verify the effectiveness of the developed device. First, the torque output of the device was measured to confirm the performance of the HAM and Angled Bar. Second, surface EMG of the subject while performing STS action was measured to validate the device's assistive capabilities. The experimental device was made from a 7 mm thick aluminum plate as shown in Fig. 2.26.

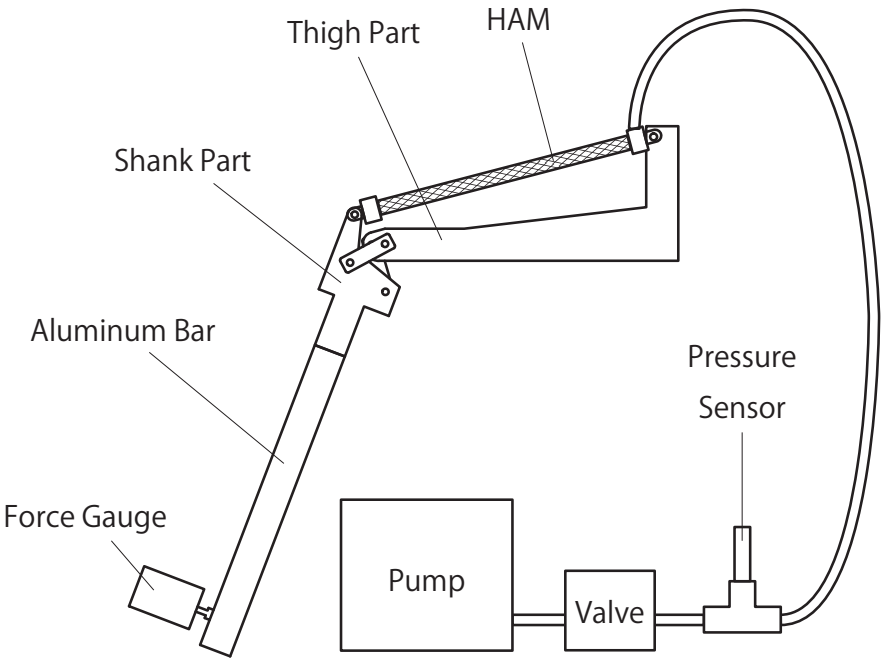

Figure 2.27: Experimental setup for joint torque measurement [99].

2.3.1 Torque Output Measurement

Methodology

The proposed device was clamped at the thigh part with C-clamps to fix the thigh part's alignment horizontally. The knee part was extended with an aluminum C-channel beam to reduce the force required to cause flexion motion and provide a working area. Next, hydraulic pressure was applied to the HAM, which caused the HAM to contract and put the shank part at full extension or $\theta_{\text{knee}} = 0°$. Force was then applied at the end of the extended aluminum beam by pressing a force gauge against the beam by hand until it reached the measuring angle. For the unloading curve, the shank part was first pushed until it reached the maximum flexion position at $\theta_{\text{knee}} = 105°$, then the applied force was reduced until the shank part extended to the measuring angle. To account for hysteresis, the reading were recorded only if it reached the measuring angle from the desired direction. The experimental setup is shown in Fig. 2.27.

The output torque was calculated by multiplying applied force to distance to ICR plus torque created by the weight of the extended bar. The applied force was measured using a force gauge (FGP-50, NIDEC DRIVE TECHNOLOGY CORPO-

RATION, Kyoto, Japan), and the angle was measured by a digital angle gauge (WR300, Barry Wixey Development, USA). The hydraulic pressure was supplied from a hydraulic unit (YU-65912, HI-PLAN Ltd., Tokyo, Japan) controlled with a hydraulic valve (BSDFA03-P-315, Wandfluh AG, Frutigen, Switzerland) and was measured using a digital pressure transmitter (8252.83.2517, Trafag AG, Bubikon, Switzerland).

Results

The experiments were conducted at 3 MPa applied pressure. The torque output gradually increases until reaching the peak at 105° in the loading curve, then gradually decreases during unloading, following the expected curve. The device showed a different torque curve during knee extension and flexion due to the hysteresis characteristic of the HAM, which has different contraction forces during loading and unloading. The results are shown in Fig. 2.30.

Experiments were also conducted at lower pressure to investigate its applicability for individuals with lower body mass or individuals with partial strength. The required torque curved was therefore computed with a proportionally reduced body mass of the average model. The resulting and expected results at lower pressures are shown in Fig. 2.28 and Fig. 2.29.

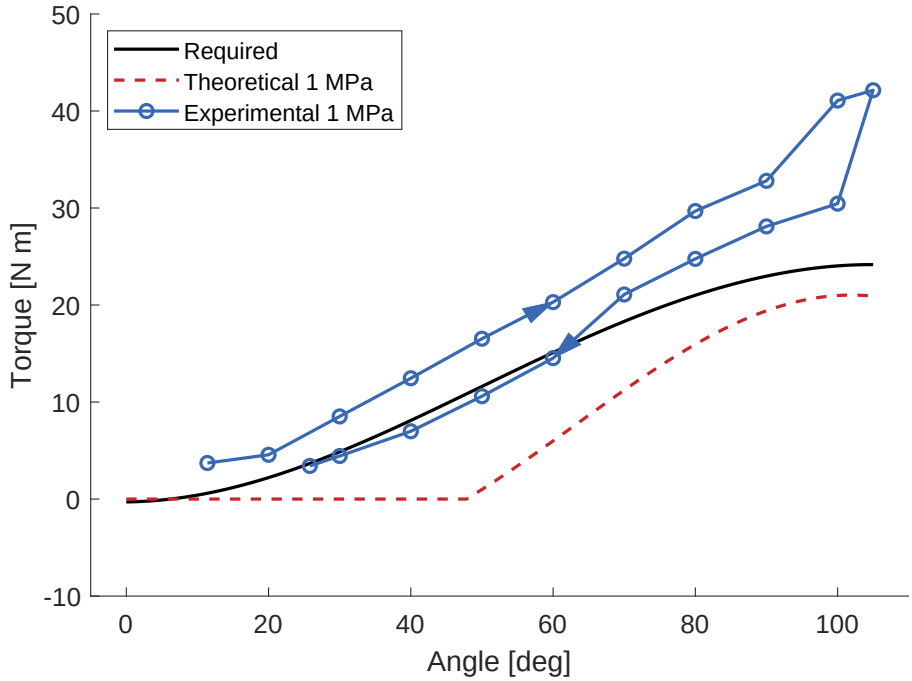

Figure 2.28: Torque output of the developed device at 1 MPa applied pressure.

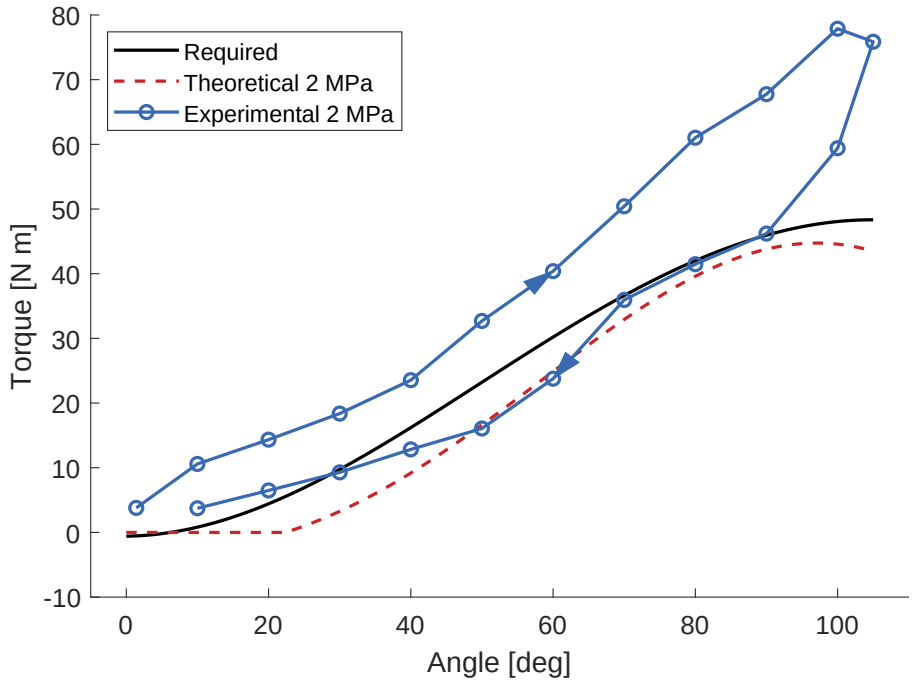

Figure 2.29: Torque output of the developed device at 2 MPa applied pressure.

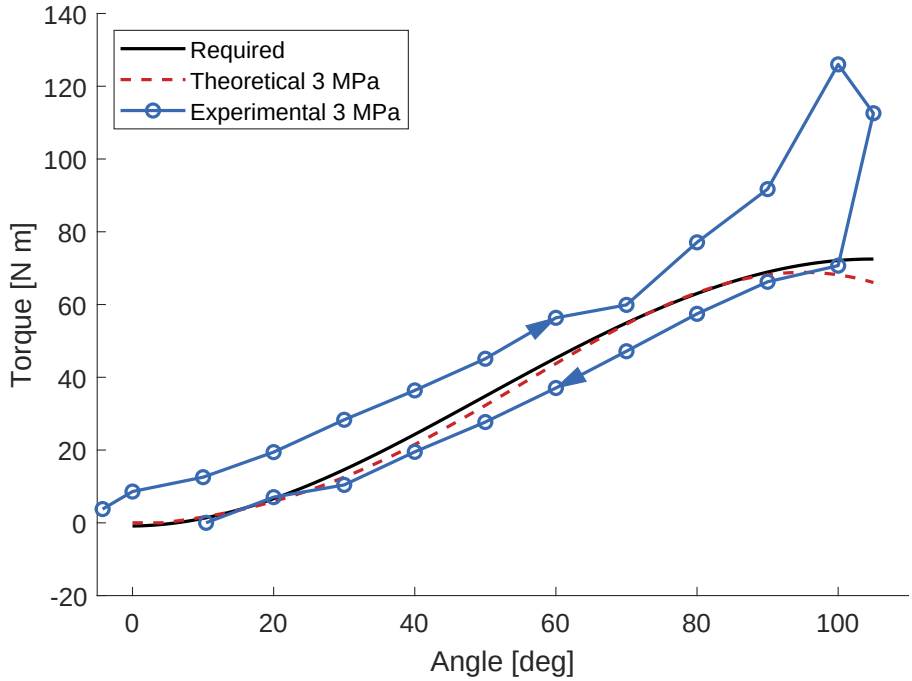

Figure 2.30: Torque output of the developed device at 3 MPa applied pressure [99].

2.3.2 Support Evaluation Experiment

Methodology

To validate the effectiveness of the proposed device in applications for humans, an experiment with a healthy subject was conducted. The participant was a 24-year-old healthy male with 1.65 m body height and 56.4 kg body mass. An aluminum bar, 3D-printed braces, and fabric straps were fitted to the device to attach the device to the leg of the user as shown in Fig. 2.31. The weight of the device including the braces and straps were 0.9 kg. The device was worn only on the right leg as shown in Fig. 2.32. Hydraulic pressure was reduced to 2.30 MPa in proportion to the participant's body mass.

The subject performed three trials of the experiment while wearing the device, each time with and without assistance from the device. One trial of the experiment consists of sitting in a normal position for 60 s, leaning forward and sitting in a seat-off position for 10 s, performing STS at natural speed, and stand for 10 s. For the active trial, the device was activated at the start of STS. The subject's arms were folded across the chest for the whole duration of the experiment The subject tried to keep the ground reaction force on both feet equal.

Hydraulic pressure was supplied and controlled with the same equipment as the previous experiment. The EMG signal on the right Rectus femoris was measured using a surface electromyography device (FREEEMG 1000, BTS Bioengineering, MI, Italy). The sensor was placed at 50% on the line from the anterior spina iliaca superior to the superior part of the patella [112]. The signal was sampled at 1 kHz, and processed with a sliding window root mean square of 200 samples windows length. The signals were resampled and normalized to the STS duration, then the mean and standard deviation between the three trials were calculated.

Results

The processed EMG signal showed a substantial reduction in muscle activity especially at seat-off with the assist of the device as shown in Fig. 2.33. The maximum processed EMG signal with and without assist were 52.10 and 20.93 µV, respectively.

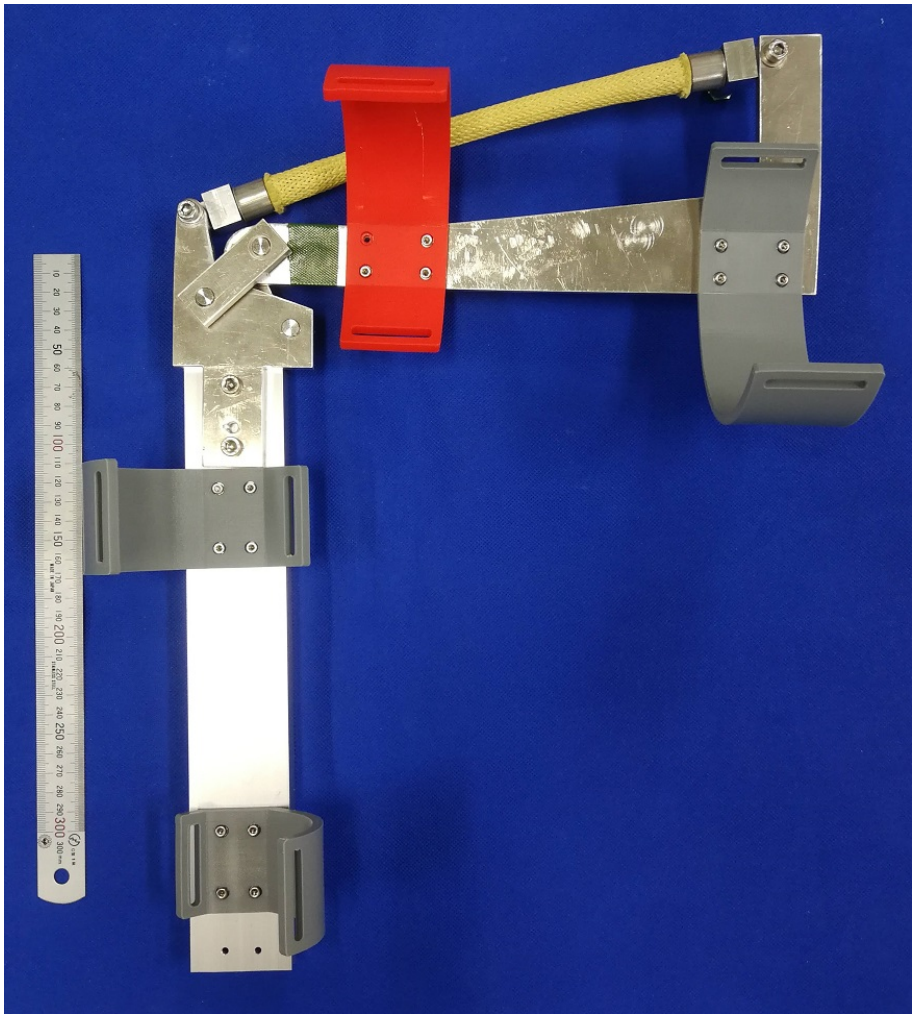

Figure 2.31: The developed device with an aluminum bar and 3D-printed braces. Straps were removed for clarity.

Figure 2.32: Photo of the subject wearing the developed device.

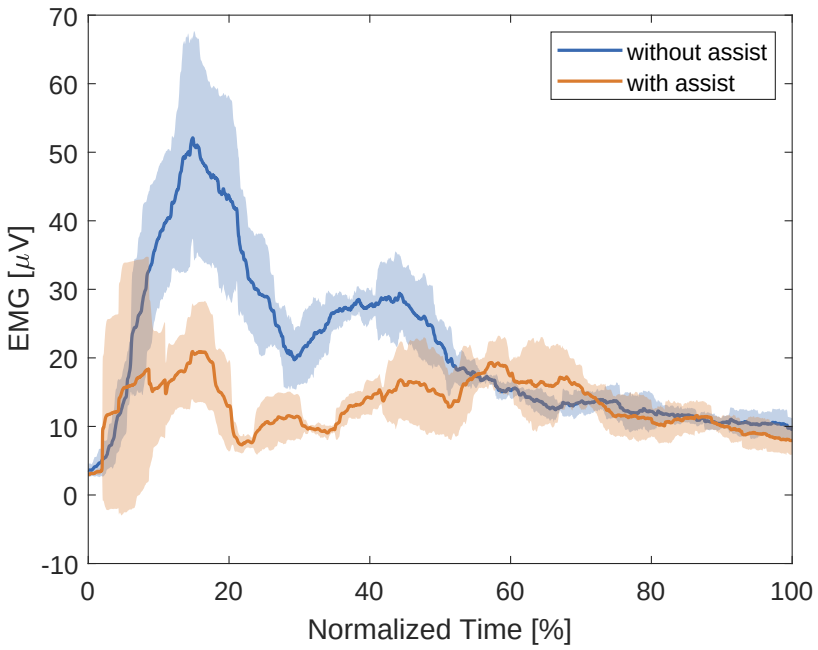

Figure 2.33: Processed EMG signal on the Rectus femoris of the subject during STS with and without assist. The standard deviation is shown as shading.

2.4 Discussion

The experimental torque output results agreed well with the expected results up to 100° at the target pressure of 3 MPa. The output torque curve showed a significant difference between loading and unloading. This is mainly caused by hysteresis characteristics of the HAM. Mechanical deformations of the links also played a significant role due to the unaccounted bending moment. However, during STS, the knee joint moves in the the extension direction (i.e., reducing knee joint angle). It is important to understand that the device was designed and developed with only the unloading curve in mind; the loading curve, which differs from the expected results, is only included for completeness.

As the device was designed according to the 73.0 kg body model, the expected result torque showed greater error at lower pressure. Despite this, experiment results showed no significant deviation from the required torque. This means that it is feasible to apply the device for individuals with different weight by reducing the pressure proportionally. However, decreasing the pressure below 1 MPa may not be practical due to the significantly lower contraction ratio of the HAM. In contrast, it is theoretically possible to increase the pressure up to 5 MPa to account for people with higher body mass. Experiments at higher pressure were deemed unsafe due to the device being designed for 3 MPa pressure, but remain a possibility in future iterations.

The large error at 105° occurs at all supplied pressure. This is because it is in a transition from the loading to unloading hysteresis curve, which resulted in large error at rest length for the least-square model as shown in Fig. 2.19. Discarding this point would reduce the RMSE from 13.01 Nm to 5.05 Nm at 3 MPa. The RMSE between required, expected, and experiment results are shown in Table 2.6.

The proposed device, including support equipment, weighs 0.9 kg and exhibits

Table 2.6: RMSE at different pressures.

	1 MPa	2 MPa	3 MPa
Required-Expected	6.08	4.60	1.98
Required-Experiment	6.45	9.55	13.01
Expected-Experiment	10.20	11.26	14.57

a peak torque of 70.7 N m in the unloading curve. This results in a peak torque per weight ratio of 78.56 $\mathrm{N\,m\,kg^{-1}}$. When comparing the proposed device to other studies on knee exoskeletons in Table 1.1, it demonstrates a significantly higher torque per weight ratio compared to motor-powered devices and more than twice as much as a hydraulic cylinder-powered exoskeleton. However, it is important to note that Bowden cable devices still offer a much higher torque per weight ratio due to their powerful off-board actuation system.

Reduction in EMG signals confirmed the effectiveness of the device in providing support for STS in individuals with lower-than-average weight. The EMG signal without assist also confirms the validity of the STS model that the highest torque requirement is at seat-off. EMG signals showed no significant differences from 60% to 100%, which shows that the device did not hinder the normal standing position.

The subject reported minor discomfort and pain both while seated and during STS due to stiffness of the 3D-printed brace. The braces were made according to the shape of the leg in a standing position, which it fitted properly. However, the thigh deformed while seated due to the reaction force from the chair which caused discomfort and pain. During STS, the force which acted on the shank was large due to the large torque output, which also created discomfort and pain. The design of the braces and the suitable materials will be further explored in the future.

The subject also reported device slippage in standing position. This occurred due to the weight of the device, and the shape of the leg, which becomes smaller in the distal direction. No slippage occurred in a seated position or during STS. This can be easily solved by extending the device to the sole which will also provide a weight-bearing capability.

In this experiment, mineral oil was utilized as the hydraulic fluid. However, oil leakage emerged as a significant concern during human experiments due to cleaning challenges. Therefore, adopting water as the hydraulic fluid could be more suitable for wearable exoskeletons.

2.5 Chapter Summary

In this chapter, a STS-assist exoskeleton based on a four-bar linkage mechanism and a HAM is proposed. The HAM, a lightweight actuator with a high force output, allows the device to generate the large torque required for STS without adding

excessive inertia to the lower extremities. The HAM is combined with a polycentric four-bar linkage mechanism based on an anatomical knee joint to reduce human-robot misalignment. To adapt the force-contraction characteristics of the HAM to the geometry of the four-bar linkage, the Angled Bar was proposed as an addition to the polycentric four-bar link mechanism. The Angled Bar enables the proposed device to generate the required torque for STS action by simply applying a constant pressure to the HAM. The target torque for the Angled Bar was calculated as a function of knee flexion angle based on literature data, and the optimal parameters of the Angled Bar were obtained using grid search.

The performance of the device was evaluated through two experiments. First, the torque output of the device was measured to verify its ability to mechanically support the STS motion. The device was able to generate the required torque for the target body mass with an RMSE of 5.05 Nm. Additionally, the device was capable of supporting persons with a lower or higher body mass by varying the applied hydraulic pressure proportionally to the body mass. Second, the degree of support provided by the device for STS motion was evaluated through a human trial. The reduction of muscle activity was measured via EMG. The experiment was conducted on a 24-year-old healthy male with a body mass of 56.4 kg. With the support of the device, the EMG decreased significantly from 52.10 µV to 20.93 µV

This chapter provides a foundation for the development of exoskeletons with advanced features capable of assisting with more complex ADLs including SC. Nonetheless, it is important to note a significant limitation of the exoskeleton proposed in this chapter, which was not addressed: the hydraulic power unit. The hydraulic power unit, which is essential for any hydraulic system, presents a significant challenge, particularly for wearable devices, due to its considerable weight. Furthermore, to further expand the capabilities of the proposed exoskeleton to also support other joints such as the hip or ankle in other ADLs, a hydraulic supply system for multi-DoF systems will be crucial. In the upcoming chapter, a novel hydraulic control algorithm will be presented, which enables simplification of the hydraulic system and reduces its weight for future exoskeletons with a higher number of DoFs.

Chapter 3

Hydraulic Control Systems

This chapter presents innovative hydraulic control algorithms for multi-DoF hydraulic systems. The algorithm integrates the benefits of conventional centralized systems and EHAs by synchronizing the source pressure from the centralized pump with the on–off valves connected to each actuator. This enables the use of smaller and lighter on–off valves, which are simpler than the large and intricate valves employed in traditional centralized systems. Moreover, the proposed algorithms offer improved efficiency compared to conventional systems. The reduced weight and improved efficiency makes hydraulic systems more suitable for wearable applications. Moreover, its capabilities to power multi-DoF systems enables the system to be used with a more complex exoskeletons. The work presented in this chapter was partially published in [113].

3.1 System Proposal

Weight and inertia are significant limitations in the development of wearable robots, particularly when hydraulic systems are utilized. In 1-DoF exoskeletons, EHAs have been a popular choice due to their high power output in a compact package. However, as the exoskeleton covers more joints and the number of DoFs becomes higher, the weight of each hydraulic unit in every EHA becomes excessive. To overcome these constraints, this research seeks to replace conventional control valves with simpler on–off valves, with a centralized servo pump. This modification reduces the weight of multi-DoF hydraulic systems, making it a more feasible option for multi-DoF powered exoskeletons compared to traditional centralized hydraulic systems or

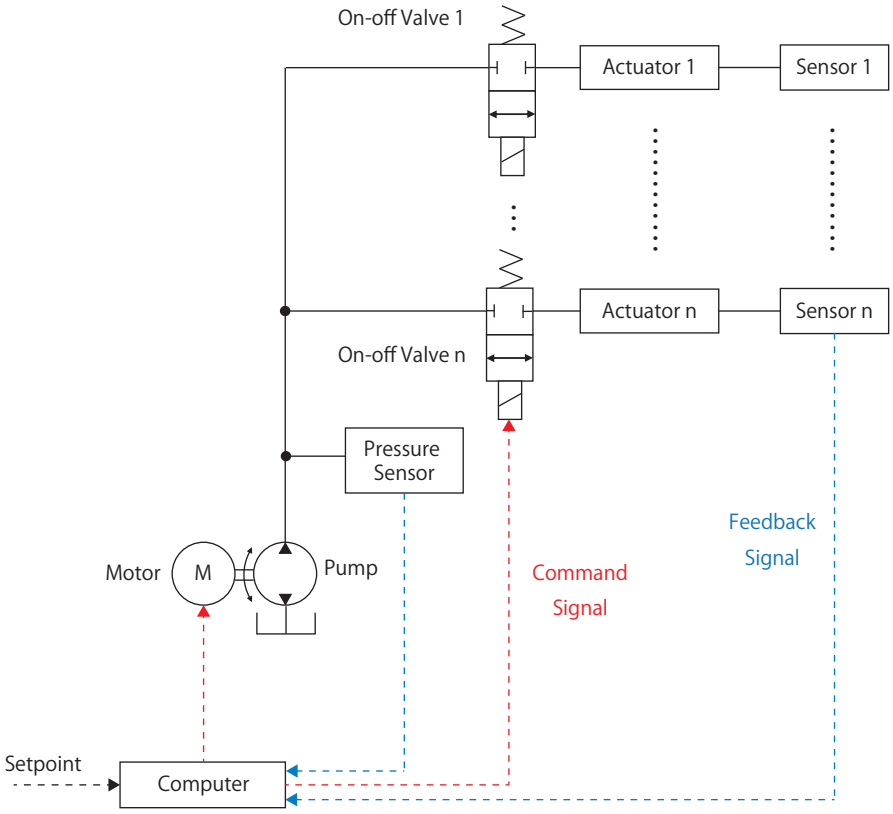

Figure 3.1: Diagram of the multi-DoF hydraulic system discussed in this chapter. The system consists of one centralized servo pump, and single-acting actuators, each connected to an on–off valve.

EHAs.

The multi-DoF system discussed in this chapter comprises a centralized servo pump, which consists of a servo motor attached to a fixed displacement pump. As a result, the system's source pressure and flow rate can be controlled by varying the motor's torque or angular velocity. The pump's IN port is connected to the tank, while the OUT port is linked to multiple sets of actuators. Each set of actuators consists of an on–off valve, a self-returning actuator (such as a single-acting cylinder or HAM). Additional sensors, such as a pressure or displacement sensor, may also be included in the system depending on the algorithm utilized. Water has been chosen as the hydraulic fluid for future implementation in wearable devices. A diagram of the multi-DoF is shown in Fig. 3.1.

In this chapters, two control algorithms are proposed for hydraulic pressure and

volume control: the alternating pressure control system (APCS) and multichannel EHA (MEHA). In addition, two variants of the APCS is also proposed, namely the open-looped APCS (APCS-OL) and APCS with dynamic duty ratio (APCS-DRR) which improves on certain aspects of the APCS.

3.2 Alternating Pressure Control System

The control algorithm of an Alternating Pressure Control System (APCS) for pressure control can be described in the following steps:

1. Periodic Pressure Command: The controller initiates the control process by sending a periodic pressure command to the servo pump. This command can take the form of any periodic waveform including a sinusoidal wave, triangular wave, or a rectangular wave, depending on the desired pressure profile. The servo pump generates an oscillating pressure based on this command, which is distributed to all the hydraulic actuators in the system.

2. Pressure Comparison: The controller continuously compares various pressure values to assess the system's state. It compares the source pressure (the pressure generated by the servo pump), the reference pressure (the desired pressure), and the current pressure within each actuator.

3. Command Signal Generation: Based on the pressure comparison, the controller generates a command signal to control the on–off valve associated with each actuator. The command signal determines whether the on–off valve should open to manipulate the pressure within its corresponding actuator, or close to keep the current pressure.

4. Pressure Manipulation: The on–off valve receives the command signal from the controller and adjusts its state accordingly. When the valve opens, it allows pressurized fluid to flow into or out of the actuator, increasing or reducing the pressure. Conversely, when the valve closes, it blocks the fluid flow, preventing change to the pressure within the actuator. By manipulating the on–off valves, the controller can control the pressure within each actuator as required.

This control algorithm enables the APCS to actively regulate the pressure within the hydraulic actuators. By continuously adjusting the on–off valves based on pressure comparisons, the APCS can maintain the desired pressure profile and respond to changes in the control input effectively.

While the APCS is based on volume control, it can also be adapted for volume control as well. Volume control for APCS will be discussed in Section 3.2.5.

3.2.1 Alternating Pressure Source

The alternating pressure source is an integral part of this study. Higher frequencies result in quicker system response and less delay; however, this response is restricted by the limitations of the pump and servo motor and the operating speed of the valve. Moreover, different alternating pressure waveforms can also lead to variable performance depending on the type of application. An APCS with a rectangular wave, associated with abrupt changes of pressure in the alternating pressure source, would enable a faster response with a higher alternating frequency. This makes a rectangular wave source pressure suitable if the actuator only requires the pressure to be on or off. In contrast, a continuous waveform such as sinusoidal or triangular wave exhibited a more gradual change in pressure. This allows the valves to open or close at any point between the maximum and minimum pressures and additionally allows any pressure value between the minimum and maximum values to be used as a setpoint.

3.2.2 Pressure Control

The valve controllers compare the source pressure, the pressure inside the actuators, and setpoint, and then open or close the valves depending on the situation. The valve opens if Eq. 3.1 is true. The logical operator AND and OR are denoted as $\wedge$ and $\vee$, respectively.

$$((P_s > P_a) \wedge (P_r > P_a)) \vee ((P_s < P_a) \wedge (P_r < P_a)) \tag{3.1}$$

where

P_s is the source pressure;

P_r is the reference pressure; and

P_a is the actuator pressure.

Moreover, an additional condition can be added to prevent overshoot, which would increase the error instead of reducing it: the valve should only open when P_r is closer to P_s than to P_a, i.e. when Eq. 3.2 is true.

$$|P_r - P_s| < |P_r - P_a| \tag{3.2}$$

The stability of the system can be improved by using a dead zone around the target pressure. The implementation of the valve controller in MATLAB Simulink is shown in Fig. 3.2

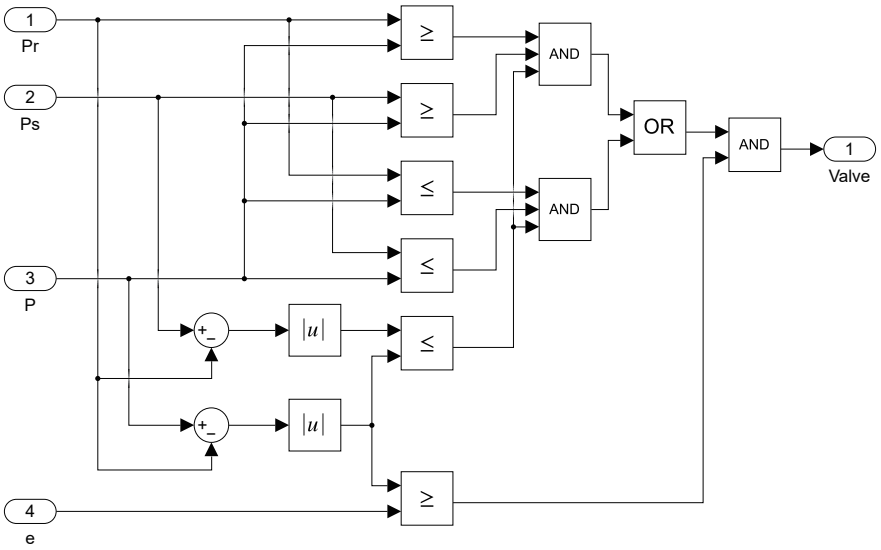

Figure 3.2: Implementation of the valve controller logic in a pressure-controlled pump for a force-controlled mode in Simulink where e is the value of dead band.

To investigate how continuity of reference signal and source pressure waveforms affects the performance of the system, permutations between continuous and discontinuous signals were investigated. Using rectangular wave as discontinuous signal and sinusoid as continuous signal results in four permutations:

1. Rectangular source, rectangular setpoint (R-R)
2. Sinusoidal source, rectangular setpoint (S-R)
3. Rectangular source, sinusoidal setpoint (R-S)

4. Sinusoidal source, sinusoidal setpoint (S-S).

3.2.3 Dynamic Duty Ratio

For a rectangular wave, it is also possible to manipulate the duty ratio to improve the overall performance of all the cylinders. The dynamic duty ratio system allows the prioritization of high or low pressure in systems with a rectangular reference signal. It is particularly useful in applications where a large flow rate is required, such as volume control which will be discussed in Section 3.2.5. The normal APCS assumes that the volume change required by the actuator is small, and that the actuator pressure will instantly increase or decrease to the supply pressure when the corresponding valve is opened. However, in reality, the actuator may be able to extend or retract without encountering any resistance. In such scenarios, the dynamic duty ratio, which adjusts the duty ratio dynamically to prioritize all active actuators equally, can improve the overall performance of the system. Additionally, dynamic duty ratio can also enhance energy efficiency in applications where the required flow rate is minimal by reducing pump utilization when control action is not required. It's important to note that the dynamic duty ratio is not applicable in pressure control systems with a continuous reference pressure signal.

Herein, the dynamic duty ratio function for a system with n actuators is expressed as Eq. 3.3

$$\mathrm{DR} = \frac{1}{2}\left(\frac{\sum_{i=1}^{n}\mathrm{sgn}(x_{r,i}-x_i)}{\sum_{i=1}^{n}|\mathrm{sgn}(x_{r,i}-x_i)|}+1\right). \tag{3.3}$$

where:

$x_{r,i}$ is the reference signal of actuator i for the relevant mode (force or displacement), and

x_i is the current state of actuator i.

Function sgn denotes the signum function, which is defined as follows:

$$\mathrm{sgn}(x) := \begin{cases} -1 & \text{if } x < 0, \\ 0 & \text{if } x = 0, \\ 1 & \text{if } x > 0. \end{cases} \tag{3.4}$$

However, a duty ratio value that is too low results in a short pulse, which does not provide sufficient time for the pump to reach the desired value. Similarly, a very

high duty ratio value results in the pressure not falling to the desired value. To prevent this, the rise time (t_{rise}), fall time (t_{fall}), and alternating pressure frequency (f) of the pump can be used to calculate the applicable range of the dynamic duty ratio value (DR_{app}), as shown in the equation below:

$$\text{DR}_{\text{app}} = \begin{cases} 0 & \text{if } DR = 0, \\ t_{\text{rise}} f & \text{if } 0 < DR \leq t_{\text{rise}} f, \\ \text{DR} & \text{if } t_{\text{rise}} f < DR < 1 - t_{\text{fall}} f \\ 1 - t_{\text{fall}} f & \text{if } 1 - t_{\text{fall}} f \leq DR < 1 \\ 1 & \text{if } DR = 1. \end{cases} \tag{3.5}$$

The value of t_{rise} and t_{fall} in the context of this paper are obtained experimentally as the time taken by the pump to reach maximum pressure or minimum pressure after receiving a step input signal.

3.2.4 APCS-OL

The APCS-OL is a modification of the APCS that operates without a feedback sensor. In APCS-OL, the source pressure supplies a periodic alternating pressure. The on–off valves connected to each actuator opens or closes in synchronization with the pump by comparing the source and reference pressures in the actuator. The outline of the APCS-OL is presented in Fig. 3.3.

The major difference between the APCS and APCS-OL is defined by the algorithm of the valve controller. In APCS-OL, the valve of actuator i opens when Eq. 3.6 is true.

$$|P_{r,i} - P_s| < \epsilon \tag{3.6}$$

where:
$P_{r,i}$ denotes reference pressure of actuator i, and
ϵ represents the error band.

As the APCS-OL does not consider any feedback, the valves are required to be opened and the pressure should be readjusted even if the reference pressure signal does not vary to counteract any potential disturbances caused by external forces.

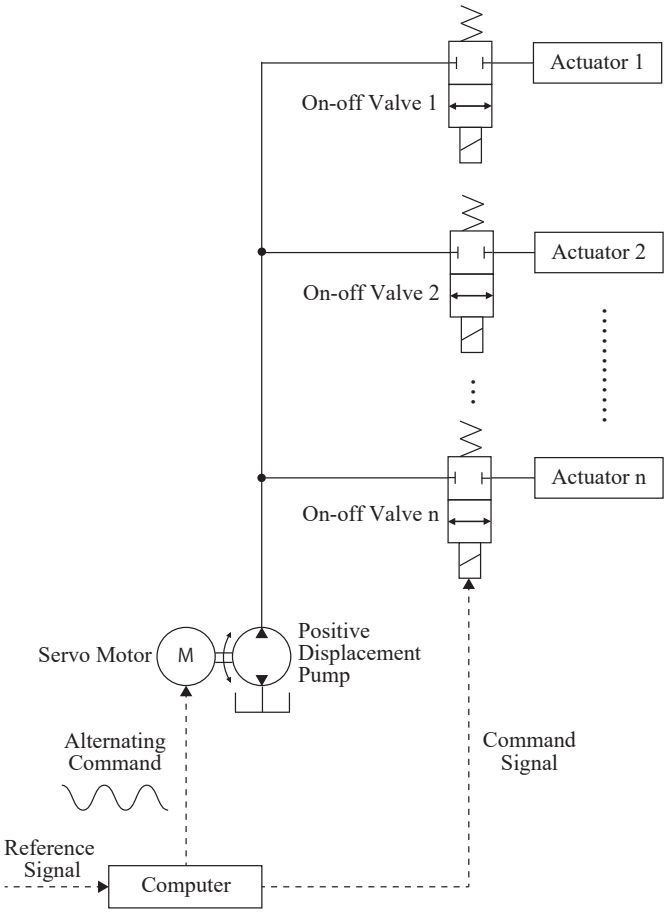

Figure 3.3: Outline of APCS-OL system.

This implies that the dynamic duty ratio used for reducing the power consumption in APCS is inapplicable for APCS-OL.

3.2.5 Volume Control

To adopt the APCS for volume control, and additional sensors for volume feedback (e.g. position sensor for hydraulic cylinders) are required. Operation in this mode is relatively simple: a rectangular wave with a dynamic duty ratio expressed in Eq. 3.3 is provided to the pump. The amplitude of the source pressure is the maximum operating pressure of the pump. The valve then opens or closes according to the direction of the pump and the desired cylinder direction, i.e., the valve opens if Eq. 3.7 is true:

$$((P_s > P_a) \wedge (V_r - V_a \geq \epsilon)) \vee ((P_s < P_a) \wedge (V_r - V_a \leq \epsilon)) \tag{3.7}$$

where:

V_r is the reference actuator volume, and

V_a is the actuator volume.

The dynamic duty ratio allows all the actuators to be equally prioritized while improving the performance when only a number of actuators are active.

3.3 Multichannel EHA

A multi-degree-of-freedom MEHA system comprises a centralized servo pump, hydraulic actuators, and a single on–off valve per actuator, as depicted in Fig. 3.4. Each actuator can be operated as a traditional EHA by opening the valve connected to its corresponding actuator, as the other valves remain closed. In principle, the actuators are classified as either active or inactive; active actuators are actuators that require pressure control, whereas inactive actuators do not require a control action. The controller cycles through all the active actuators and operate them as required. In each cycle, the controller opens the valve and activates the servo pump to supply the required pressure or flow, or it skips the actuator if activation is not required. If no actuator requires control action, the motor shuts off to reduce energy consumption.

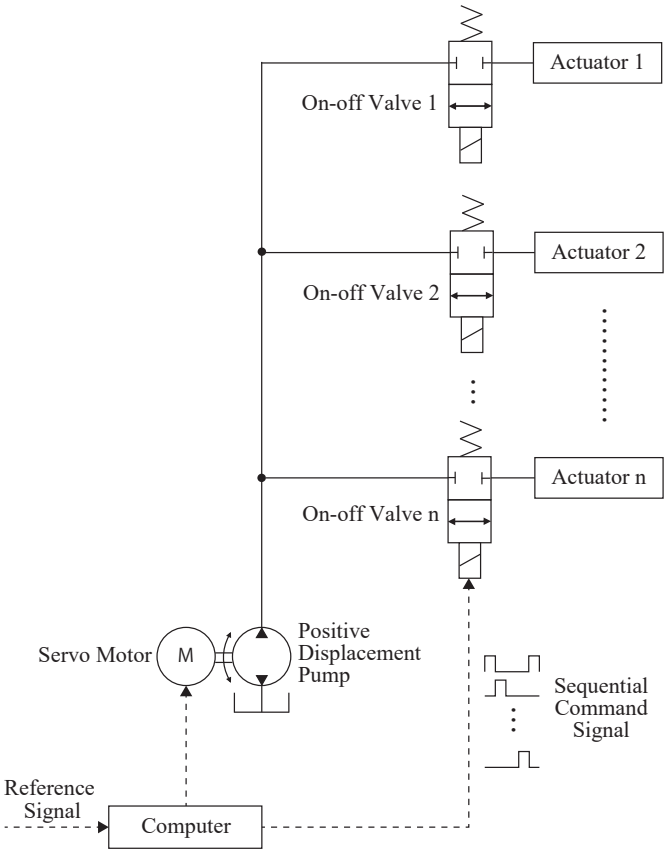

Figure 3.4: Outline of MEHA system.

3.3.1 Pressure Control

In pressure control mode, the controller cycles through all the active actuators and sequentially operates them even if there is no alteration in the reference pressure to account for the possible disturbance due to external forces. The motor shuts off only when all actuators are marked as inactive or when the pressure in all active actuators are set to 0. The process in which the controller operates an actuator in a cycle is described as follows:

1. Source pressure is set to the reference pressure of actuator
2. Controller waits for the source pressure to settle
3. Valve opens for a short period
4. Valve closes

5. Controller waits for valve to shut off completely

6. Controller cycles to subsequent active actuator.

The period for each actuator can be expressed as

$$t_{\text{period}} = t_{\text{settling}} + t_{\text{open}} + t_{\text{close}}, \tag{3.8}$$

where:
t_{period} denotes the period of each actuator;
t_{settling} represents the settling period of source pressure;
t_{open} denotes the total duration for which the valve is open, including the operating period of the valve;
t_{close} denotes the closing instance of the valve.

The parameters t_{settling} and t_{close} were experimentally obtained. In particular, setting these parameters with inadequately small values causes undesired pressure spikes, whereas larger values result in a slower response.

3.3.2 Volume Control

A self-returning hydraulic actuator such as a single-acting cylinder or HAM is required for the operation of MEHA in the volume control mode with an on–off valve. Alternatively, a 4/3 direction control valve with an additional return line can also be used for volume control with a double-acting cylinder. The utilization of a double-acting cylinder with a 4/3 flow control valve enables the system to manage overrunning loads at the cost of more complex piping and valves.

In the volume control mode, the actuator volume can be estimated by integrating the speed of the servo motor over the period during which the valve is open. The actuators in volume control mode were individually activated in a sequence. Accordingly, two control algorithms are proposed for actuator switching: periodic switching and hysteresis switching. In the periodic switching mode, the volume can be divided into certain blocks. During each cycle, the controller increases the volume by a single block if the current volume is less than the reference volume, decreases the volume by a single block if the current volume is greater than the reference volume, or skip the actuator if the current and reference volumes are situated in the same block. The size of each block is given by pump flow rate multiplied by period.

In the hysteresis switching mode, the controller activates a single actuator until it passes the reference signal by a predetermined threshold or attains the maximum or minimum volume. Thereafter, it switches to the subsequent actuator in the sequence. This is similar to the traditional hysteresis on–off control.

3.4 Comparisons between proposed algorithms

The APCS-DDR and APCS-OL are variants of the APCS algorithm which provides enhancement in certain specific case. The APCS-DDR allows a significant reduced pump utilization time, resulting in an improved power consumption of the system. The limitation of APCS-DDR is that it can only operate in the R-R configuration. In contrast, the APCS-OL allows APCS to operate in pressure control mode without feedback sensor, allowing further simplification of components. Experiment results showed that APCS-OL offers a comparable performance to APCS. The limitations of APCS-OL being dynamic duty ratio is not applicable in this control scheme, and lower flow rate in some cases.

In the pressure control mode, the major difference between the MEHA and APCS algorithms is that the valves in the MEHA periodically open and close as the pressure source alters its pressure with respect to the reference signal of the active actuator. In contrast, the APCS systems use the pressure source to supply a periodic alternating pressure. Thereafter, the valves open or close by comparing the reference signal to its corresponding actuator and source pressure. In other words, the valves follow the pump in APCS systems, whereas the pump follows the valves in MEHA. Consequently, the pump control for the MEHA is much more complex than APCS algorithms. Furthermore, the step response performance of the pump is crucial for the system performance of MEHA. In contrast, the pump in APCS systems generates a periodic alternating pressure, which is much simpler than the MEHA. The performance of APCS systems are primarily limited by the operating speed of the valves rather than response of the pressure source.

Overall, the response time of an actuator in MEHA is inversely proportional to the number of actuators. Conversely, the response time of the APCS algorithms does not depend on the number of actuators. This implies that the MEHA is potentially faster in systems with fewer actuators, but it becomes slower as the number of actuators increases.

Table 3.1: Comparisons of MEHA and APCS.

	MEHA	APCS
Pump	Follows reference signal of the active actuator	Generates constantly oscillating pressure
Valves	Operate sequentially	Operate independently
Feedback	Not required	Required for volume control
Performance	Inversely proportional to number of actuator	Constant performance

Finally, it should be noted that open-looped volume control is only feasible with MEHA since it operates a single hydraulic actuator at a time. Achieving this with an APCS system would require the incorporation of position sensor feedback. In theory, it is also possible to simultaneously operate some actuators in pressure control mode while others are being operated in volume control mode with MEHA.

The comparisons between MEHA and APCS are summarized in Table 3.1

3.5 Simulations

Simulations were conducted as a preliminary study to evaluate the feasibility of this switching approach through the APCS algorithm. The system was simulated using MATLAB 2021a Simulink and Simscape software. The pumps in the pressure- and volume-controlled modes were modeled as perfect pressure sources. The transient response of the pump was modeled as an underdamped unity-gain second-order system with the transfer function shown in Eq. 3.9.

$$G(s) = \frac{100^2}{s^2 + 160s + 100^2} \tag{3.9}$$

Further, four sets of hydraulic cylinders and valves were connected to the pump. The components are modeled after the experimental equipment, which will be explained in detail in Section 3.6.1. It was assumed that liquid temperature was constant and there was no deformation in the components. Other conditions including cylinder friction, valve leakage, fluid compressibility and viscosity, volume of tubing were already considered. The parameters in the simulations are obtained experimentally and are given in Table 3.2.

Table 3.2: Parameters used in the simulation.

Parameter	Value
System temperature	293.15 K
Atmospheric pressure	101.325 kPa
Pump rise time	0.1 s
Pump fall time	0.1 s
Cylinder piston diameter	20 mm
Cylinder piston stroke	0.2 m
Valve delay	20 ms
Valve orifice diameter	1.5 mm
Valve leakage area	1×10^{-10} m^2

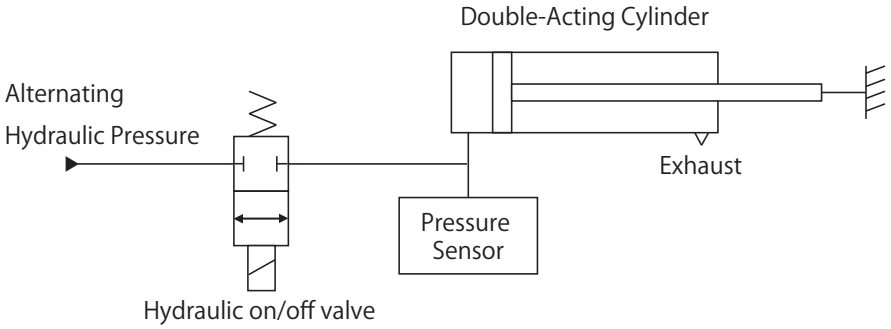

Figure 3.5: The model of the valve and cylinder in pressure control mode simulations. The cylinder rod was fixed, and the volume within the cylinder was constant.

3.5.1 Pressure Control

In the pressure control mode, both rectangular and sinusoidal waves were used for the source pressure and setpoint. All four combinations of rectangular and sinusoidal source pressure and reference signals, namely: R-R, R-S, S-R, and S-S were evaluated.

The hydraulic cylinders in the pressure control mode were simulated to be fixed with no external force acting on the cylinder. The valves were simulated as gate valves with a transport delay of 50 ms to emulate the actuation time of the real valve. The models of the valve and cylinder are shown in Fig. 3.5.

The performance of the simulated system is evaluated using the root mean square

error (RMSE) defined as shown in Eq. 3.10

$$\mathrm{RMSE} = \sqrt{\frac{1}{n}\sum_{i=1}^{n}(y_{\mathrm{r},i} - y_i)^2}. \tag{3.10}$$

where:
$y_{r,i}$ indicate the reference value at point i, and
y_i represents the measured value at point i.

In addition, for sinusoidal setpoint modes, the output delay was also calculated. A discrete Fourier transform is used to obtain the phase difference between the setpoint and pressure output, which is then used to calculate the time delay. The theoretical maximum delay corresponds to the period of the alternating pressure.

The setpoints in the rectangular setpoint modes were rectangular waves with different frequencies and pulse widths. The APCS could control the pressures in all cylinders simultaneously with both rectangular and sinusoidal pressure sources, as shown in Fig. 3.6 and 3.7. The sinusoidal pressure source has a more gradual change in pressure, resulting in a larger delay compared to the rectangular pressure source mode. However, all delays were less than the period of the alternating pressure source. Further, the RMSE values for the R-R and S-R configurations were 1.21 and 1.56 MPa, respectively.

The application of the dynamic duty ratio reduces the total pump utilization time in the R-R configuration from 50% to 41.22% and increases the RMSE to 1.62 MPa. The dynamic duty ratio decreases energy consumption by reducing the pump utilization time when all actuators are already in place; in addition, it improves the performance by increasing the pump utilization time when activating an actuator. However, the improved performance was not apparent in this simulation, where all cylinders were at a fully extended position with a virtually fixed volume. The current implementation of the dynamic duty ratio increases the theoretical maximum delay to two periods of the source pressure, which also results in an increased RMSE. The simulation results are shown in Fig 3.8

Simulations with sinusoid setpoint modes yielded contrary results; using a sinusoid wave as the source pressure resulted in lower delay and error, as shown in Fig. 3.9 and Fig. 3.10. This is because sinusoidal waves have a more gradual change in pressure compared to rectangular waves, which allows the valves more time to

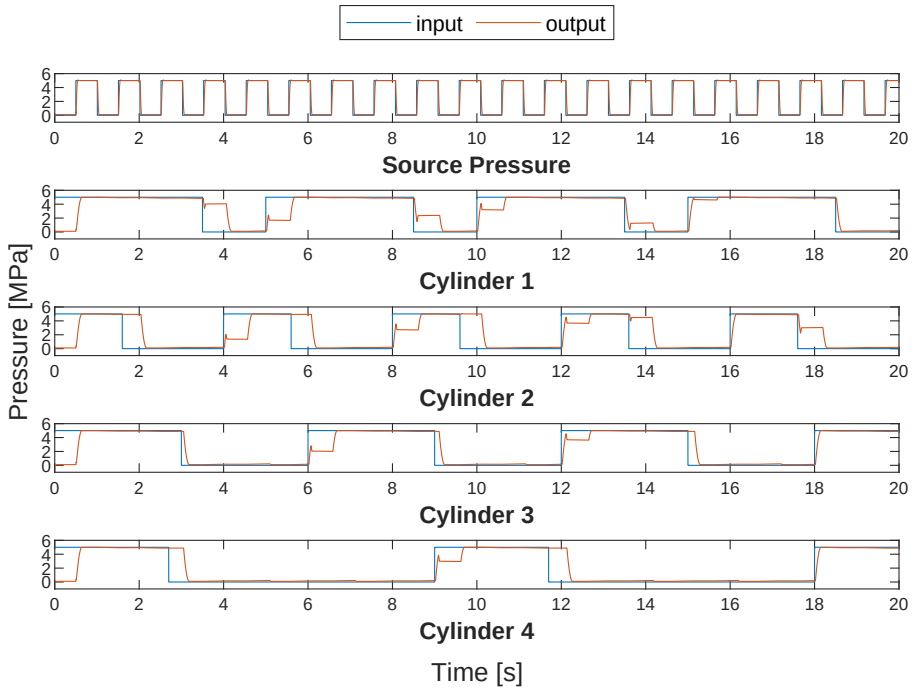

Figure 3.6: Simulation results in the R-R configuration with a 1 Hz source frequency and a 0.2 MPa deadband.

Table 3.3: RMSE and delay in S-S configuration from 1 Hz to 5 Hz. The dead band was 0.2 MPa.

Frequency (Hz)	1	2	3	4	5
RMSE (MPa)	0.69	0.52	0.41	0.40	0.46
Delay (s)	0.30	0.16	0.13	0.10	0.10

shut at the reference pressure. As a result, the R-S configuration has a larger delay (0.61 s) and RMSE (1.22 MPa) compared to the corresponding values for the S-S configuration (0.30 s, 0.69 MPa).

Increasing the source pressure frequency improves both the RMSE and the delay of the system. The delays and RMSEs of the S-S configuration between the 1 and 5 Hz source frequencies are shown in Table 3.3.

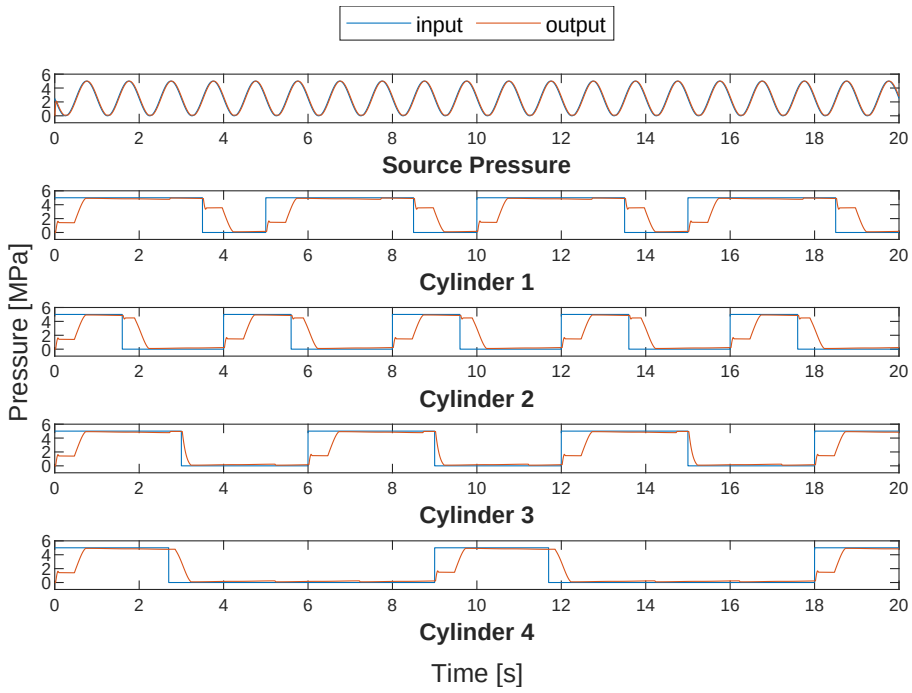

Figure 3.7: Simulation results in the S-R configuration with a 1 Hz source frequency and a 0.2 MPa deadband.

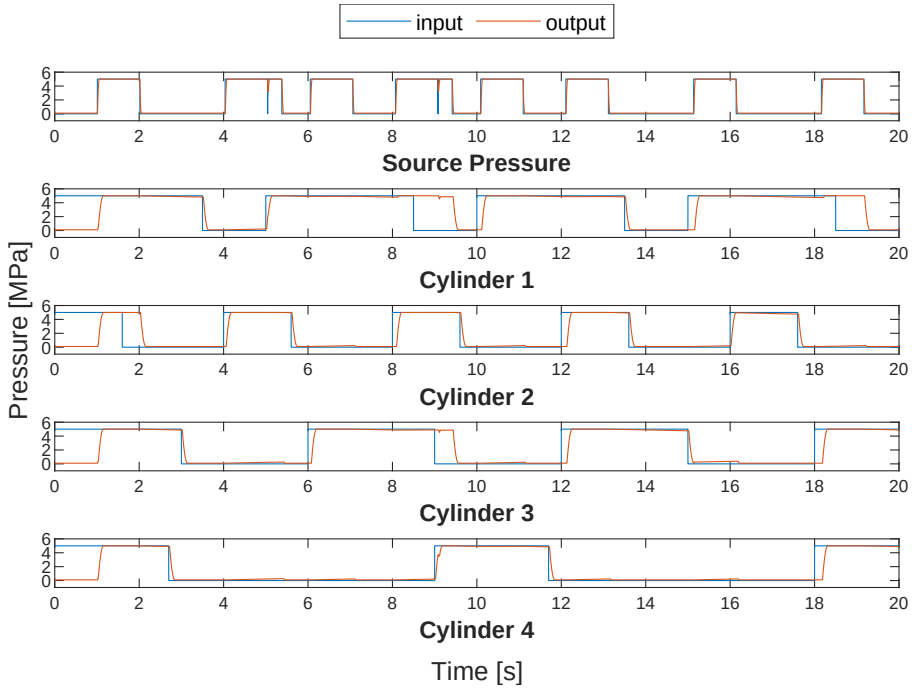

Figure 3.8: Simulation results in the R-R configuration with dynamic duty ratio with a 1 Hz source frequency and a 0.2 MPa deadband.

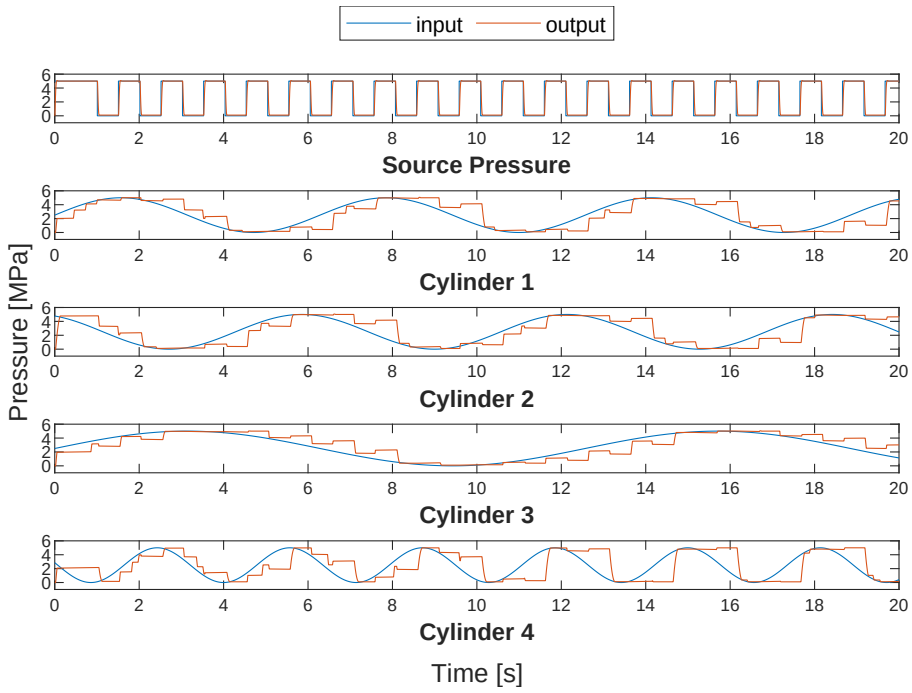

Figure 3.9: Simulation results in the R-S configuration with a 1 Hz source frequency and a 0.2 MPa deadband.

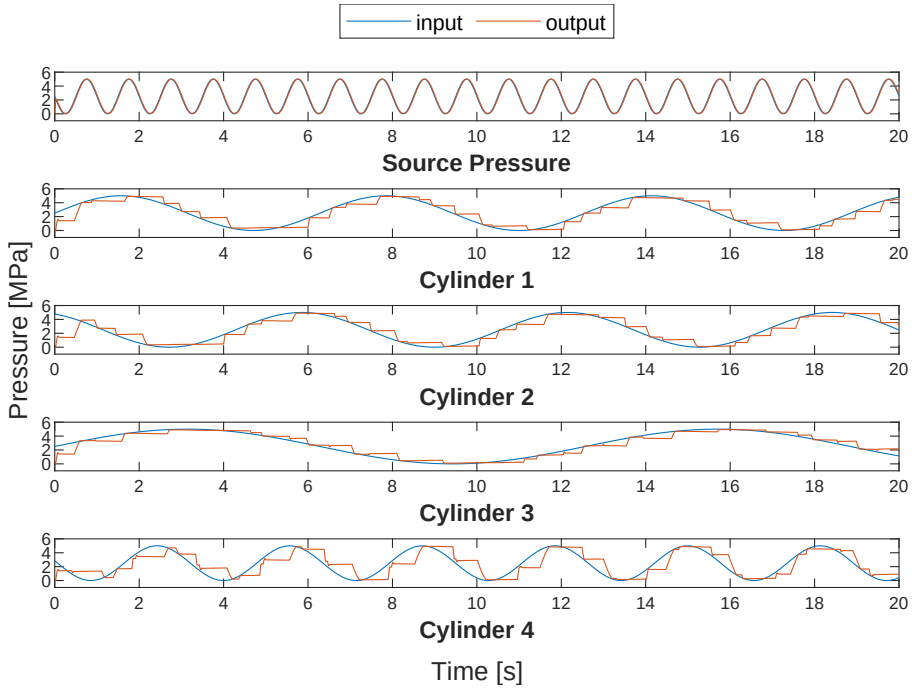

Figure 3.10: Simulation results in the S-S configuration with a 1 Hz source frequency and a 0.2 MPa deadband.

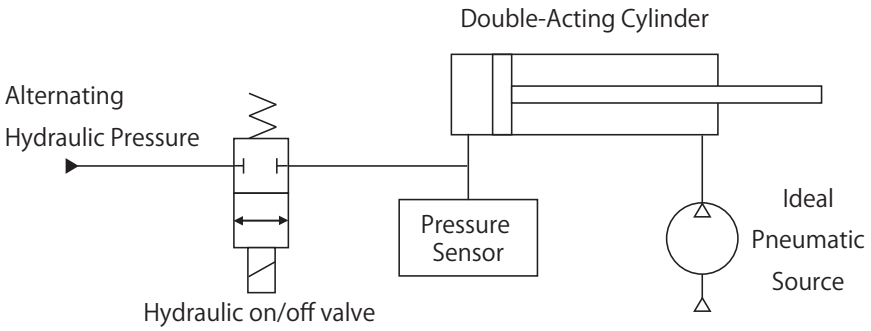

Figure 3.11: The model of the valve and cylinder in the volume control mode simulations. The double-acting cylinder acts as a single-acting cylinder with a constant pressure as the return mechanism.

3.5.2 Volume Control

In the volume control mode, a constant pneumatic pressure of 0.9 MPa is applied to the cylinder as a return mechanism instead of a return spring. This was simulated as a constant force of an equivalent magnitude acting on the rod. Further, the valves were simulated as gate valves with a transport delay of 50 ms, similar to the pressure control mode. The models of the valve and cylinder are shown in Fig. 3.11

The simulated system could operate all four hydraulic cylinders independently. The resulting positions of the hydraulic cylinder rods with a 5 mm dead band are shown in Fig. 3.12. The RMSE of all four cylinders is 3.17 mm. The pump was activated for a total of 16.30 s, which is 32.60% of the operating time.

While setting the dead band to 0 mm offers a very slight reduction of RMSE to 3.10 mm, it increases the pump utilization time by 75% to 28.14 s or 56.28 % of the operating time. Conversely, increasing the dead band to 10 mm increases the RMSE to 5.05 mm and reduces the pump utilization time to 11.63 s, or 23.26% of the operating time.

This section demonstrated the viability of using on–off valves for switching in combination with an oscillating pressure source through simulation. In the upcoming section, these simulation results will be experimentally verified, and the performance of the proposed APCS will be evaluated, along with other systems such as APCS-DDR, APCS-OL, and MEHA.

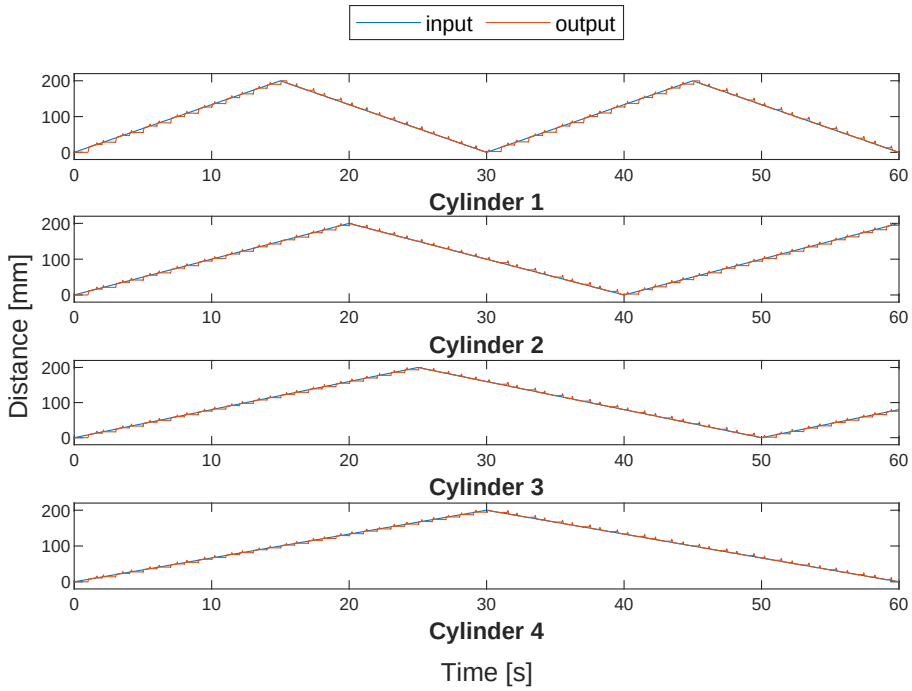

Figure 3.12: The model of the valve and cylinder in the volume control mode in Simulink Simscape.

3.6 Experiments

In this section, the pressure and volume control capabilities of the proposed systems are experimentally evaluated.

3.6.1 Experiment Setup

Herein, the experimental system comprises a servo pump, four single-acting cylinders, four on–off valves, and the primary controller. The servo pump comprises a positive displacement water pump (ASP035-T110, LEVEX Corporation, Kyoto, Japan), which was powered using a 3-phase AC servo motor (HG-SR51B, Mitsubishi Electric Corporation, Tokyo, Japan) and controlled using a servo amplifier (MR-J4a, Mitsubishi Electric Corporation, Tokyo, Japan). The servo pump exhibits a maximum working pressure of 5 MPa. The system was controlled using a controller board (MicroLabBox, dSPACE Inc., MI, USA) operating at 1 kHz.

The single-acting cylinders were simulated by applying a constant pneumatic pressure of 0.8 MPa to one side of a double-acting cylinder as a return mechanism

instead of a return spring. The double-acting hydraulic cylinders (KS-5LB20×20, JPN Co. Ltd., Tokyo, Japan) bear an inner diameter of 20 mm and a stroke of 200 mm with a nominal pressure of 7 MPa. More specifically, the cylinders are composed of stainless steel and can be operated with water as the hydraulic fluid. The constant air pressure that acts as a return mechanism was regulated with a filter regulator (FRF300-02-MD, Nihon Pisco Co. Ltd., Nagano, Japan) and a positive pressure sensor (GPD-01, Nihon Pisco Co. Ltd., Nagano, Japan).

Each on–off valves contains two solenoid flow control valves (HTJ262G002, ASCO Japan Co. Ltd., Hyogo, Japan) connected in opposite directions. Both solenoid valves are operated on the same control signal as a single on–off valve. This configuration of solenoid valves in opposite directions enables the valves to maintain pressure and prevent leakage, which is not feasible with a single solenoid valve.

Lastly, to monitor and validate the performance of the proposed system, four pressure sensors (PSE577, SMC Corporation, Tokyo, Japan) were installed between the on–off valve and hydraulic cylinder to monitor the actuator pressure in the pressure control mode. Additionally, another pressure sensor was directly installed after the servo pump to monitor the source pressure. Moreover, a total of four linear potentiometers (LP-250FJ, Midori Precisions, Tokyo, Japan) were installed on each hydraulic cylinder to monitor the performance in the volume control mode. The experiment setup is illustrated in Fig. 3.13.

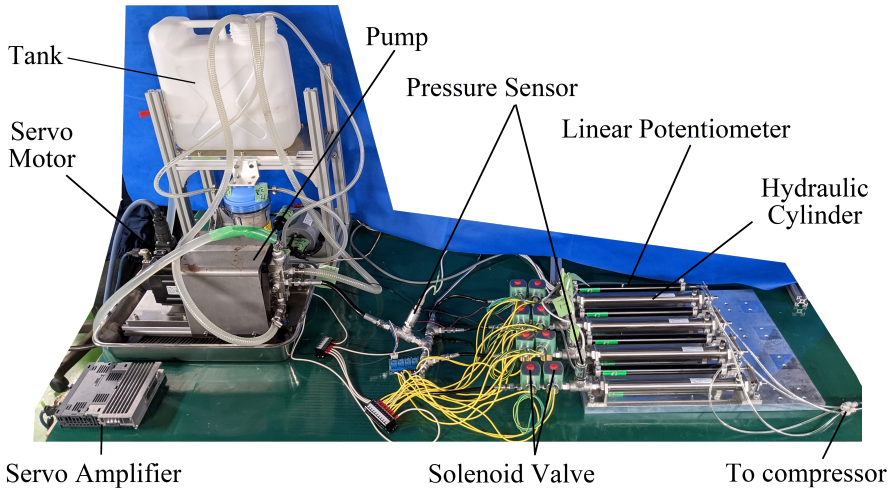

Figure 3.13: Experimental equipment. Controller and pneumatic equipment are not displayed herein.

3.6.2 Pressure Control

In the pressure control mode, all cylinders are in a fully-extended position, and the pneumatic pressure was disconnected.

APCS

For APCS, sinusoidal waveform was selected as the continuous source pressure waveform in the experiments. To test the system's effectiveness, all four permutations of rectangular and sinusoidal source pressure and reference signals, namely: R-R, R-S, S-R, and S-S were experimentally investigated.

In the R-R configuration with a constant duty ratio of 0.5, the RMSE was 0.61 MPa, which was lower than the simulated result of 1.21 MPa.

In the S-R configuration, the RMSE was 1.13 MPa, which was lower than 1.56 MPa in the simulations. For the rectangular setpoint modes, the sinusoidal source pressure offers a larger error and slower response compared to the rectangular source pressure. Furthermore, utilization of the dynamic duty ratio is not possible with a sinusoidal source pressure.

To demonstrate the performance of the APCS at a higher source frequency, experiments were also conducted between 1 Hz and 5 Hz. Increasing the source frequency to 5 Hz reduced the delay significantly as shown in Fig. 3.16. The RMSE

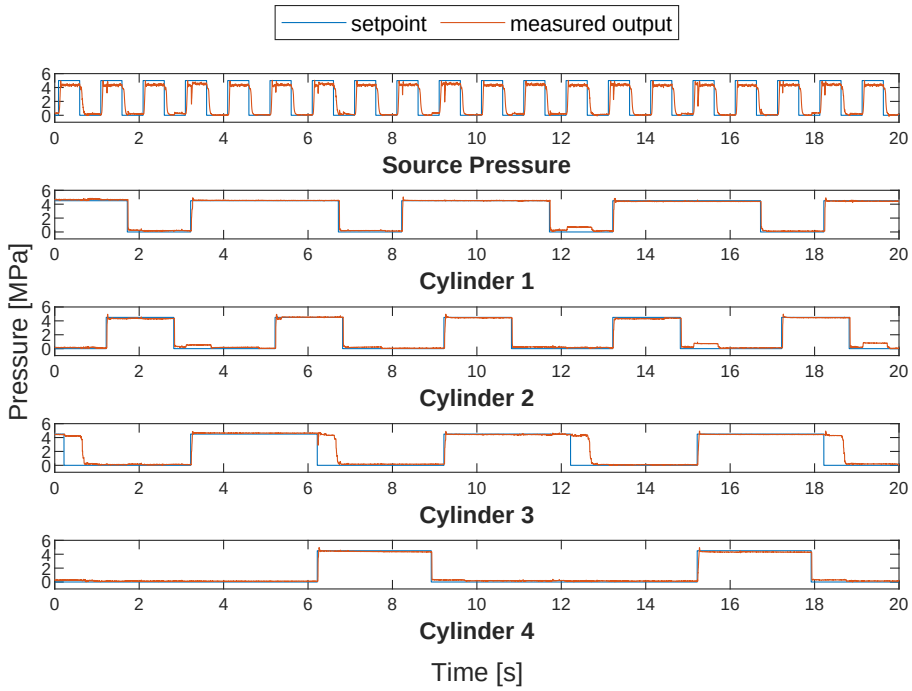

Figure 3.14: Experiment results in the R-R configuration with a 1 Hz source frequency and a 0.2 MPa deadband. This is an example of a suitable configuration.

at 5 Hz source frequency was 0.65 MPa.

Operation in the R-S configuration also returned a similar result for the simulation. The valves could not react to the sudden pressure change, resulting in a larger error compared to the S-S configuration. The delay and RMSE in the R-S configuration for an alternating source frequency of 1 Hz and a 0.2 MPa dead band were 0.29 s and 1.17 MPa, respectively.

Finally, in the S-S configuration with a frequency of 1 Hz and a 0.2 MPa dead band, the average RMSE and delay were 0.64 MPa and 0.32 s, respectively, as shown in Fig. 3.18. This is similar to the corresponding simulation results of 0.69 MPa and 0.30 s, respectively.

Increasing the source frequency reduced the delay. Unlike the simulation, however, the RMSE increased at a higher frequency. This was because the valves were slower in the experiments, resulting in a larger "overshoot" error as shown in Fig. 3.19. Moreover, the RMSE value also depends on the frequency of the setpoint signal. The RMSE of Cylinder 3, which has the slowest setpoint frequency, is significantly lower than that of Cylinder 4 which has the fastest setpoint frequency within the same configurations. The RMSE and delay values between 1 and 5 Hz with a

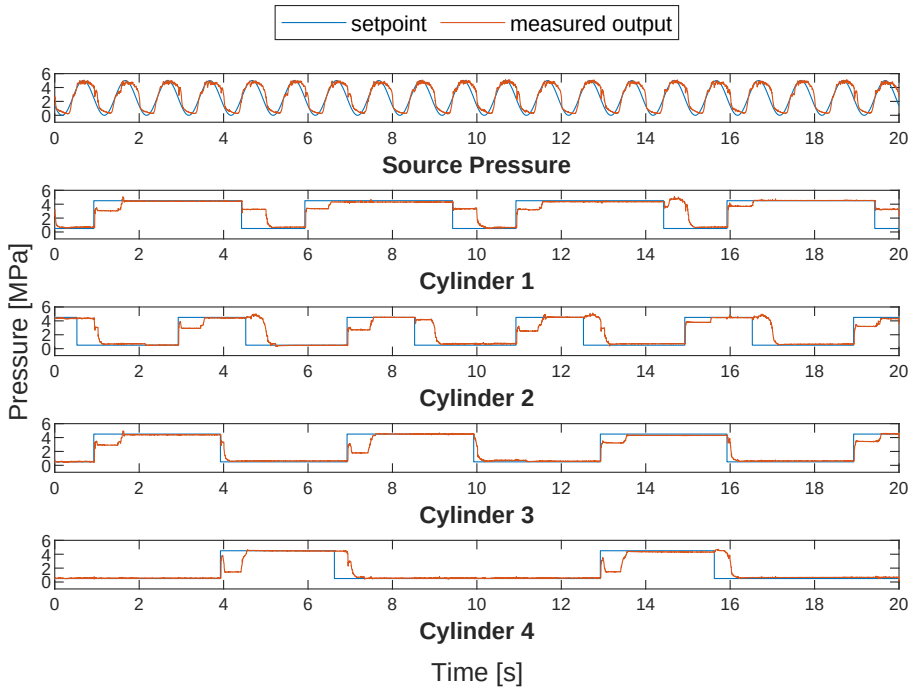

Figure 3.15: Experiment results in the S-R configuration with a 1 Hz source frequency and a 0.2 MPa deadband. This is an unsuitable configuration because sinusoidal source pressure has a slower pressure change, resulting in a larger error.

Table 3.4: RMSE and delay in S-S configuration from 1 Hz to 5 Hz. The dead band was 0.2 MPa.

Frequency (Hz)	1	2	3	4	5
Overall RMSE (MPa)	0.64	0.67	0.80	0.82	0.85
Cylinder 1 RMSE (MPa)	0.58	0.60	0.79	0.78	0.94
Cylinder 2 RMSE (MPa)	0.60	0.61	0.81	0.87	0.81
Cylinder 3 RMSE (MPa)	0.47	0.62	0.63	0.80	0.67
Cylinder 4 RMSE (MPa)	0.84	0.75	0.88	0.82	0.97
Overall delay (s)	0.32	0.17	0.14	0.11	0.13

0.2 MPa dead band are summarized in Table 3.4.

Increasing the source frequency beyond 5 Hz was not possible with current experimental equipment.

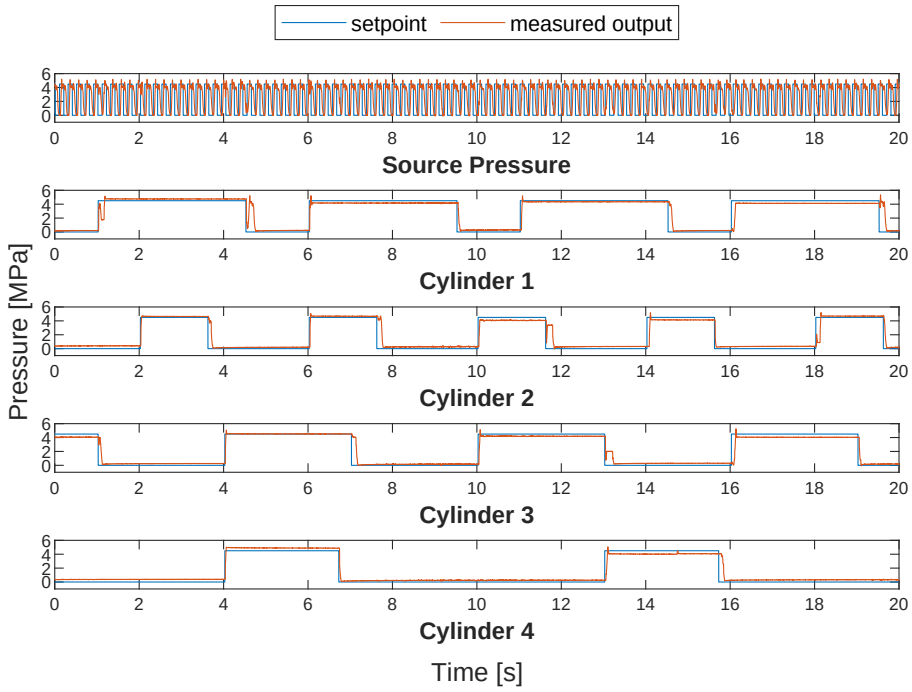

Figure 3.16: Experiment results in the R-R configuration with a 5 Hz source frequency and a 0.5 MPa deadband.

APCS with Load Disturbance

In this section, the performance of pressure-controlled APCS with external force acting on the cylinder rod is evaluated. The external force acting on the cylinder in the return direction was simulated by applying air pressure to the hydraulic cylinder. For the constant loading experiment, a constant pneumatic pressure of 0.75 MPa was applied to the cylinder, which is the equivalent of 172.5 N. For the dynamic loading experiment, a sinusoidal pneumatic pressure with an amplitude of 0.25 MPa, bias of 0.25 MPa, and angular velocity of 1.5 π rad/s was applied to the cylinder to simulate an external force between 0 to 115 N acting on the rod. The source pressure frequency and dead band in this section are 1 Hz and 0.2 MPa, respectively.

Adding disturbance to the system result in a slight increase in RMSE, with a larger error with dynamic disturbance as shown in Table 3.5. The errors in R-R configuration with disturbance are much higher than without disturbance but still lower than the simulated result without disturbance of 1.21 MPa. Experiment results in R-R configuration with dynamic disturbance are shown in Fig. 3.20.

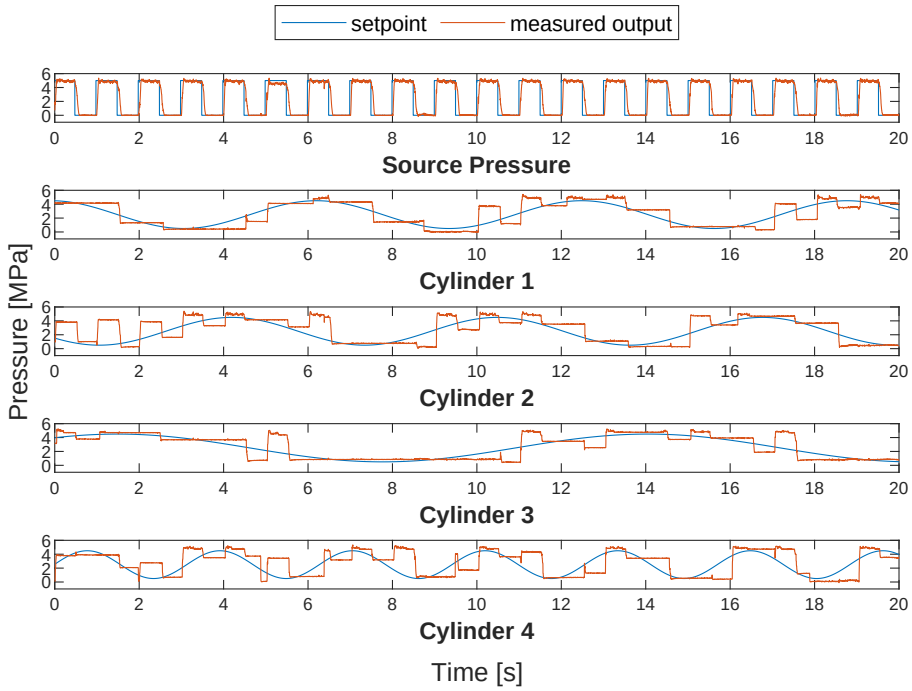

Figure 3.17: Experiment results in the R-S configuration with a 1 Hz source frequency and a 0.2 MPa deadband. Operation in this mode results in "overshoot" errors because the valves are not fast enough to react to the source pressure. This is an example of an unsuitable configuration.

Table 3.5: RMSE (MPa) in pressure control mode with external disturbance.

Mode	Disturbance		
	None	Constant	Dynamic
R-R	0.61	1.02	1.18
S-R	1.13	1.17	1.27
R-S	1.17	1.22	1.33
S-S	0.64	0.86	0.80

APCS-DDR

In this section, only the performance in R-R configuration was assessed as the dynamic duty ratio is only applicable to rectangular source pressure. Applying the dynamic duty ratio to the alternating pressure source reduced the total pump utilization time to 40.78% and increased the RMSE to 1.55 MPa. The increase in RMSE was due to the controller prioritizing the activation or deactivation of the

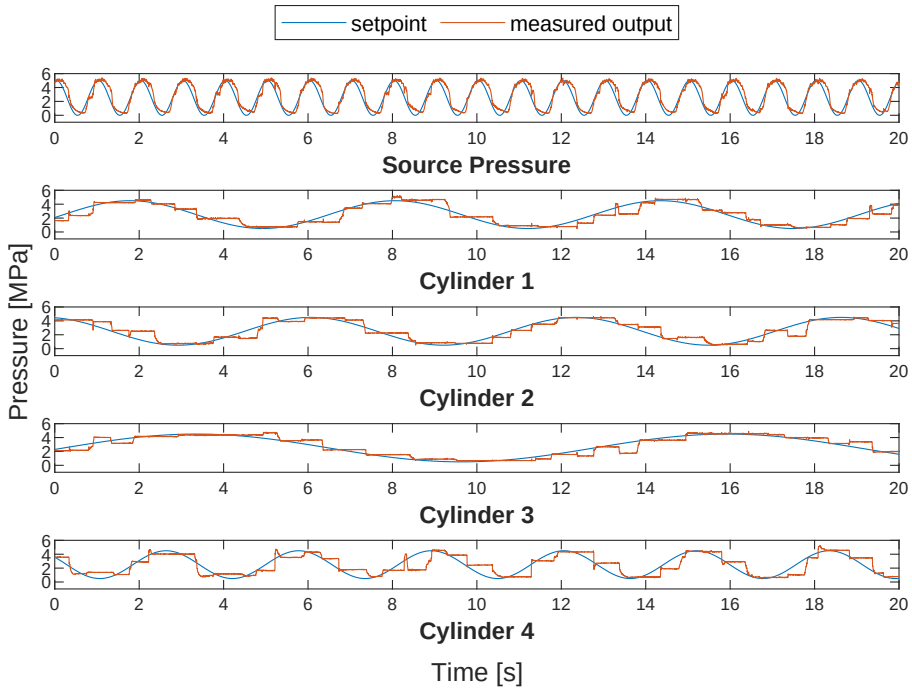

Figure 3.18: Experiment results in the S-S configuration with a 1 Hz source frequency and a 0.2 MPa deadband. This is an example of a suitable configuration.

actuator. For example, the error in Cylinder 1 in Fig. 3.21 between 12 and 13 s was due to the controller prioritizing the activation of cylinder 2 before updating the dynamic duty ratio at the 13 s mark. While this results in a larger error in this experimental setup where the cylinders are fixed, the dynamic duty ratio may improve performance in situations where cylinder rod movement is required.

Applying the dynamic duty ratio at a higher source frequency results in a significantly reduced pump utilization time to 21.96% at 3 Hz and 22.50% at 5 Hz source frequency as shown in Fig. 3.22. Moreover, the RMSE was also substantially reduced to 0.66 MPa. Utilizing the dynamic duty ratio at a higher source frequency results in a significantly reduced pump utilization time compared to the 50% of APCS with an insignificant impact on RMSE. The pump utilization percentage at different source frequencies is summarized in Table 3.6.

APCS-OL

In this section, only the system's ability to follow continuous pressure commands with different control strategies was assessed. Based on the findings from the previ-

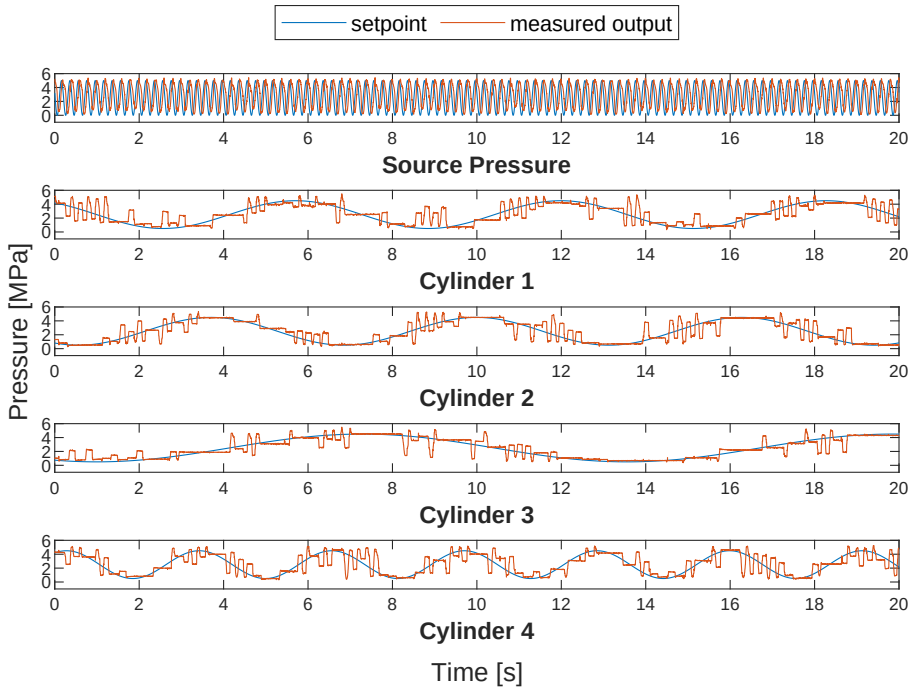

Figure 3.19: Experiment results in the S-S configuration with a 5 Hz source frequency and a 0.2 MPa deadband. The "overshoot errors" occurred due to the faster pressure change, similar to the R-S configuration. This is another example of an unsuitable configuration.

Table 3.6: Pump utilization time at different source frequency with the dynamic duty ratio.

Frequency (Hz)	1	2	3	4	5
Pump utilization (%)	40.78	28.62	21.96	21.89	22.50

ous section, only continuous waveforms were used as the source pressure waveform. However, the performance of additional continuous waveforms, namely triangle and sawtooth, were also investigated. The rectangular waveform was deemed unsuitable for continuous pressure command tracking and therefore not used in this section.

First, the experiment results of APCS-OL obtained at a source frequency of 2 Hz and an error band of 0.2 MPa with sinusoidal source pressure showed a comparable results to APCS as presented in Fig. 3.23.

Adopting the triangular wave as the oscillating pressure source instead of sinusoidal increases the viable frequency range, allowing a higher source frequency up

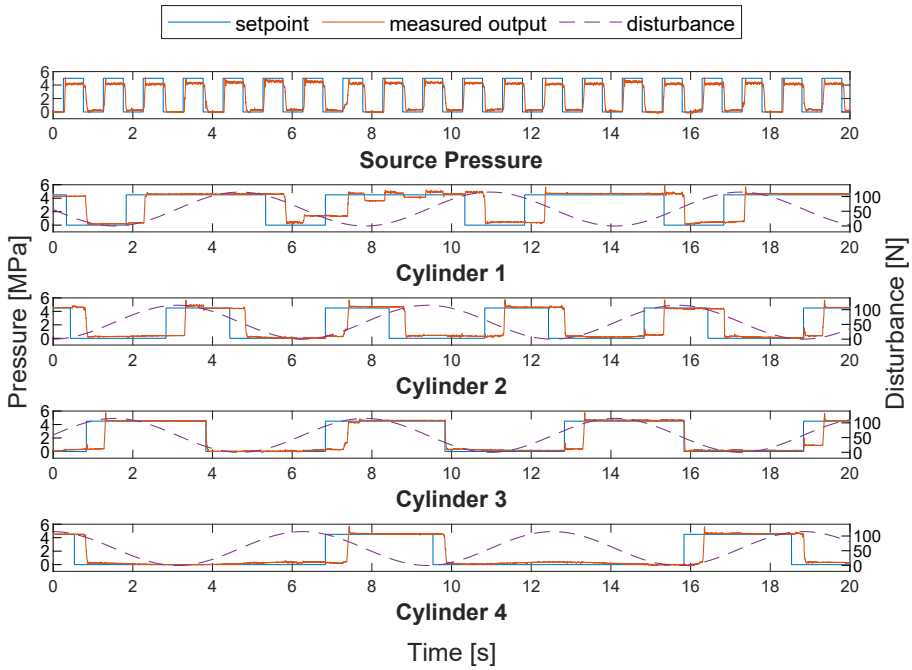

Figure 3.20: Experiment results in the R-R configuration with dynamic disturbances. The effects of disturbance can be seen most clearly in Cylinder 4.

to 4 Hz to be utilized. This improves the performance of the device, reducing both RMSE and delay. The experimental results at 4 Hz is presented in Fig. 3.24.

Increasing the source frequency above the viable range results in increased RMSE and delay owing to the limitations of the hardware implementation of the system, mainly the response of the pump and valve. This occurrence is most apparent with the application of a sawtooth source pressure at 5 Hz, as depicted in Fig. 3.25, where the servo pump could not reduce the source pressure to 0 MPa fast enough.

In contrast, for the sinusoidal source pressure at 5 Hz, the valves failed to react to the pressure variation adequately fast at the middle of the operating pressure range, as portrayed in Fig. 3.26.

The RMSE and delay of APCS-OL at multiple source pressure waveforms and frequencies are listed in Table 3.7.

MEHA

The pressure tracking capabilities of MEHA is depicted in Fig. 3.27. The settling period (t_{settling}) and valve closing period (t_{close}) for MEHA were 0.05 s and 0.02 s, respectively. Both the delay and RMSE of the MEHA reduced with a smaller

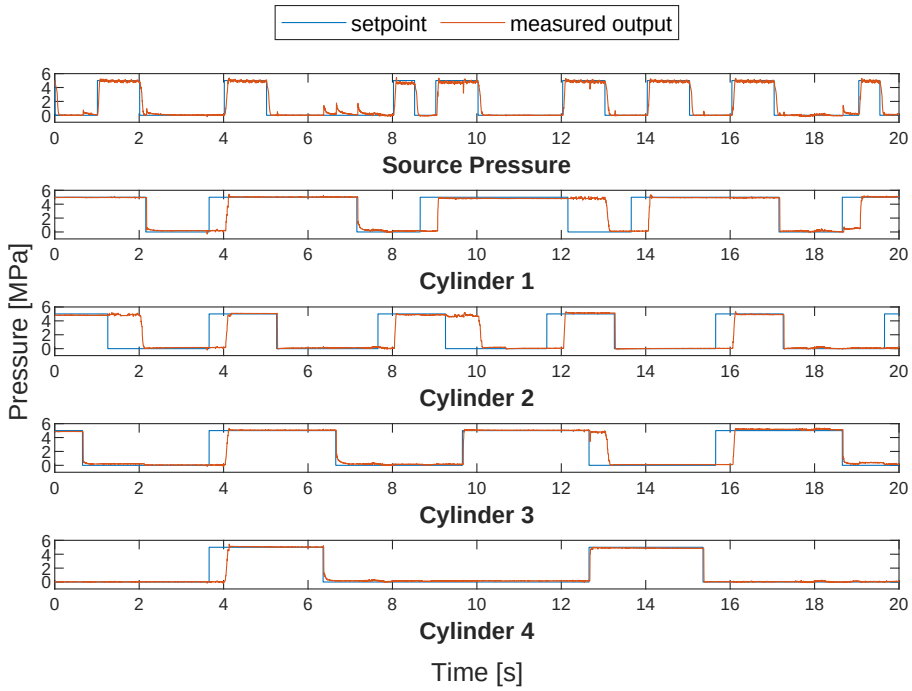

Figure 3.21: Experiment results in the R-R configuration including the dynamic duty ratio, with a 1 Hz source frequency and a 0.2 MPa deadband. The dynamic duty ratio reduces the pump utilization.

period up until $t = 0.08$ s. However, the period was nor further reduced owing to the constraints of t_{settling} and t_{close}. The experiment results are summarized in Table 3.8

Summary

The APCS, APCS-OL, and MEHA systems all demonstrated comparable performance. Specifically, the APCS and APCS-OL using sinusoidal source pressure produced similar results, while the APCS-OL with triangular source pressure produced the lowest RMSE and delay among all proposed systems. These findings suggest that the triangular waveform, which has a consistent slope, is the most suitable source pressure waveform. Although the use of an additional feedback sensor in APCS did not result in improved performance, it allowed for reduced energy consumption, such as in APCS-DDR.

In the current experiment setup, the MEHA system performed comparably to APCS. However, the MEHA system may perform even better with a lower number

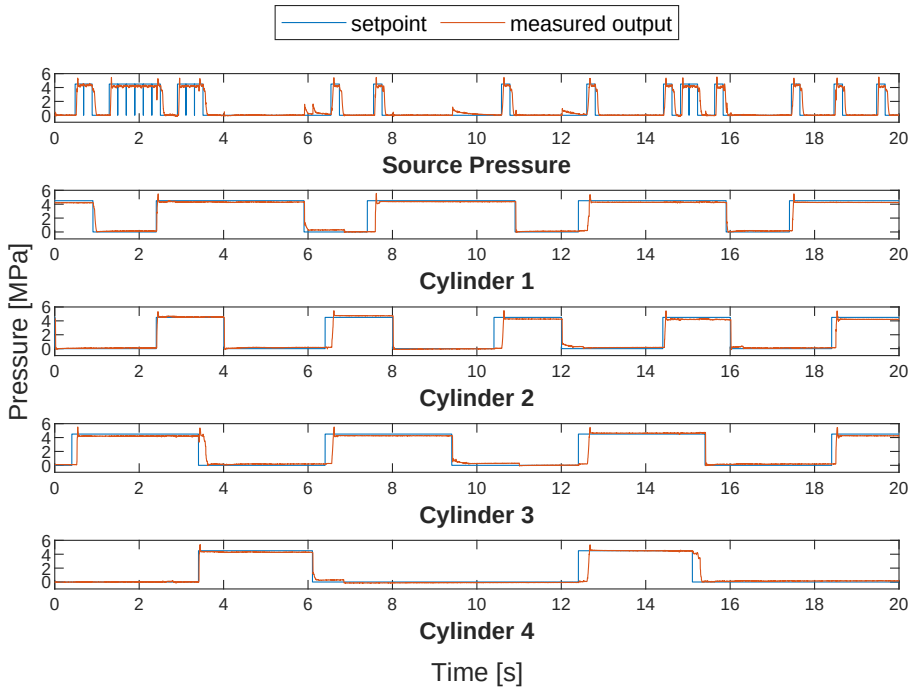

Figure 3.22: Experiment results of APCS-DDR with a 5 Hz source frequency and a 0.2 MPa deadband.

of actuators or by allowing for actuator movement, as MEHA is capable of achieving a better total system flow rate. The RMSEs and delays are summarized in Table 3.9.

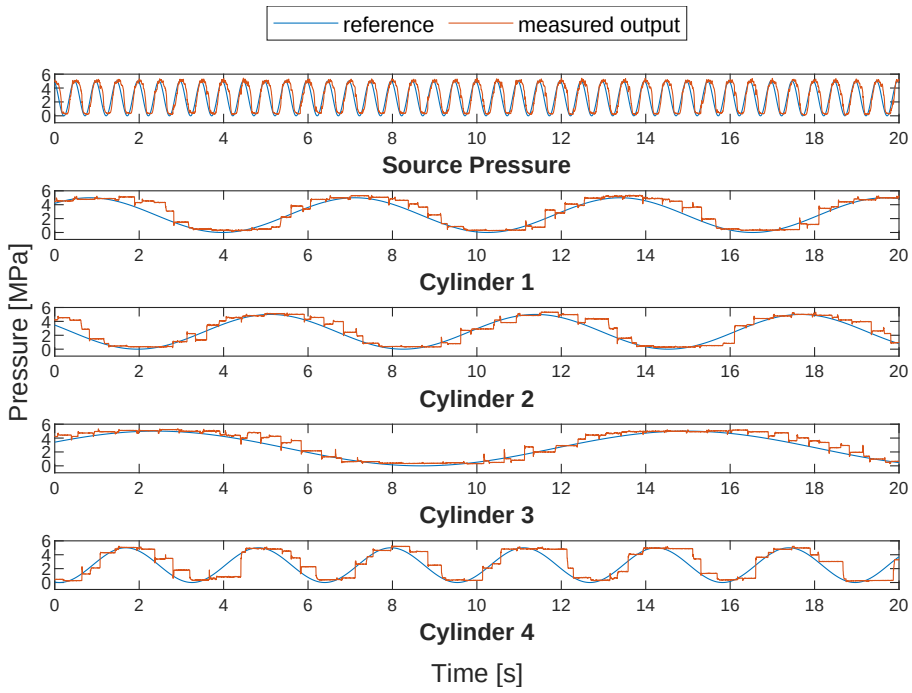

Figure 3.23: Experiment results of APCS-OL with sinusoidal reference signal and sinusoidal source pressure at source frequency of 2 Hz.

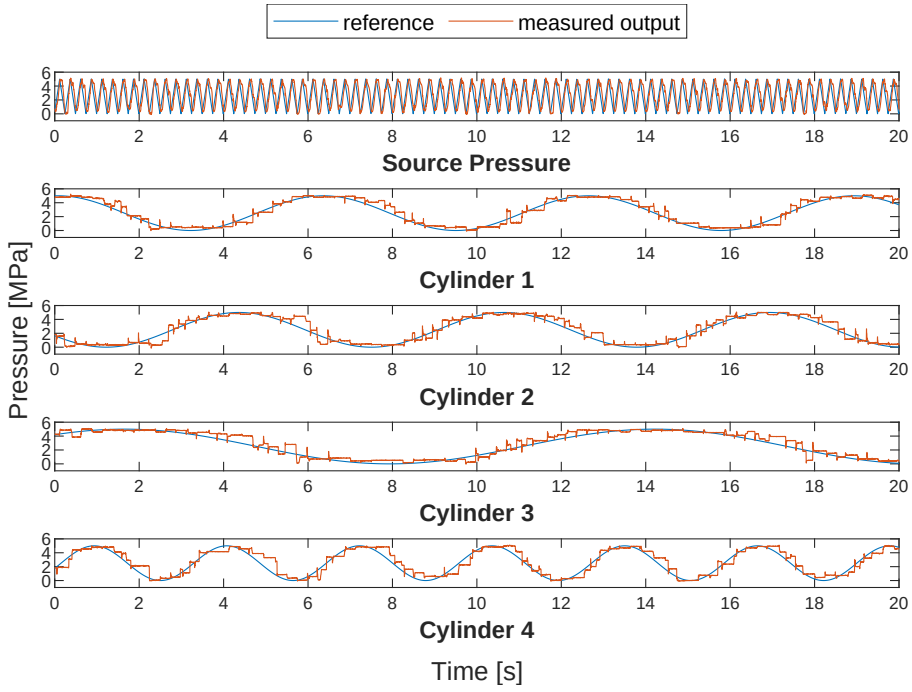

Figure 3.24: Experiment results of APCS-OL with sinusoidal reference signal and triangular source pressure at source frequency of 2 Hz.

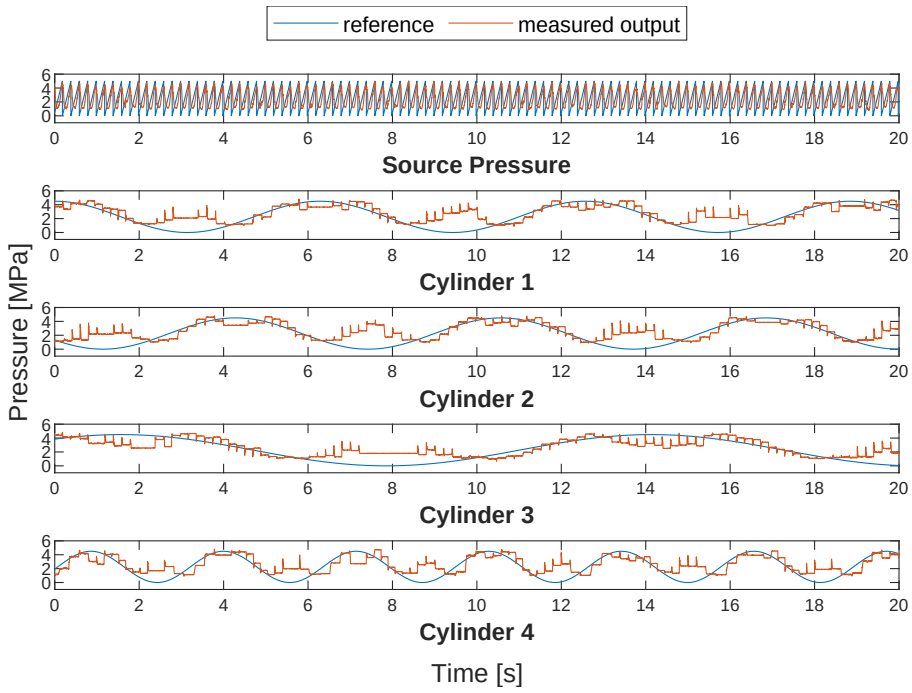

Figure 3.25: Experiment results of APCS-OL with sinusoidal reference signal and sawtooth source pressure at source frequency of 5 Hz.

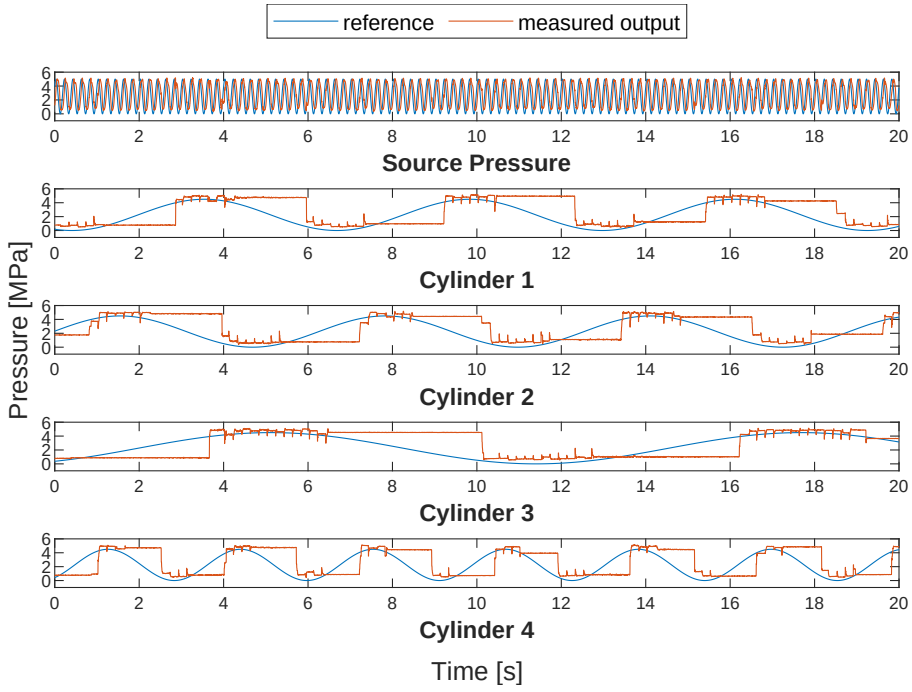

Figure 3.26: Experiment results of APCS-OL with sinusoidal reference signal and sinusoidal source pressure at source frequency of 5 Hz.

Table 3.7: Experiment results of APCS-OL in multiple configurations.

Source waveform	Frequency (Hz)	RMSE (MPa)	Delay (s)
Sinusoid	1	0.88	0.24
	2	0.75	0.19
	3	0.87	0.22
	4	1.29	0.67
	5	1.65	0.90
Triangular	1	0.90	0.26
	2	0.68	0.17
	3	0.57	0.12
	4	0.55	0.13
	5	0.74	0.18
Sawtooth	1	1.21	0.47
	2	1.02	0.26
	3	0.97	0.21
	4	1.10	0.18
	5	1.14	0.17

Table 3.8: Experiment results of MEHA in pressure control mode.

Period (s)	RMSE (MPa)	Delay (s)
0.2	0.88	0.34
0.1	0.67	0.22
0.08	0.64	0.24

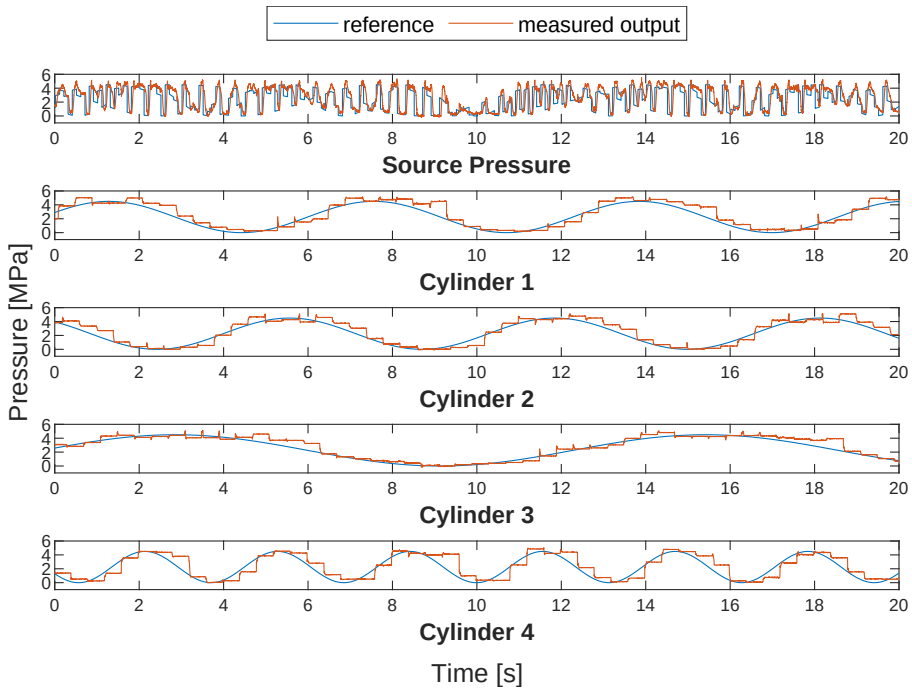

Figure 3.27: Experiment results of MEHA in pressure control mode with 0.1 s period.

Table 3.9: Comparisons between APCS, APCS-OL, and MEHA in pressure control mode.

System	Waveform	RMSE (MPa)	Delay (s)
APCS	Sinusoidal	0.64	0.32
		0.82	0.11
APCS-OL	Sinusoidal	0.75	0.19
	Triangular	0.55	0.13
		0.57	0.12
MEHA	N/A	0.64	0.24
		0.67	0.22

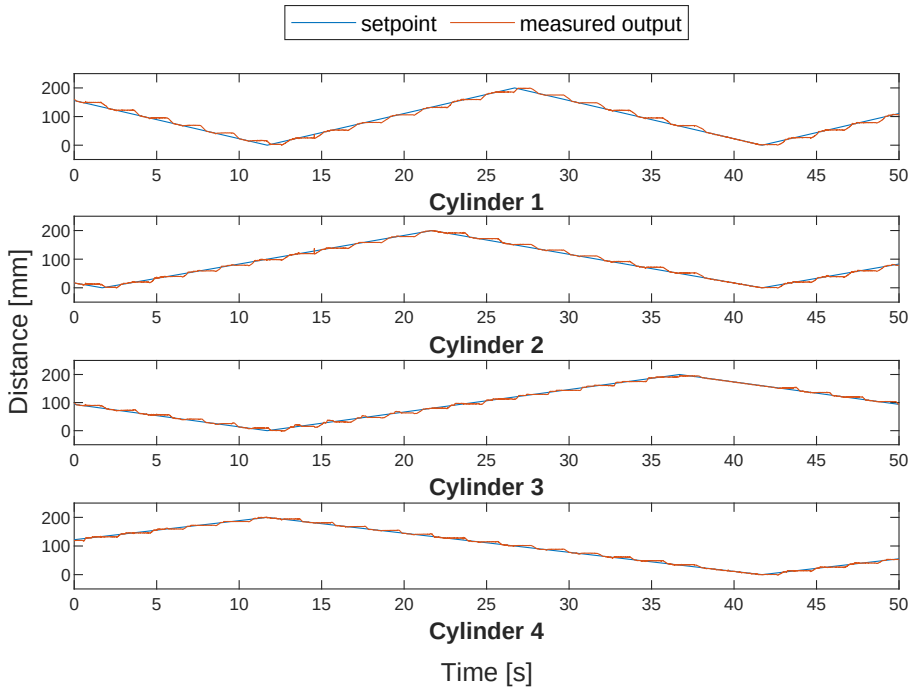

Figure 3.28: Experiment results in the volume control mode with a 1 Hz source frequency and 5 mm dead band.

3.6.3 Volume Control

In this section, volume control capabilities of the APCS and MEHA are evaluated experimentally.

APCS

The experiment of volume-controlled APCS with a 5 mm dead band also showed an RMSE of 4.90 mm. Moreover, changing the frequency or dead band gap showed no significant reduction in error in the experiment, as shown in Table 3.10.

In contrast, increasing both the frequency and the dead band gap resulted in a substantial reduction in the pump utilization time. At a source frequency of 3 Hz and a dead band gap of 10 mm, the pump utilization time was reduced to 26.07% as shown in Table 3.11.

MEHA

As indicated in Fig. 3.29 and Fig. 3.30, the MEHA could follow the reference command both in the periodic switching mode and hysteresis switching mode.

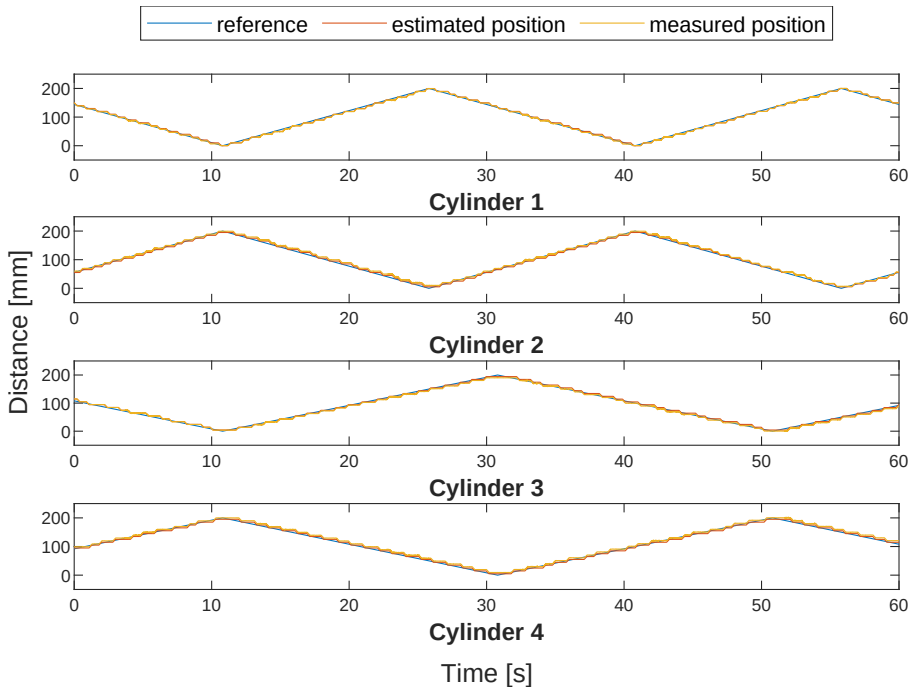

Figure 3.29: Experiment results of volume-controlled MEHA in periodic switching mode with 0.2 s period.

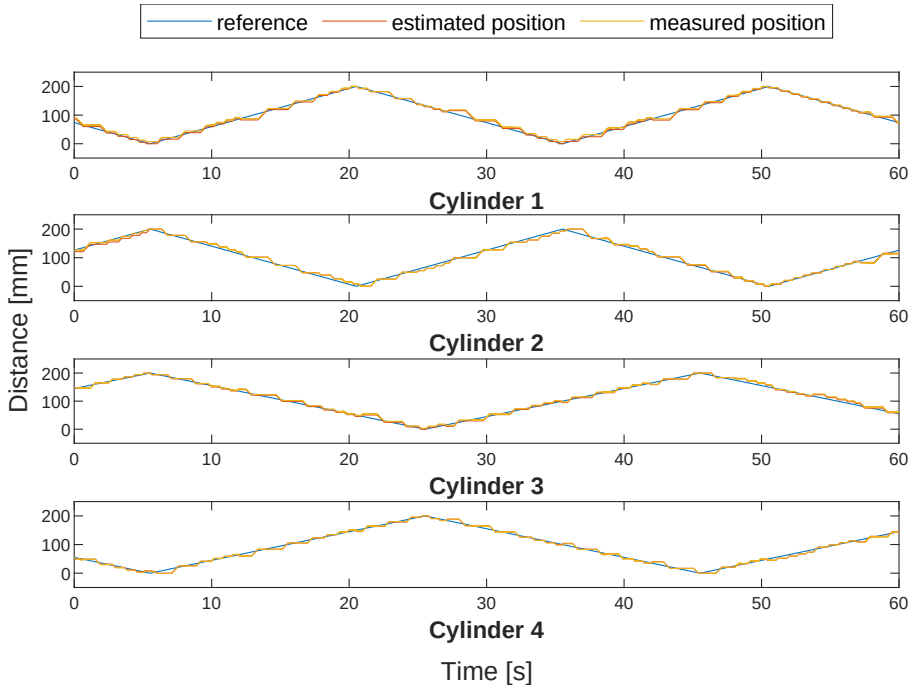

Figure 3.30: Experiment results of volume-controlled MEHA in hysteresis switching mode with error band of 5 mm.

Table 3.10: RMSE (mm) in volume control mode at different alternating source frequencies and dead band values.

Dead Band (mm)	Frequency (Hz)		
	1	2	3
0	4.45	3.03	4.99
5	4.90	3.54	3.29
10	5.51	4.53	4.48

Table 3.11: Pump utilization time (%) in the volume control mode at different alternating source frequencies and dead band values.

Dead Band (mm)	Frequency (Hz)		
	1	2	3
0	57.66	55.82	49.62
5	47.81	38.87	34.51
10	43.26	25.72	26.07

Table 3.12: RMSE of volume-controlled MEHA in periodic switching mode.

Period (s)	RMSE (mm)
0.5	12.04
0.2	5.05
0.1	7.25

Table 3.13: RMSE of volume-controlled MEHA in hysteresis switching mode.

Error band (mm)	RMSE (mm)
10	12.26
5	6.43
2	12.01

In case the period or error band is set smaller than the viable range, the RMSE increases because of the drifts, as observed in Fig. 3.31.

The RMSE in both mode are summarized in Tables 3.12 and 3.13, respectively.

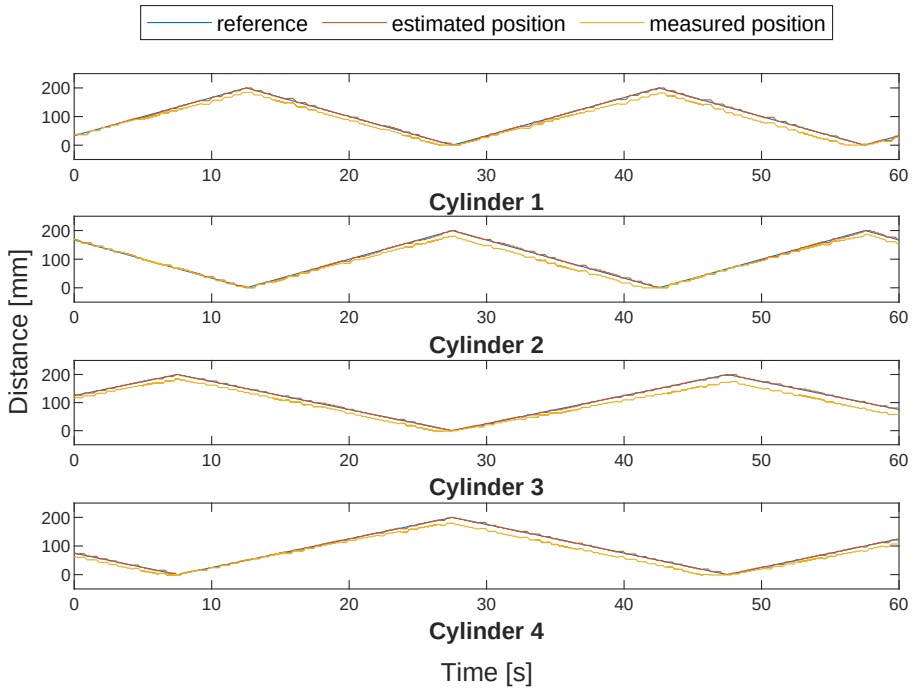

Figure 3.31: Experimental results of volume-controlled MEHA in hysteresis switching mode with error band of 2 mm.

3.7 Discussion

The main advantages of the proposed system in this chapter is reduced hydraulic losses compared to traditional centralized systems, and reduced weight compared to using multiple EHAs in multi-DoF systems. The main reduced hydraulic losses are in the form of throttling loss, which is reduced through the adoption of on–off valve for switching with servo pump. In addition, the application of the dynamic duty ratio in APCS further reduces pump utilization as shown in Table 3.6. In contrast, MEHA only needs to be activated when required, reducing standby power consumption similar to traditional EHAs.

Previous studies aiming to reduce energy losses in hydraulic systems have proposed several solutions, including structural modifications to the pump, as well as the inclusion of additional components such as control valves, a converter, a compensator, or accumulators [114]. However, this results in increased system complexity, and the additional components introduce extra weight and size, which may not be possible in certain applications. In contrast, the proposed system eliminates the need for a feedback sensor and utilizes simpler on–off valves. This reduction in

complexity not only streamlines the system but also reduces its weight, making it suitable for exoskeletons.

Comparing the system weight of the proposed system to multiple EHAs with a similar total power, two main components in the hydraulic power units needs to be considered: pump and motor. Sakama et al. [75] reported that power of hydraulic motors are proportional to its weight. Considering that hydraulic motors and pumps are theoretically interchangeable, a similar power-to-weight trend can also be expected for hydraulic pumps. This means that in systems with an equivalent total power, the weights of a centralized pump and multiple decentralized pumps should be similar. In practice, the power requirement for a centralized pump will generally be lower than the sum of the maximum power of all actuators, resulting in the potential for further weight reduction.

Conversely, the output power of electric motors is proportional to 4/3 power of motor weight [75]. This implies that using a centralized motor with an equivalent power to the motors in all EHAs combined, the total system weight will be 3/4 power that of EHAs. In other words, the motor weight, m, of a proposed centralized system with n DoF is $m \propto n^{3/4}$ which is lower $m \propto n$ of decentralized EHAs. This results in up to a 40% weight reduction with 8 actuators as shown in Fig. 3.32.

Additional weight reduction can be achieved with the proposed system if all actuators are not required to operate at maximum power simultaneously, as the centralized power unit only needs to be capable of total system load. In contrast, employing multiple EHAs is the requirement for each actuator to be capable of bearing its maximum load. For example, systems with sporadic spike loads may necessitate excessively large EHAs, adding unnecessary weight. Conversely, a centralized system only requires the centralized power unit to be capable of handling the maximum load, thereby reducing excessive weight.

However, the most significant advantage of the proposed system for wearable robots is that it eliminates the need for heavy components to be installed directly on the limb. When compared to EHAs, the proposed system offers a distinct advantage in terms of weight distribution. With EHAs, all the necessary components, including the pump and tank, are combined into a single unit mounted on the limb. This can introduce substantial weight and inertia directly onto the limb, affecting the user's movement and overall agility. In contrast, the proposed system allows heavier components, such as the pump and tank, to be placed remotely instead of directly on

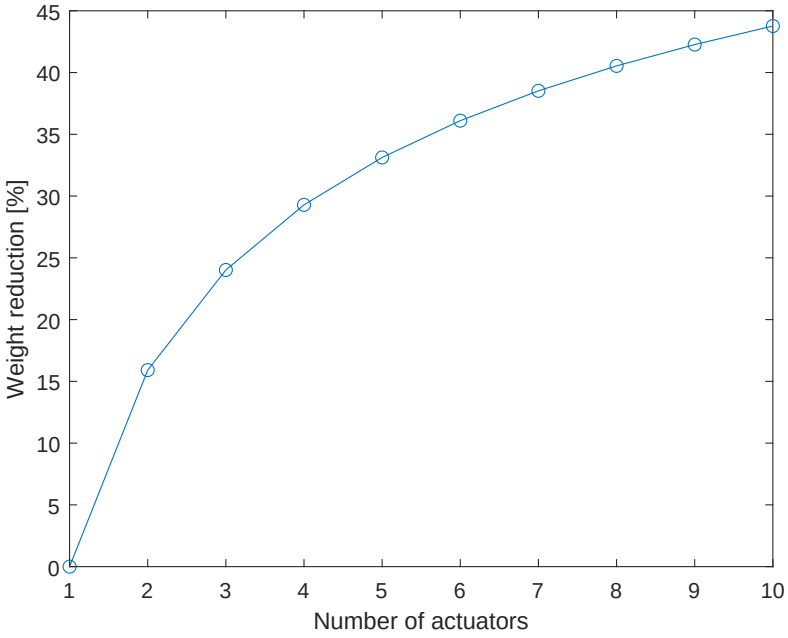

Figure 3.32: Weight reduction of a centralized system compared to decentralized EHAs.

the limb. This reduces the inertia experienced by the limb, enhancing the wearer's ability to move and perform tasks without being hindered by excessive weight or inertia.

The main disadvantages of both MEHA and APCS is the inherently lower performance compared to both conventional centralized system and EHAs, as smooth operation is not possible due to channel-switching. Furthermore, the proposed systems also have limitations in countering external disturbances when the valves are closed, which restricts their application in situations where sudden spikes of disturbances occur. Additionally, the operating pressure range of both systems is relatively low.

Therefore, the proposed system holds potential for applications in wearable robots where weight and efficiency outweigh the comparatively lower operating pressure and low disturbance. While the current prototypical implementation may be too large for mobile applications, future improvements hold the potential to downsize the system, making it suitable for mobile exoskeletons. Other types of robots which benefit from these advantage includes mobile robots such as walking robots. Furthermore, the proposed system, when used at higher pressure ratings, has the

potential for applications where smooth motion, instantaneous response, or frequent channel switching is not essential. One such application is in jack-up systems for structural adjustment, where rapid or continuous motion are not required.

3.8 Chapter Summary

This chapter proposes a novel hydraulic system for multi-DoF hydraulic exoskeletons which simplifies hydraulic components of conventional centralized hydraulic systems. Instead of using resistance control as often used in conventional valve-controlled constant pressure system, a centralized motor-controlled system with on–off valve is proposed. The on–off valves which are smaller and lighter than traditional pressure control valve and flow control valve allows reduction of system weight. Furthermore, the proposed systems also allow omission of feedback sensor, further simplifying the components.

To allow pressure and volume control of each individual actuator with a centralized servo pump, we propose two control algorithms, namely APCS and MEHA. In APCS, the pump generates a constantly oscillating pressure source. The controller then opens or closes the valves accordingly. In contrast, the valves in MEHA opens or closes periodically. The pump then generates an appropriate pressure or flow to the active actuator. Additional variants of the APCS, namely APCS-DDR and APCS-OL were also proposed to enhance system performance in specific cases. APCS-DDR allows reduced pump utilization and improved power consumption in R-R configuration. On the other hand, APCS-OL omits pressure feedback from the system, further reducing system weight.

Experiments were conducted to evaluate performance of the proposed algorithms. All proposed algorithms were able to track both pressure and volume commands at the cost of a minor error and delay compared to conventional system. Performance of various source pressure waveforms were also evaluated, with the triangular wave offering best performance for continuous pressure command tracking.

The hydraulic system proposed in this chapter allows for weight and size reduction for multi-DoF hydraulic systems, both of which are crucial in hydraulic-powered exoskeletons. This allows development of a multi-DoF exoskeleton, which will be discussed in the next chapter.

Chapter 4

Stair Climbing Exoskeleton

In this chapter, a multi-DoF dual-limb knee exoskeleton for stair climbing assistance based on the exoskeleton introduced in Chapter 2 and the hydraulic system proposed in Chapter 3, is presented. To meet the higher torque requirements of stair climbing, a dual four-bar linkage mechanism with a HAM on each side of the knee is proposed. In order to allow for internal rotation of the knee, a novel dual asymmetric link mechanism was adopted. The parameters of the four-bar linkage mechanism were optimized using a genetic algorithm (GA) to match the kinematics of the knee joint on both the lateral and medial sides. The experiment results found that the proposed device has improved comfort compared to the traditional revolute joint and is effective at reducing muscle activities during SC.

4.1 Dual Four-Bar Linkage Mechanism

In this chapter, an ergonomic dual four-bar linkage exoskeleton is proposed. In Chapter 2, STS was selected as the first target for assistance to evaluate the feasibility of combining the HAM and the four-bar linkage mechanism. The knee torque profile required for STS and the force-contraction characteristics of the HAM are similar, making the implementation simpler. To evaluate the effectiveness of the proposed method in a more complex action, stair climbing was selected as a "complex ADL" due to the following reasons:

1. DoF increase: SC requires the use of both legs, resulting in increased number of required DoF

2. Higher torque requirement: the body weight is supported only by one leg in SC instead of two in STS. Moreover, the higher torque requirement amplifies discomfort due to misalignment.

3. Complex knee torque profile: SC has an increasing-decreasing torque profile which is different from the force-contraction relationship of the HAM, making the implementation of the linkage mechanism more complex.

The increase in DoF can be achieved using the multi-DoF hydraulic system proposed in Chapter 3. To meet the higher torque requirement and accommodate the complex knee torque profile, a two-side-support layout is adopted. This allows the exoskeleton to provide assistive torque from both the medial and lateral sides of the leg, potentially doubling the torque output. The two-side-support design also improves pHRI by reducing the undesired twisting force, which improves force transmission efficiency and reduces misalignment.

The proposed mechanism accounts for the asymmetricity of the femoral condyle by reproducing the displacement of the GCA on the lateral and medial sides relative to the tibia at any orientation using two separate link mechanism. As the medial-lateral translational motion of the tibia is relatively small, it is assumed to be negligible, and the three-dimensional motion of the tibia is approximated using two planar four-bar linkage mechanisms on the medial and lateral sides of the knee. The three anatomical axes, including the GCA, are shown in Fig. 4.1, and their movement patterns on the medial and lateral sides are shown in Fig. 4.2

Previous research efforts focused on developing optimal ergonomic four-bar linkage mechanisms aiming to replicate the centrode or axoid of the anatomical knee joint. However, this approach has been found to be prone to error, as both the tangent method and the Reuleaux method used to determine the centrode or axoid are sensitive to measurement errors. Furthermore, small errors in the centrode or axoid can accumulate to a large final translation error due to the instantaneous nature of the ICR and IHA.

As a result, this section proposes a novel four-bar linkage mechanism that aims to replicate the translational displacement of an anatomical axis at any orientation relative to the tibia, rather than replicating the centrode or axoid of the knee. The proposed mechanism achieves this by selecting the GCA as the target axis, which has the lowest proximal–distal translation. It is important to note that any arbitrary

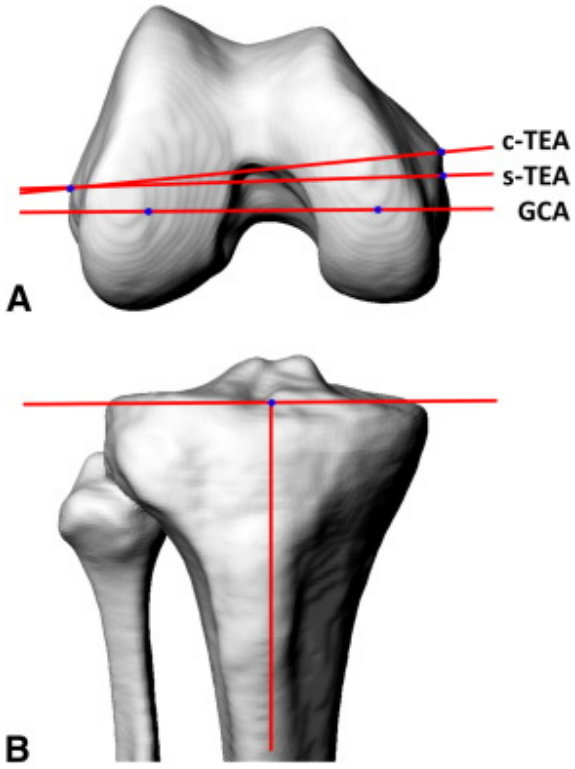

Figure 4.1: (A) Axial view of the right femur and (B) coronal view of the right tibia. The clinical transepicondyle axis (c-TEA) connects the most prominent points of the lateral and medial epicondyles. The surgical transepicondyle axis (s-TEA) connects the lateral epicondylar prominence and the medial sulcus of the medial epicondyle. The geometric center axis (GCA) connects the centers of the spheres fitting to the lateral and medial posterior femoral condyles. From [43].

axis can also be used in a similar design method. For consistency with Chapter 2, the kinematics of the knee was transformed to the moving tibia on a stationary femur coordinates. By focusing on replicating the translational displacement of the anatomical axis, this mechanism provides a more accurate representation of the knee joint's movement, reducing potential measurement errors.

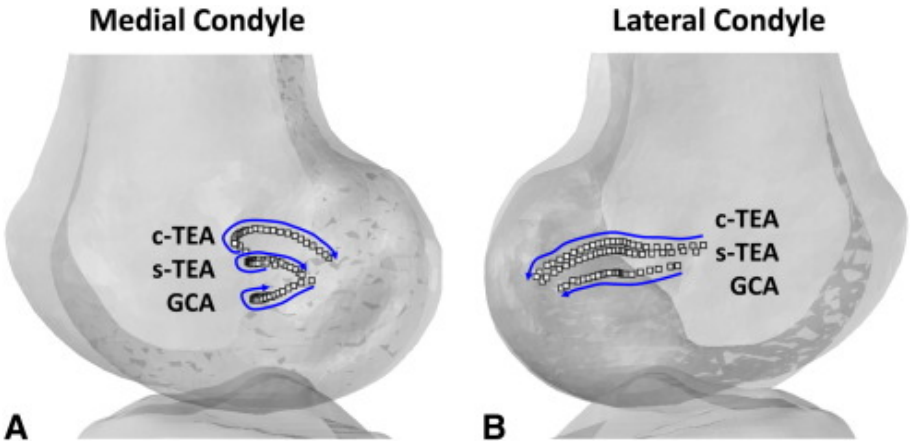

Figure 4.2: Movement patterns of (A) medial and (B) lateral femoral condyles in three dimensional spaces during a dynamic flexion motion measured using three different anatomical axes. From [43].

4.1.1 Four-bar Linkage

In this chapter, the four-bar linkage mechanism was solved using Freudenstein's Equation [115] instead of the method introduced in Chapter 2. Freudenstein's Equation allows the positions of each link to be solved as a function of angle of the coupler link. The linkage mechanism was designed in moving tibia on the fixed femur coordinate.

Consider the four-bar linkage consisting of four rigid links connected by four revolute joints shown in Fig. 4.3. Following the notation in Chapter 2, let the initial position of the joints be denoted by A, B, C, and D, and let the angles of the links AB, BC, CD, and AD be denoted by θ_1, θ_2, θ_3, and θ_4, respectively. Next, r_1, r_2, r_3, and r_4 corresponds to the lengths of link AB, BC, CD, and AD respectively. The link AD represents the stationary femur link, while link BC represents the moving tibia. Point P denotes the coupler point which traces the path of the tibia plateau.

The flexion angle of the knee joint, denoted by θ_{knee}, is given by the difference of angle of the tibia link and its initial angle ($\theta_{2,0}$):

$$\theta_{\text{knee}} = \theta_2 - \theta_{2,0}. \tag{4.1}$$

To solve for positions of the links as a function of the knee angle (θ_{knee}), either angle θ_1 or θ_3 must a be solved as a function of θ_2.

First, summing the vectors along the direction of vector $\overrightarrow{AD}$ results in the fol-

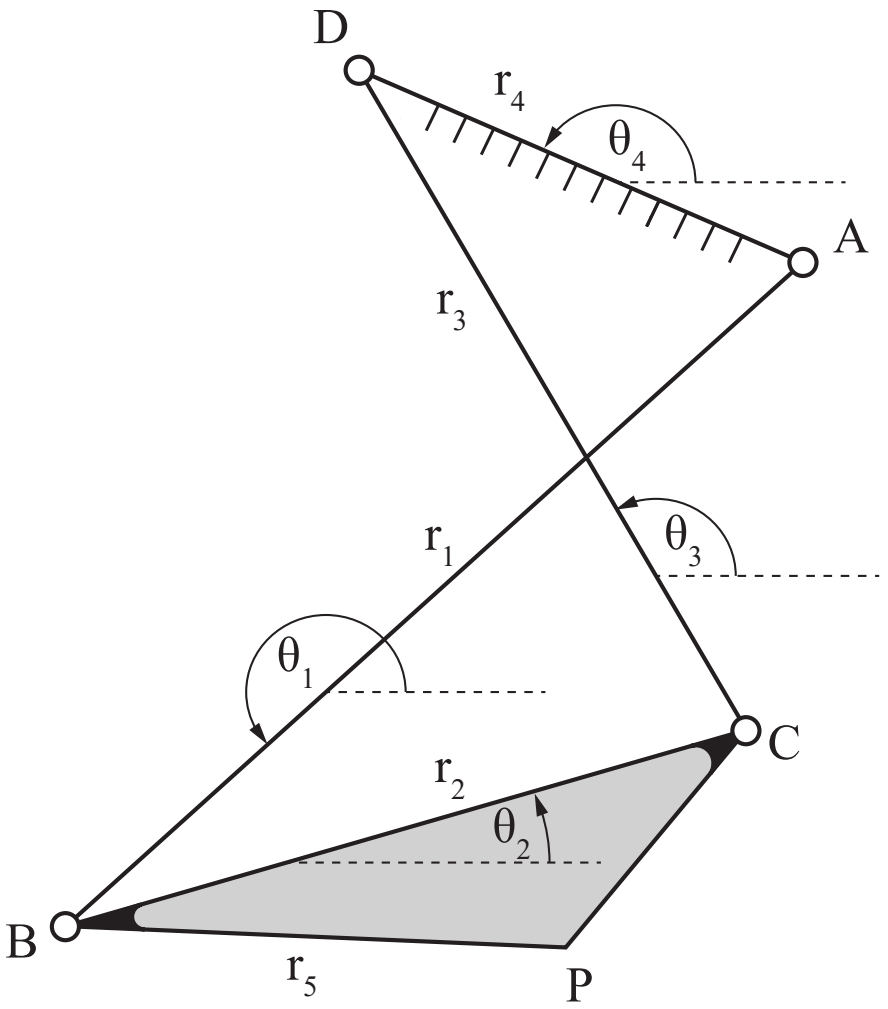

Figure 4.3: A crossed four-bar linkage mechanism.

lowing equation:

$$r_4 = r_1 \cos(\theta_1 - \theta_4) + r_2 \cos(\theta_2 - \theta_4) + r_3 \cos(\theta_3 - \theta_4) \tag{4.2}$$

Next, summing the vectors perpendicular to the vector $\overrightarrow{AD}$ results in

$$0 = r_1 \sin(\theta_1 - \theta_4) + r_2 \sin(\theta_2 - \theta_4) + r_3 \sin(\theta_3 - \theta_4). \tag{4.3}$$

Separating the terms with r_3 to eliminate $\cos(\theta_3 - \theta_4)$ and $\sin(\theta_3 - \theta_4)$, we get

$$r_3 \cos(\theta_3 - \theta_4) = r_4 - r_1 \cos(\theta_1 - \theta_4) - r_2 \cos(\theta_2 - \theta_4) \tag{4.4}$$

$$r_3 \sin(\theta_3 - \theta_4) = -r_1 \sin(\theta_1 - \theta_4) - r_2 \sin(\theta_2 - \theta_4). \tag{4.5}$$

Summing the square of Eq. 4.4 and Eq. 4.5 resulting in the following equation:

$$\begin{aligned} 0 =& \frac{r_4^2 + r_1^2 + r_2^2 - r_3^2}{2r_1r_2} - \frac{r_4}{r_2}\cos(\theta_1 - \theta_4) - \frac{r_4}{r_1}\cos(\theta_2 - \theta_4) \\ &+ \cos(\theta_1 - \theta_4)\cos(\theta_2 - \theta_4) + \sin(\theta_1 - \theta_4)\sin(\theta_2 - \theta_4) \end{aligned} \tag{4.6}$$

Equation 4.6 can be rewritten as

$$k_3\cos(\theta_2 - \theta_4) - k_1 = (\cos(\theta_2 - \theta_4) - k_2)\cos(\theta_1 - \theta_4) + \sin(\theta_1 - \theta_4)\sin(\theta_2 - \theta_4), \tag{4.7}$$

where:

$k_1 = \frac{r_4^2+r_1^2+r_2^2-r_3^2}{2r_1r_2}$,

$k_2 = \frac{r_4}{r_2}$,

$k_3 = \frac{r_4}{r_1}$.

Since the angle θ_4 is constant, solving the angle θ_1 as a function of θ_2 will allow the four-bar linkage to be solved at any knee joint angle. The solution of Eq. 4.7 is given below.

$$\theta_1 = \operatorname{atan}\left(\frac{k_4k_6 \pm k_5k_7}{k_5k_6 \mp k_4k_7}\right) + \theta_4 \tag{4.8}$$

where:

$k_4 = \sin(\theta_2 - \theta_4)$,

$k_5 = \cos(\theta_2 - \theta_4) - k_2$,

$k_6 = k_3\cos(\theta_2 - \theta_4) - k_1$,

$k_7 = \sqrt{k_4^2 + k_5^2 - k_6^2}$.

This will allow point B, and subsequently, point C and P, of the four-bar linkage mechanism to be found at any angle of the coupler link.

4.1.2 Optimization

To accurately generate the trajectory of the anatomical axis using four-bar linkage mechanism, an optimization method is necessary as it is not possible to solve for the optimal value directly. The objective of this optimization is to minimize the error between the biomechanical trajectory and the trajectory generated by the coupler point in the four-bar linkage mechanism.

To achieve this objective, the Euclidean distance between the translational displacement of the two trajectories is minimized at any orientation. This approach ensures that the coupler point of the four-bar linkage mechanism replicates the translational displacement of the anatomical axis accurately, reducing potential errors in the generated trajectory. The problem can be formulated as an optimization problem as:

$$\begin{aligned} \underset{x}{\text{minimize}} \quad & \sum_{i=0}^{\theta_{\max}} \|f_P(\mathbf{x}, i) - \mathbf{P}_{\text{knee},i}\| \\ \text{subject to} \quad & \mathbf{P}_{\text{knee}} \in \mathbb{R}^2 \\ & -50 \preceq A \preceq 50 \\ & -50 \preceq B \preceq 50 \\ & -50 \preceq C \preceq 50 \\ & -50 \preceq D \preceq 50 \end{aligned} \tag{4.9}$$

where:

$\mathbf{x}$ denotes the optimization variable vector containing initial position of points A, B, C, and D,

f_P denotes the function of point P of the four bar linkage,

$\theta_{\max}$ denotes the maximum knee flexion angle, and

$\mathbf{P}_{\text{knee},i}$ denotes position vector of the biological knee joint at angle i.

The maximum and minimum values of joint positions are in place to avoid a bulky and unfeasible solution. Since the objective function of the optimization is nonconvex, a global optimization technique is required. With a total of eight optimization variables, using grid search to brute force for the optimal values is no longer feasible. In this chapter, the parameters were first optimized using GA, then the optimization results were further fine-tuned using quasi-Newton method.

Genetic Algorithm

The GA is a global optimization technique that draws inspiration from the principles of natural selection and evolution. It falls within the broader class of evolutionary algorithms, which are widely used for solving complex optimization problems. GA, in particular, is a popular method for optimizing a four-bar linkage mechanism.

The GA operates by emulating the mechanics of natural selection in a population of potential solutions. It begins with an initial randomized population of individuals, each representing a potential solution to the optimization problem. Each candidate solution has a set of properties which is equivalent to chromosomes in biological evolution. The GA then utilizes biologically inspired operators such as selection, crossover, and mutation to simulate the processes of genetic variation and natural selection to modify these chromosomes.

The population first undergoes the selection process, where each individual are evaluated and selected through a fitness-based process. A portion of the population is then selected to reproduce a new generation, where fitter candidate solution is more likely to be selected. This allows the optimization process to gradually improving the overall fitness of the population, eliminating characteristics from less-fit individuals. Other techniques, such as elitism, may also be utilized to guarantee that a small portion of the best individuals are selected and carried over to the next generation.

The next step is the crossover process, which is analogous to sexual reproduction in biology. During this process, two "parent" solutions are selected for breeding from the pool of selected individuals. A new "child" solution is created from genetic recombination of parent solutions, creating a new individual which inherited many characteristics from both parents. This process is repeated until a new pool of population with an appropriate size is generated.

In addition to the crossover process, random changes are also introduced into the genetic makeup of individuals through mutation. The mutation operators are used to avoid local minima, and allowing the population to better explore the search space. Without mutation, the population may become too similar to each other, and stop converging towards the global minimum.

The selection, crossover, and mutation steps are subsequently executed iteratively, progressively enhancing the overall fitness of the population until one of the termination conditions is met. These conditions usually involve the discovery of a solution that meets the minimum criteria, the completion of a fixed number of generations, or the fitness of the highest-ranking solution reached a plateau, and further iterations no longer yield superior outcomes.

The GA is a suitable optimization method for four-bar linkage design due to its ability to effectively explore a large design space and find optimal or near-optimal

solutions. Four-bar linkage design involves determining the lengths of the links and the initial joint angles to achieve specific motion requirements. The design space for these variables can be vast and highly nonlinear. The GA's ability to explore a wide range of design possibilities allows it to search for solutions in this complex space, considering various combinations of initial link positions.

One of the major advantages of the GA is its global search capabilities. Four-bar linkage design optimization is typically a nonlinear and nonconvex problem, where the relationship between the design variables and the objective function can be highly complex and involve multiple local optima. The GA's ability to simultaneously explore different regions of the design space helps overcome these challenges by avoiding convergence to a local minima and enabling the discovery of globally optimal or near-optimal designs.

In addition to exploring the design space, the GA is well-suited for handling constraints commonly encountered in four-bar linkage design. Constraints, such as limits on link lengths or joint angles, are necessary to ensure mechanical feasibility. The GA can incorporate these constraints into the design process. This allows the GA to generate feasible linkage designs that satisfy the required constraints, ensuring that the resulting solutions are physically realizable.

However, the main disadvantage of GA is its computational cost: The GA can be computationally intensive. This is especially for complex four-bar linkage design problems, where a relatively large number of population is preferred. As the size of the design space increases or when dealing with high-dimensional problems, the time required to evaluate fitness functions and perform genetic operations (selection, crossover, and mutation) can become significant.

Furthermore, the results obtained from GA is not guaranteed to be the global minimum due to being a probabilistic method. Although the mutation process allows the GA to escape a local minimum to an extent, the GA may still converge to a local optimum instead of the globally optimal solution. The effectiveness of the GA heavily relies on the selection of appropriate genetic operators, population size, and convergence criteria. Careful parameter tuning and multiple runs may be necessary to increase the likelihood of finding satisfactory solutions.

The GA in this study was implemented using the Global Optimization Toolbox in MATLAB 2021a (MathWorks, MA, USA). The population size was 2000. A smaller population was not able to explore the search space enough to reach a reasonable

solution due to the complexity of four-bar linkage problem.

The selection method was Stochastic Universal Sampling (SUS), in which a line representing the population was created where each parent corresponds to a section of the line of length proportional to its fitness value. SUS then sample all solutions at evenly spaced intervals. This gives fitter individuals greater chance to be sampled, while also giving weaker members a chance to be chosen [116].

The crossover method was Crossover Scattered, where each element of the child's gene is selected randomly from a parent. To be more specific, first, a random binary vector with a length equal to the genes is created. The genes of the child is then created by selecting the first parent's genes where the random vector is 1, or selecting the second parent's genes where the random vector is 2 [117]. For instance, if p_1 and p_2 are the parents:

p_1 = [a b c d e f g h], and
p_2 = [1 2 3 4 5 6 7 8],

and the randomly generated binary vector is [1 0 0 0 1 1 0 0], the generated child is then

child = [a 2 3 4 e f 7 8].

Mutation was also adopted to enhance the GA's ability to explore the search space. The adopted mutation function was Gaussian mutation, where a random number taken from a Gaussian distribution with mean 0 was added to each genes of the parent. The amount of mutation decreases as the optimization process progresses. The standard deviation of the mutation parameter was given by the following recursive function

$$\sigma_k = \sigma_{k-1}\left(1 - \frac{k}{\text{Generations}}\right) \tag{4.10}$$

where σ_k represents the standard deviation at generation k.

The initial standard deviation value was 1 ($\sigma_1 = 1$). The percentage of crossover children and mutation children was 80% and 20%, respectively [116, 117].

Quasi-Newton Method

To further optimize the results obtained from GA, a quasi-Newton method was used to fine-tune the results obtained from GA. A similar approach have been adopted in [118], where they used gradient descend, another gradient-based method, to fine-tune the optimized results from GA. By using a gradient-based method for fine-tuning, the optimization process can converge faster within the basin of attraction, which allows the optimal solution to be found more efficiently.

The quasi-Newton methods are a class of optimization algorithm used to solve unconstrained optimization problems as an alternative to Newton-Raphson method. Unlike the Newton-Raphson method, the quasi-Newton method can be used even if the Jacobian or Hessian is not available, or is too expensive to compute. Instead, the quasi-Newton method iteratively updates an estimate of the Hessian matrix, which represents the second-order derivative of the objective function.

In the quasi-Newton method, the Hessian matrix is approximated using the information obtained from the gradient of the objective function and the history of the parameter updates. The algorithm starts with an initial estimate of the Hessian matrix and updates it at each iteration based on the changes in the gradient and the parameter values.

Various quasi-Newton algorithms have been proposed in the literature, including Broyden's method [119], the Broyden–Fletcher–Goldfarb–Shanno (BFGS) algorithm [120–123], Davidon–Fletcher–Powell (DFP) formula [124,125], and Symmetric Rank 1 (SR1) method [126]. In this study, the implementation of the BFGS algorithm in MATLAB 2021a was utilized.

Results

The best optimization results were manually examined for mechanical feasibility. The selected optimization solution of the medial and lateral sides are shown in Fig. 4.4 and Fig. 4.5, respectively. The path traced by point P replicates the path traced by the tibial plateau, and the origin point (0, 0) represents the GCA of the femoral condyle.

Next, the optimized mechanism was compared to a simple revolute joints and four-bar mechanisms proposed in the literature. The positions of all mechanisms were optimized, and the coupler link was extended with an optimal coupler point

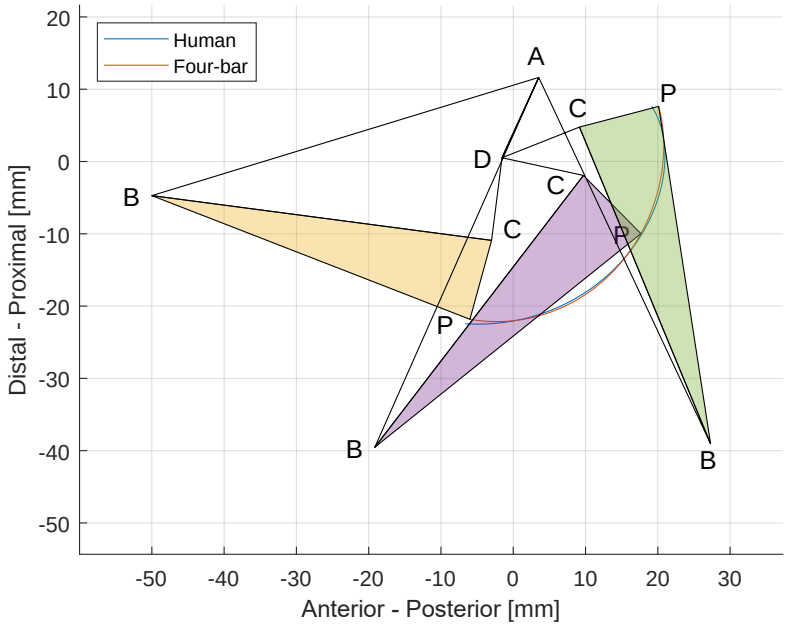

Figure 4.4: The optimal four-bar linkage configuration of the medial side at 0°, 60°, and 120°.

(point P in Fig. 4.3) to minimize the errors. All mechanisms were compared to the data in [43].

The four-bar mechanisms proposed by Zavatsky et al. [51] and Karami et al. [52] showed a significantly reduced error compared to a revolute joint on the lateral side, from 5.69 mm to 1.72 mm and 1.81 mm, respectively. However, The errors were much larger on the medial side, at 5.08 mm and 5.49 mm, respectively. This highlights the importance of using an asymmetric four-bar linkage, which has a much lower RMSE of 0.35 mm and 0.46 mm on the medial and lateral side, respectively. The errors are summarized in Table 4.1.

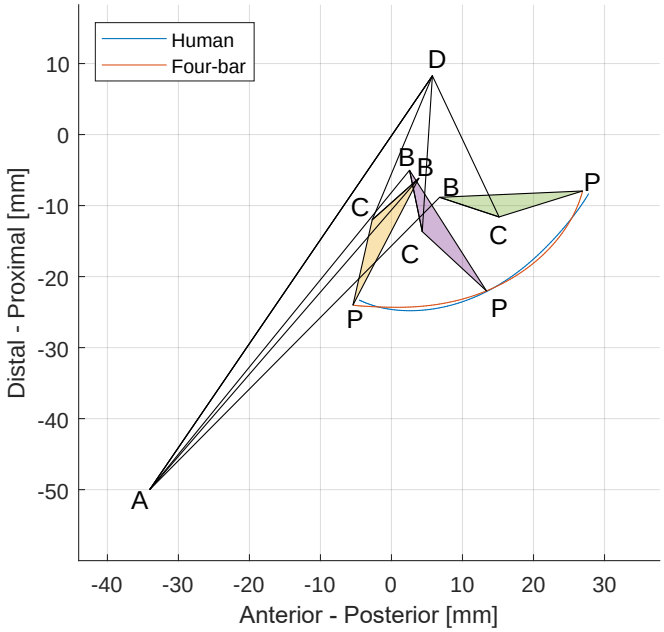

Figure 4.5: The optimal four-bar linkage configuration of the lateral side at 0°, 60°, and 120°.

Table 4.1: RMSE of knee joint mechanisms in the literature.

Mechanism	RMSE [mm]	
	Medial	Lateral
Revolute Joint	6.61	5.69
Zavatsky model [51]	5.49	1.72
Karami model [52]	5.08	1.81
Proposed dual four-bar	0.35	0.46

4.2 Device Design

In this section, the design process of determining the position of the HAM is discussed. The position of the HAM plays a crucial role in achieving effective pHRI, generating the required torque profile, and assisting the user in performing specific tasks. First, the SC action is examined to determine the required assistance for SC in older people. Next, the HAM and its placement to generate the optimum assistive torque is discussed.

4.2.1 Stair Climbing

The literature on kinematics of stair climbing has seen several studies conducted, but there is a notable variation in their results. The reported peak torque varies from as low as 0.58 $\mathrm{N\,m\,kg^{-1}}$ in [127] to as high as 1.72 $\mathrm{N\,m\,kg^{-1}}$ in [128]. The angle at which the peak torque occurred also varies between 40° to 70° [9, 10, 129–134]. The maximum reported mean of peak flexion angle was 106° [10].

One significant factor contributing to this variation is the age of participants involved in the studies. For instance, Hortobágyi at al. [9] and Böhme et al. [10] specifically examined the effects of participant demographics on stair climbing kinetics. The results revealed a significant difference in peak knee torque between old and young groups, highlighting the influence of participant characteristics on the observed kinetics. Other factors such as stair dimensions also impact the resulting knee torque during stair climbing. The peak knee torque values in the literature are summarized in Table 4.2.

Table 4.2: Peak of average stair climbing torque normalized to body weight in $\mathrm{N\,m\,kg^{-1}}$. Adapted from [135] and [10].

Researchers	Average	SD
Andriacchi et al. [129]	0.76	0.24
Andriacchi et al. [136]	0.69	0.29
McFadyen and Winter [130]	∼1.50	N/A
Markovich et al. [137]	1.46	0.25
Costigan et al. [138]	1.16	0.23
Kowalk et al. [139]	0.92	0.23
Salsich et al. [131]	1.11	0.14
Riener et al. [132]	∼1.1	N/A
Hortobágyi et al. (elderly) [9]	1.00	0.22
Hortobágyi et al. (young) [9]	1.55	0.24
Protopapadaki et al. [127]	0.58	0.19
Reid et al. [133]	0.96	0.13
Reeves et al. [134]	1.19	0.14
Larsen et al. [128]	1.72	0.49
Böhme et al. (elderly) [10]	0.9	0.3
Böhme et al. (young) [10]	1.7	0.3

4.2.2 Hydraulic Artificial Muscle

The HAM used in this chapter has a similar size and braiding angle to the HAM introduced in Chapter 2. However, it has a minor differences in construct and material, resulting in a different force-contraction relationship. The experimental contraction force is shown in Fig. 4.6. Other properties of the HAM are summarized in Table 4.3.

Similar to Chapter 2, the model of the HAM used during the design process was not the theoretical model of the HAM which greatly exaggerates the contraction ratio. Instead, a linear regression of the unloading force-contraction curve was used. The model was previously discussed in Section 2.2.3.

The HAM is connected to between link AD and BC to generate knee extension torque through the Angled Bar, BE. The placement of the HAM on both links was determined by first determining a fixed HAM length. First, link BC was extended

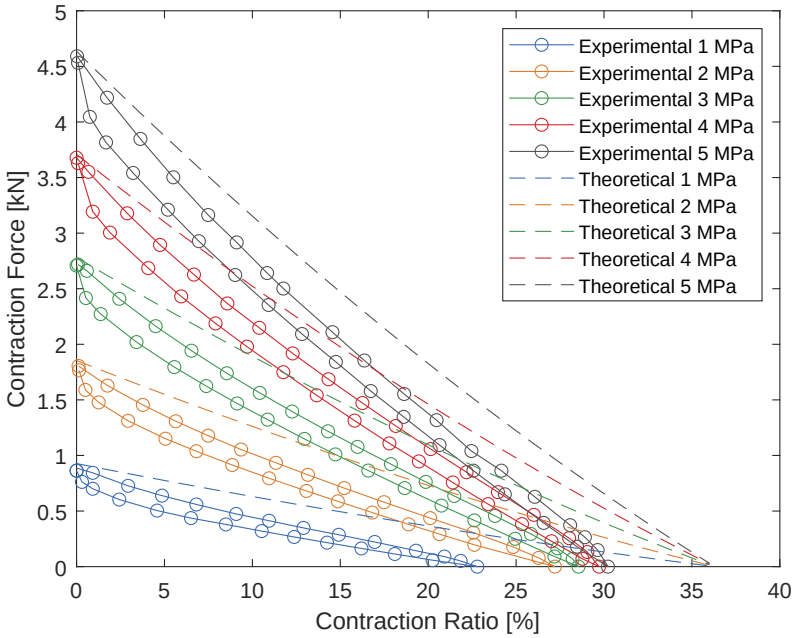

Figure 4.6: Experimental and theoretical of force-contraction relationship of the HAM used in this chapter.

Table 4.3: Properties of the HAM used in this chapter.

Parameter	Value
Hole-hole distance	250 mm
Contracting length	166 mm
Maximum pressure	5 MPa
Maximum contraction ratio	30.2%
Inner tubing diameter	8 mm
Outer tubing diameter	11 mm
Sleeve Diameter	12 mm
Sleeve material	Kevlar
Initial braiding angle	25°
Dry weight (including fittings)	100 g

from point B by length l_1 and angle ψ, creating point E, which is where the HAM is connected to link BC. Then, to match the contraction ratio of the HAM to the motion range of the device, a circle with a radius equal to the length of the HAM

at rest length was drawn with the point E at $\theta_{\text{knee}} = 0$ as its center. Next, another circle with a radius equal to the HAM at maximum contraction was drawn with the point E at maximum flexion angle as its center. The two circles has two intersection, and the intersection on the proximal side (i.e. on the thigh) is selected as the fixed point for the HAM. This process ensures that the HAM will be at rest length at the maximum flexion angle, and fully contracted when $\theta_{\text{knee}} = 0$, effectively preventing the device from bending the knee beyond its natural range of motion.

Next, the output knee extension torque of the device can be calculated using the position of both fixed points of the HAM and the ICR. The knee torque calculation methodology was discussed in detail in Section 2.2.2.

The optimal values of l_1 and ψ were selected by using grid search to optimize for the values with the maximum L^1 norm of knee extension torque between 40° to 70°, which is the range where the peak torque during SC was reported in the literature. The values were also selected such that the device will not generate negative torque, hindering the motion at any knee joint position. The lateral link was designed with a slightly wider range of motion to account for internal rotation.

The final design of the device with the four-bar linkage mechanism the fully extended position with the HAM in a fully contracted state are presented in Fig. 4.7.

The theoretical peak torque of the proposed device 152.44 N m which occurs at 57°. This is equivalent to 2.09 N m kg^{-1} normalized to body parameters in [107,108]. This is greater than the 1.72 N m kg^{-1} reported by Larsen et al. [128], which is the highest value found in the literature. The torque output of the device on both sides and the total torque are presented in Fig. 4.8.

The final design of the device is displayed in Fig. 4.9.

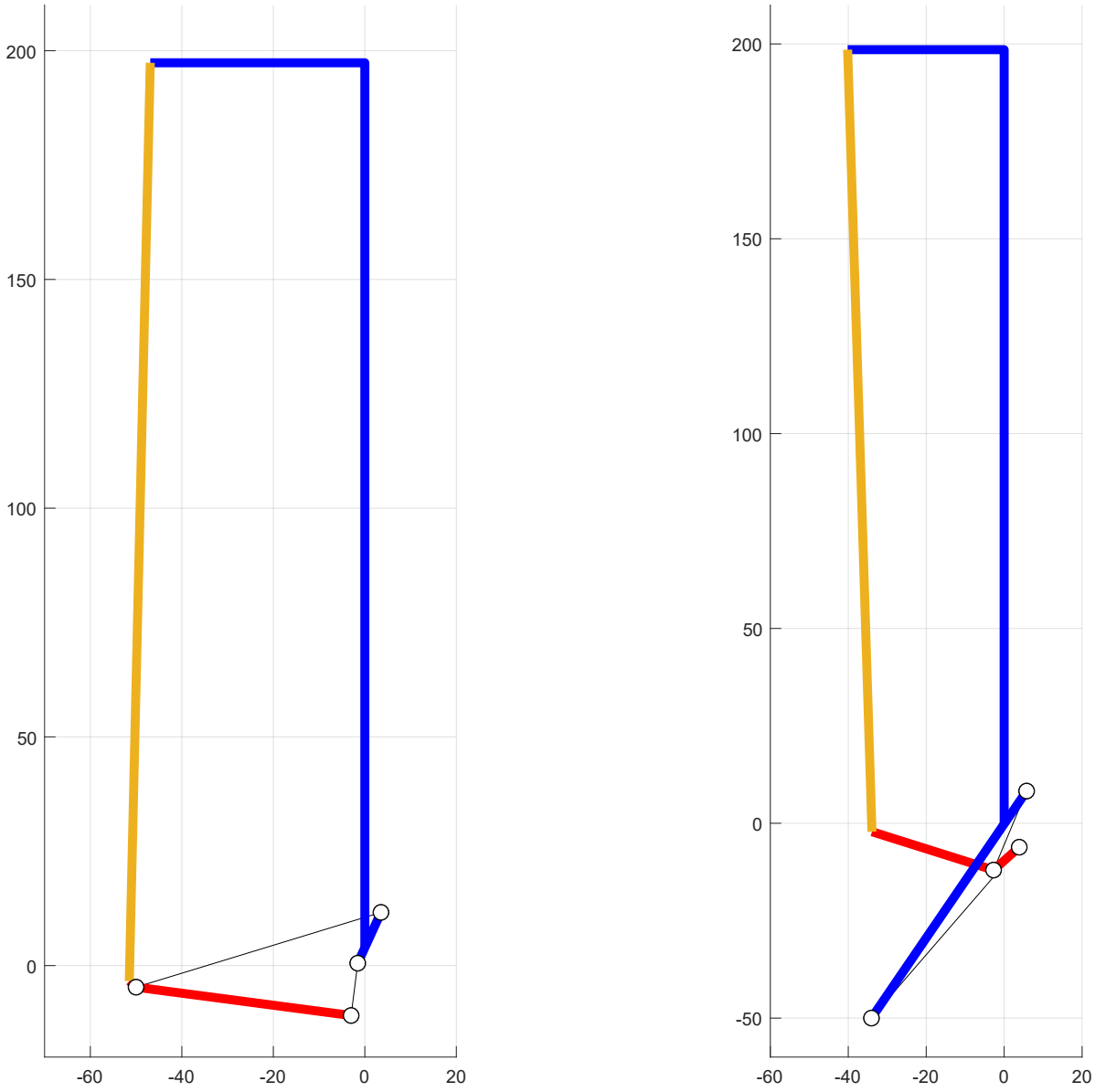

(a) Medial (b) Lateral

Figure 4.7: Diagram of the dual four-bar linkage mechanisms on the (a) medial and (b) lateral sides. The thigh part, shank part, and the HAM are shown in blue, red, and yellow, respectively.

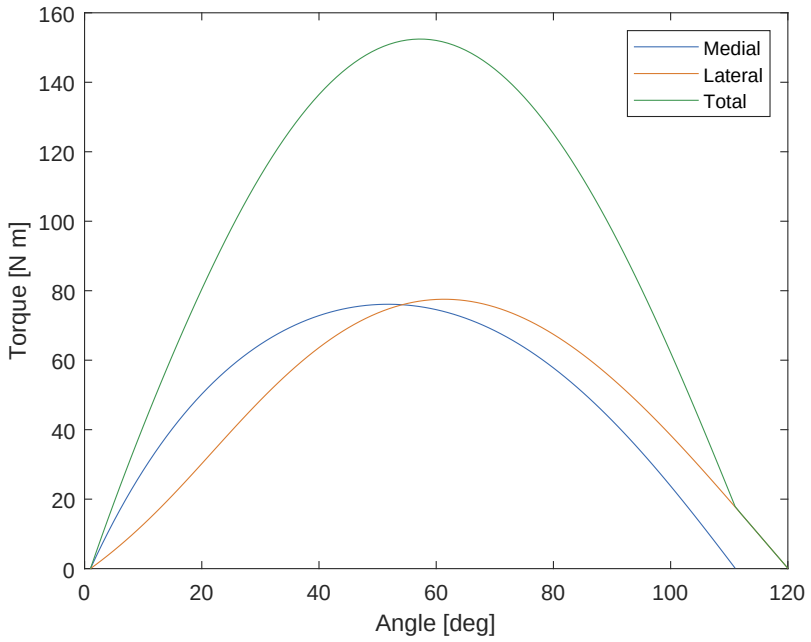

Figure 4.8: Theoretical output torque of the proposed device.

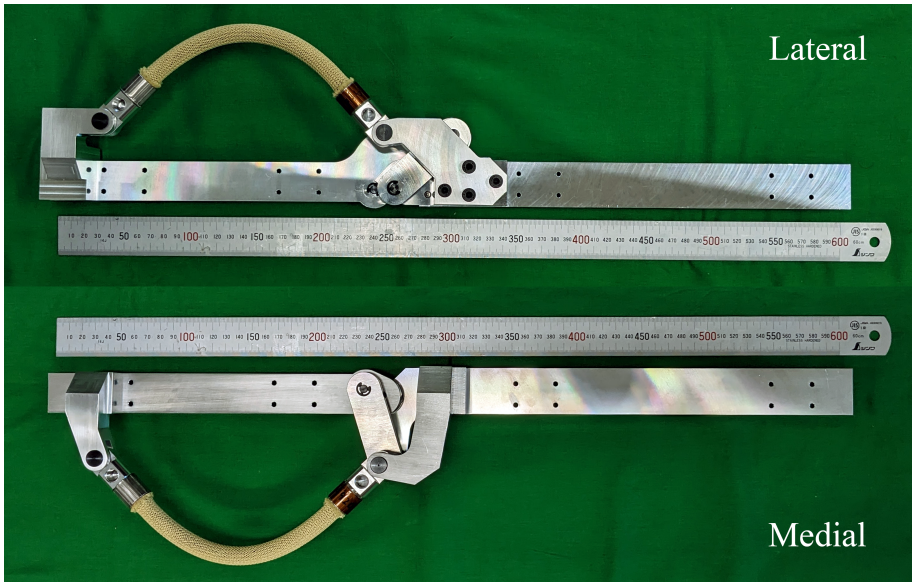

Figure 4.9: Photograph of the proposed device for the right leg on the lateral and medial sides.

4.3 Experiments

Three experiments were conducted to verify the effectiveness of the proposed exoskeleton. First, the improved comfort of the proposed dual four-bar linkage mechanism were evaluated using pressure sensor to measure the unintended load acting on the leg due to human-robot misalignment. Next, the torque output of the device was measured to confirm the performance of the device. Finally, a human trial have been conducted to verify the effectiveness of the device in human. The experiments in this chapter uses the servo pump discussed in Chapter 3 as the pressure source.

4.3.1 Undesired Load Measurement

When a wearable device with an incompatible kinematics to the natural biomechanics of the human body is worn, it can lead to issues of overconstraint and discomfort for the user. This is particularly evident in the joints, where the additional constraints imposed by the device can limit the natural range of motion and create a sense of discomfort. The discomfort can vary depending on the type of connective equipment used, such as braces, cuffs, or straps.

In cases where the connective equipment is deformable or not tightly fixed to the user, the relative movement between the human body and the wearable device can result in friction and abrasion, leading to further discomfort and potential skin irritation. Furthermore, a wearable device that does not fit well to the user's body may fail to effectively deliver the intended assistive forces or torques [28].

Conversely, if the wearable device is tightly fixed to the user's body using stiff supports to ensure better force and torque delivery, there is a risk of undesired load acting on the user's biological joints due to misalignment. This may potentially cause discomfort and even injury in extreme cases.

As the device is designed to provide power assistance, the device was tightly fixed to the body with stiff braces to ensure better force transmission. Therefore, the primary source of discomfort in this device is the unintended load on as the normal force between the limb and the connecting equipment. The shearing force in the proximal-distal direction is difficult to measure due to the deformability of human tissue and skin. Therefore, only the normal force acting perpendicular to the limb will be measured.

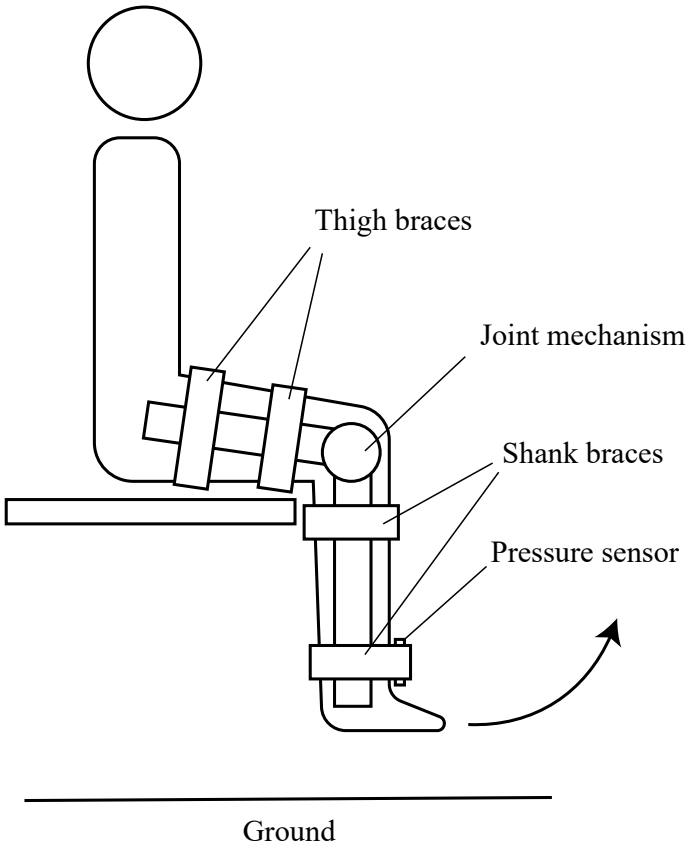

Figure 4.10: Diagram of the undesired load experiment.

Methodology

In this experiment, stiff braces were used to connect the wearable device to the user's body. These braces were carefully designed and 3D-printed to fit the user's body contours, ensuring a secure and customized attachment. The braces were fixed to the user's body using hook-and-loop fastener straps. Two braces were used for each of the shank and thigh parts of the device, resulting in a total of four braces.

To measure the undesired load, a thin film force sensing resistor (MD30-60, Walfront) was inserted between the lower shank brace and the user's leg. This position is where the undesired load was felt the intensely in preliminary tests. Both sides of the sensor were attached with a thin plate to normalize the contact surface. The sensor was calibrated to ensure a precise sensor readings. The experiment setup is illustrated in Fig. 4.10.

The proposed dual four-bar linkage mechanism was compared against an identical orthosis with a revolute joint and a four-bar linkage proposed by Karami et al. [52],

which was used in Chapter 2. All mechanisms were outfitted with identical braces. The experiment was conducted on a 28-year-old healthy male with a height of 1.65 m and body mass of 54 kg. The experimental methodology is as follows:

1. The participant wears the device while seated and the knee at approximately 90° angle.
2. The participant extends and flexes their leg a few times and readjust the straps to align the device with the biological joint.
3. The participant is seated with their legs hanging.
4. The participant slowly extends their leg until fully extended, then slowly returns to the hanged position. This step is repeated for 10 times.

Results

The experimental results show a significant reduction in undesired force acting on the shank part as shown in Table 4.4. Moreover, the participant reports a significantly reduced pain at the contact area at the braces.

Table 4.4: The mean and standard deviation of peak load acting on the lower shank brace during extension motion in N.

Mechanism	Medial	Lateral
Revolute	14.15 (2.32)	18.32 (2.61)
Karami Model [52]	10.70 (1.95)	6.48 (1.22)
Proposed Dual Four-bar	1.88 (0.26)	1.07 (0.17)

The experiment results show that in orthoses with traditional revolute joint, kinematic differences between a mechanical joint and a biological joint may causes discomfort and pain. On the other hand, the proposed four-bar linkage mechanism which aims to mimic the biomechanics of human knee joint can significantly improve comfort by reducing load at connective equipment.

4.3.2 Torque Output Measurement

In this experiment, the output torque of the device was measured to verify the performance of the proposed design.

Methodology

The proposed device was clamped vertically at the thigh part with C-clamps to fix the thigh part's alignment horizontally. Next, hydraulic pressure was applied to the HAM, which caused the HAM to contract and put the shank part at full extension or $\theta_{\text{knee}} = 0°$. Force was then applied at the end of the shank part by pressing a force gauge by hand until it reached the maximum flexion angle. Next, the applied force was reduced until the shank part extended to measure the unloading curve.

The output torque was calculated by multiplying applied force to distance to ICR. The applied force was measured using a force gauge (FGPX-100, NIDEC DRIVE TECHNOLOGY CORPORATION, Kyoto, Japan). The hydraulic pressure was generated from the equipment described in Chapter 3 operating directly with no switching involved.

Results

The experiment was only conducted at 2 and 3 MPa pressure. At higher pressure levels, the bending moment due to the vertical offset between the linkage mechanism and the HAM which was not considered during the design stage caused the pins at the joints to bend. Therefore, we only experimented up to 3 MPa to avoid damaging the device.

Even at a lower pressure, the device displayed deformation, resulting in increased friction between parts. This also contributes to hysteresis characteristics of the device, resulting in the discrepancies between the loading and unloading curves. The experiment results of the medial and lateral links are shown in Fig. 4.11 and Fig. 4.12, respectively.

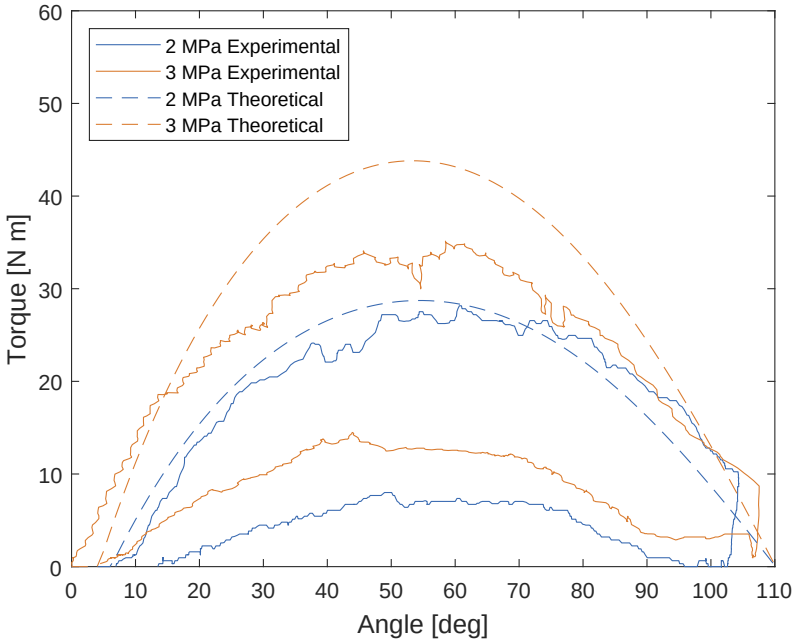

Figure 4.11: Torque output of the medial side of the proposed device.

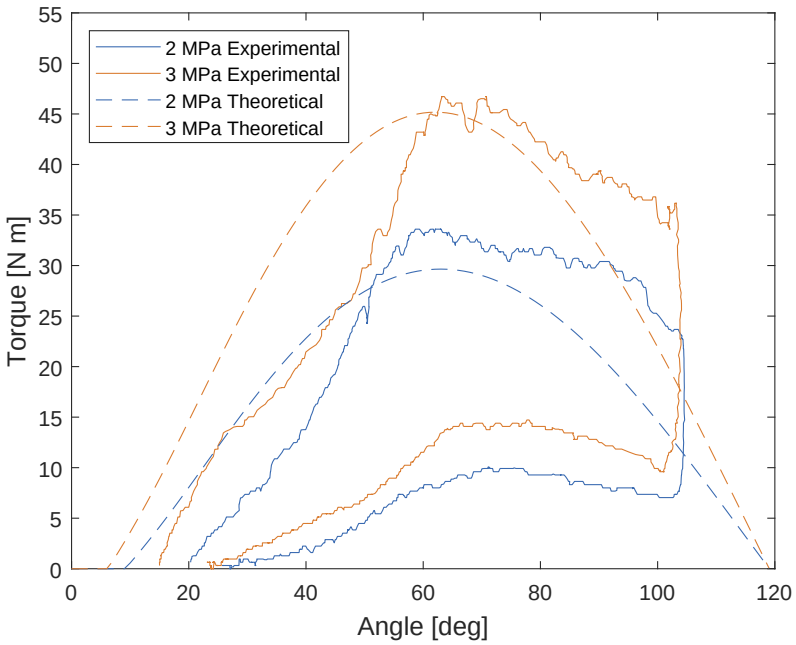

Figure 4.12: Torque output of the lateral side of the proposed device.

4.3.3 Support Evaluation

In this section, a human trial was conducted to evaluate the effectiveness of the proposed device in assisting a natural SC motion in a healthy subject. The EMG signal was monitored to measure the level of muscle activation during SC with and without assistance from the device.

Methodology

The stair used in this study had two steps, with a 160 mm rise and 265 mm run. The participant was a 28-year-old healthy male with 1.65 m body height and 54 kg body mass. The device was equipped with 3D-printed braces and slots, a rubber strap, and hook-and-loop fastener straps as shown in Fig. 4.13. The weight of the device including connective equipment was 3.7 kg. The subject wore the device on the left leg. First, the participant placed their left foot on the first step in a natural position. Next, the participant climbs the stair, lifting their right foot from the ground to the second step. The experiment methodology is illustrated in Fig. 4.14. The EMG signal was measured during the stance phase of the supported leg.

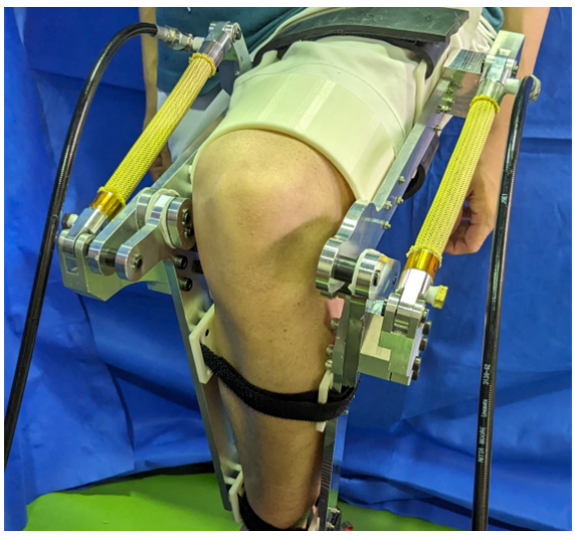

Figure 4.13: The proposed device worn by the participant.

A natural EMG signal during SC without wearing the device was compared with two support strategies. In the slow assistance configuration, the pump flow rate was limited to 0.58 cm^3/sec, resulting in a gradual increase in actuator pressure. The supply pressure increased gradually similar to a ramp function until reaching the

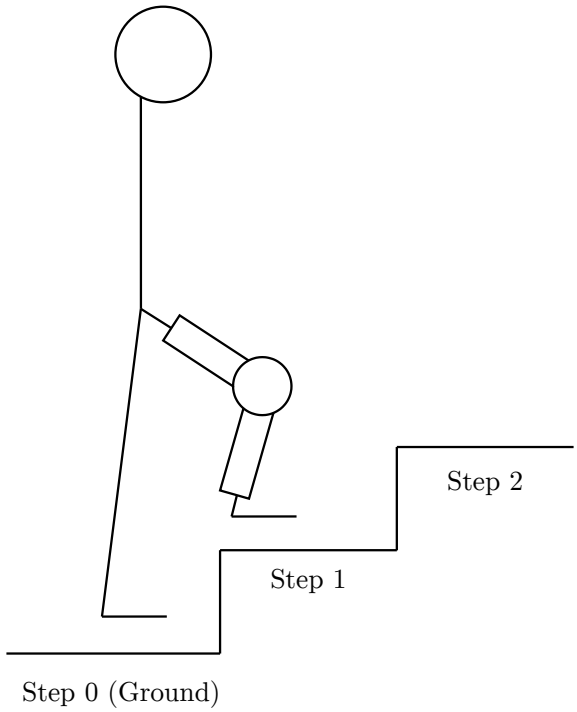

Figure 4.14: Illustration of the experiment methodology.

maximum pressure of 3 MPa in approximately 2 second. On the other hand, in the fast assistance configuration, flow rate limit was increased to 2.33 cm^3/sec. The supply pressure increased to the maximum value in a much smaller. The applied pressure in each assistance schemes are illustrated in Fig. 4.15. The subject performed ten trials of the experiment for each configuration.

Hydraulic pressure was supplied and controlled the hydraulic equipment described in Chapter 3. The EMG signal on the left Rectus femoris was measured using a surface electromyography device (FREEEMG 1000, BTS Bioengineering, MI, Italy). The signal was sampled at 1 kHz, and processed with a sliding window root mean square of 200 samples windows length. The signals were resampled and normalized to the STS duration, then the averages between the ten trials were calculated.

Results

The processed EMG signal showed a substantial reduction in muscle activity with the assist of the device as shown in Fig. 4.16. However, their is no significant differences between the two assistance strategies. The maximum processed EMG

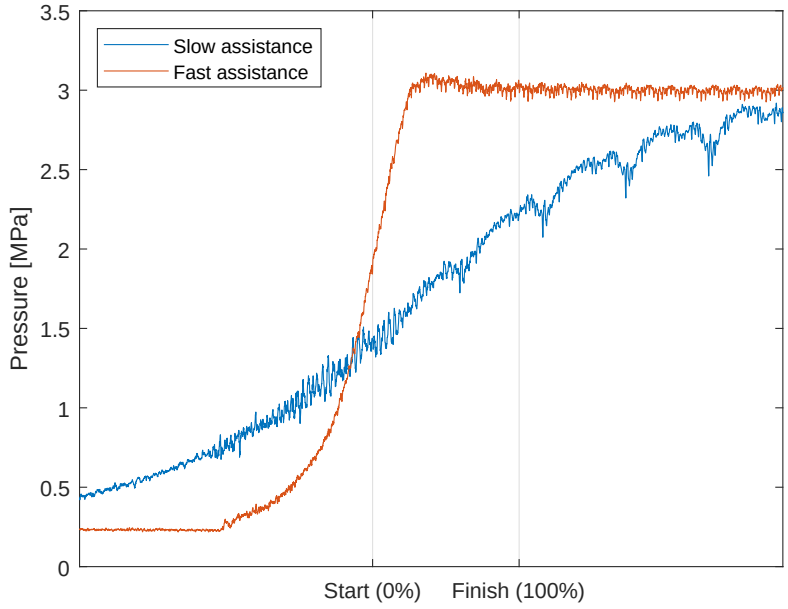

Figure 4.15: Slow assistance and fast assistance schemes.

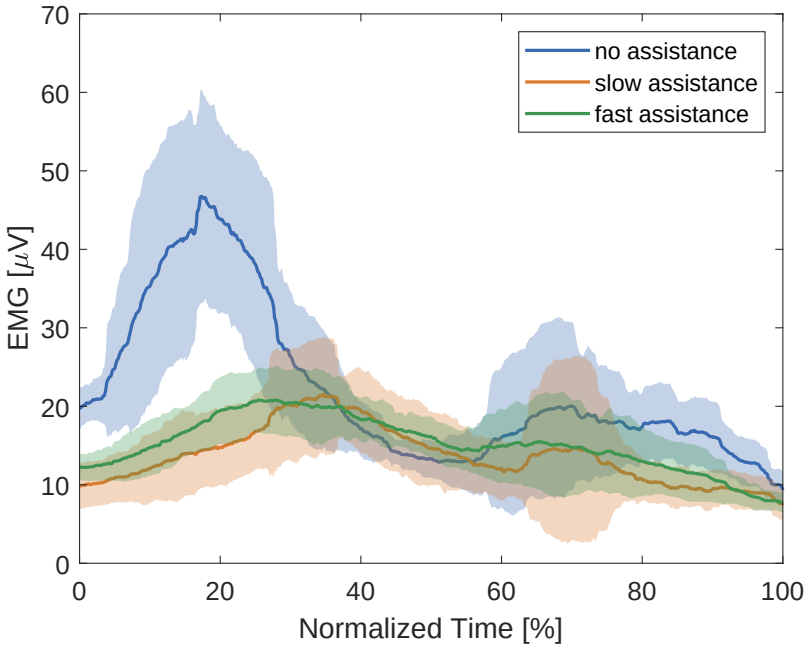

Figure 4.16: EMG signal on the Rectus femoris of the subject during SC.

signal without assistance, with slow assistance, and with fast assistance schemes were 52.34 µV, 26.09 µV, and 23.06 µV, respectively.

4.4 Discussion

The device was originally designed to have excessive maximum torque output. While this may seem counter-intuitive to the goal of developing an exoskeleton with reduced weight and inertia, the higher capability would allow us to study the effectiveness of the device at varying degree of support. The level of support provided can be easily adjusted by reducing the hydraulic pressure, which will reduce the torque output of the device. This allows for the investigation of different support levels and their impact on user performance, which is a crucial consideration to develop a more compact design in future iterations.

However, in the real device, the offset between the HAM and the four-bar linkage created a tremendous bending moment, resulting in bending of the pin at higher pressure levels. This limits the operating pressure of the device up to 3 MPa instead of 5 MPa in the design. Moreover, the increased friction due to deformations further reduced the torque output on the unloading curve, resulting in a large differences between loading and unloading curve. This is due to mechanical design limitations of the obtained optimized four-bar linkage parameters. Including additional mechanical design considerations into the optimization process will allow a more realizable configurations to be obtained.

The device including braces and straps weighed 3.7 kg and has a peak theoretical torque of 152.44 N m, which would result in a 41.2 $\mathrm{N\,m\,kg^{-1}}$ peak-torque-per-weight ratio at 5 MPa. This is lower than the STS exoskeleton proposed in Chapter 2, but still among the highest in Table 1.1 excluding Bowden cable devices. The reduced peak-torque-per-weight ratio was due to the fact that at rest length where the HAM has the maximum contraction force, the optimal mechanism has zero torque. This significantly reduced the theoretical peak-torque-per-weight ratio. Furthermore, the reduced torque output due to unconsidered bending moment resulted in a much lower operating pressure and torque output, with a combined torque of 22.4 N m. This corresponds to a 6.05 theoretical peak-torque-per-weight ratio, which is lower than all studies in Table 1.1.

Moreover, the proposed device has a low torque output at high knee joint angles, limiting its capability to assist some ADLs such as STS. However, with future design improvements, it is possible to address this limitation and enhance the device's performance to aid a broader range of ADLs, including STS.

Previous studies on powered knee exoskeleton for stair climbing assistance often aimed at 50% assistance ratio [140, 141]. However, the authors did not specify why they chose this number. A study on an optimal assistance ratio will be a valuable data for future studies.

Two assisting strategies, namely slow assistance, which gradually increases the assistive torque, and fast assistance, which instantaneously applies the assistive torque, were examined. No significant difference in the EMG signal was found between both configurations. A more gentle application of assistive force gives the user more time to adjust and stabilize their motion. This finding may serve as another consideration for the mechanical design and hydraulic systems in future iterations.

The trade-off between size and output torque is an important consideration for future iterations of the device. The intentional oversized design serves as a starting point to explore the device's capabilities and understand the effects of different torque levels on user assistance. Future iterations of the device optimized for lower degree of support will require less torque, which will allow a more compact link mechanism, as well as smaller pumps to be utilized. The findings from the study on varying degrees of support will inform the decision-making process and guide the design choices in creating more compact and efficient devices in the future, taking into account factors such as mobility, ease of use, and overall user experience.

In Section 4.3.3, the proposed device was only worn on one leg and actuated simultaneously with a common hydraulic supply unit, and did not take full advantage of the switching algorithm for multi-DoF hydraulic system proposed in Chapter 3. Wearing the device on both lower limbs will allow the proposed device to take full advantage of the MEHA system, and also fully support the SC motion which requires both limbs.

4.5 Chapter Summary

In this chapter, an exoskeleton designed specifically for SC assistance was introduced. The exoskeleton utilized a dual four-bar linkage mechanism, which was chosen to provide a higher torque output necessary for stair climbing.

The design of the dual four-bar linkage mechanism took into account the asymmetry of the medial and lateral sides of the condyle, ensuring a more anatomically accurate motion. The kinematics of the mechanism were optimized using a genetic

algorithm, aiming to replicate the translational motion of the knee joint at any orientation. This optimization process helped achieve a more natural and effective movement pattern.

The actuator of the exoskeleton was implemented using a HAM, positioned strategically to maximize torque output within the range of 40°-70°, which is known to be the angle where the knee joint generates the highest torque according to previous literature.

To evaluate the effectiveness of the proposed design, three experiments were conducted. Firstly, the human-robot misalignment, which can lead to user discomfort, was measured using a pressure sensor to quantify the undesired load acting on the leg. The results demonstrated a significant improvement from 14.15 N and 18.32 N in revolute joint on the medial and lateral sides, respectively, to 1.88 N and 1.07 N in the proposed mechanism. This indicates a better alignment and reduced discomfort.

Secondly, the torque output of the exoskeleton was measured to assess its capability to provide the necessary assistance during stair climbing. This evaluation aimed to validate the design's ability to deliver the required torque effectively.

Lastly, a human trial was conducted to evaluate the supportive capabilities of the exoskeleton. EMG signals were used to measure muscle activity, and the results showed a significant reduction in muscle activity when the device provided assistance from 52.34 µV to 23.06 µV. This reduction in muscle activity indicated that the exoskeleton effectively offloaded the user's muscles, reducing the effort required during stair climbing.

Overall, the experiments conducted in this chapter demonstrated the effectiveness of the proposed dual four-bar linkage exoskeleton design for stair climbing assistance. The design addressed the issue of human-robot misalignment, and successfully reduced muscle activity during stair climbing, indicating its potential as an assistive device for this specific task.

Chapter 5

Conclusions

In this thesis, a hydraulic-powered ergonomic knee exoskeleton for the elderly was studied in various aspects, including the biomechanics of the knee joint, the mechanics of the HAM and four-bar linkage, as well as the hydraulic system required to operate the HAM.

Chapter 1 introduces the hazard risks associated with ADLs in the elderly, with falls being the leading external cause of death in this population. STS and SC were identified as some of the most difficult and risky ADLs due to deteriorated physical capabilities. However, these falls can be prevented with the use of assistive devices, which can be categorized as manual devices, powered devices, and exoskeletons. While manual and powered assistive devices are often immobile, limiting their utility, robotic exoskeletons are mobile and can be used in various applications, making them advantageous for the user. However, current exoskeletons are plagued by discomfort caused by human-robot misalignment and excessive inertia. Therefore, the objective of this thesis is to develop an ergonomic exoskeleton with reduced misalignment and inertia.

Chapter 2 introduces a bioinspired knee support device that utilizes a four-bar joint mechanism and HAM to reduce misalignment and weight compared to previous exoskeletons. A previously proposed four-bar linkage joint was modified to accommodate the HAM. Additionally, the Angled Bar was proposed to exploit the force-contraction relationship of the HAM to generate the desired torque at the corresponding angle by applying constant hydraulic pressure without the need for a complex control system. The device was able to generate a maximum output of 126.55 Nm torque at a knee joint angle of 100° during loading and 70.69 Nm

torque at 100° during unloading at a pressure of 3 MPa, resulting in a 78.56 Nm/kg peak-torque-per-weight ratio, which is much higher than previous exoskeletons in the literature. The root-mean-square error of the knee extension torque curve was 13.01 N m. An experiment with a healthy participant showed a significant reduction in muscle activity with the assistance of the device. The maximum processed EMG signal with and without assistance were 52.10 µV and 20.93 µV, respectively.

Chapter 3 aimed to simplify the hydraulic components of a centralized multi-degree-of-freedom hydraulic system for hydraulic exoskeletons by adopting on-off valves and synchronizing them with a servo pump. To achieve individual actuator pressure control, two control algorithms were proposed: MEHA and APCS. In the MEHA approach, the servo pump switches between the reference signals of each actuator by periodically opening or closing the valves. On the other hand, the APCS system utilizes a servo pump that supplies a periodic source pressure, such as a triangular wave, and the valves operate by comparing the source pressure with the reference signal. Furthermore, two algorithms for position control were introduced: the periodic switching mode and the hysteresis switching mode. In the periodic switching mode, the controller cyclically switches between the actuators, while in the hysteresis switching mode, the controller triggers a switch if the estimated volume exceeds the error band by a specific threshold. The experimental results demonstrated successful control of both the pressure and volume of all actuators using the proposed algorithms in the multi-degree-of-freedom hydraulic system.

Finally, Chapter 4 discussed the design and evaluation of a multi-DoF exoskeleton specifically created to assist with SC powered by the hydraulic system introduced in Chapter 3. The exoskeleton utilizes a dual four-bar linkage mechanism to allow for the large torque necessary for SC, which is greater than for STS. The design takes into account the asymmetry of the knee joint to ensure more anatomically accurate motion and optimizes the kinematics using GA. The actuator of the exoskeleton employs a HAM positioned strategically to maximize torque output required for stair climbing. Three experiments were conducted to assess the effectiveness of the design. The first experiment measured human-robot misalignment and demonstrated significant improvement compared to previous mechanisms. The undesired normal force due to misalignment reduced significantly from 14.15 N and 18.32 N in revolute joint on the medial and lateral sides, respectively, to 1.88 N and 1.07 N in

the proposed mechanism. The second experiment measured the torque output of the exoskeleton to evaluate its capability to assist during stair climbing. The third experiment involved a human trial where muscle activity was measured using EMG signals, showing a significant reduction in muscle activity from 52.34 µV to 23.06 µV when the exoskeleton provided assistance.

Comparing the proposed devices to those in the literature, the proposed exoskeleton, especially the STS variant, is among the lightest and boasts the highest peak-torque-per-weight ratio, excluding Bowden cable devices, as shown in Table 1.1. Furthermore, the proposed device offers improved comfort due to the kinematically compatible four-bar joint mechanisms, in contrast to the commonly used revolute joint mechanisms found in the literature.

Future work includes the improvement of the mechanical design of the mechanism and support equipment. The mechanical components of the exoskeleton could undergo further analysis and redesign to enhance their efficiency, durability, and comfort. The vertical offset issue encountered in the SC exoskeleton should be addressed in future designs. Another area of improvement lies in the hydraulic equipment. While the experimental pump and valves used in this study confirmed the effectiveness of the proposed control schemes, actual hydraulic application necessitates further reduction in physical footprint and weight. Lastly, conducting a human trial specifically with elderly participants would be essential to validate the exoskeleton's effectiveness for its intended use case.

Further directions for this work involve adopting pressure control for each actuator, enabling the torque output of the device to be adjusted for any ADLs beyond STS or SC. Another potential enhancement is the expansion of covered joints, such as the hip or ankle, which would enable the proposed exoskeleton to comprehensively support lower extremities in various ADLs.

Table 5.1: Weight and peak torque of the proposed devices compared to recent knee exoskeletons.

Study	Transmission	Actuator	Peak torque [N m]	Weight [kg]	Torque/Weight [N m kg^{-1}]
KNEXO [63]	Pneumatic	Pleated PAM	75	4.5	16.67
AssistOn-Knee [57]	Bowden cable	External motor	780	1.4	557.14
Kim et al. [54]	Electrical	Motor (with battery)	38	3.5	10.86
Witte et al. [64]	Bowden cable	External motor	120	0.76	157.89
Wang et al. [59]	Electrical	Motor	16	1.82	8.79
Sarkisian et al. [60]	Electrical	Motor	120	2.5	48
Lee et al. [65]	Electrical	Motor	17.4	1.5	11.6
Rituraj et al. [66]	Hydraulic	Cylinder	100	2.8	35.71
STS Exoskeleton	**Hydraulic**	**HAM**	**Design: 68.84**	**0.9**	**76.49**
			Experimental: 70.7		**78.56**
SC Exoskeleton	**Hydraulic**	**HAM**	**Design: 152.44**	**3.7**	**41.2**
			Experimental: 22.4		**6.05**

Bibliography

[1] Canadian Institute for Health Information, "National Trauma Registry 2011 Report: Hospitalizations for Major Injury in Canada, 2008–2009 Data," *Ottawa, Ont.: CIHI*, 2011.

[2] J. K. Startzell, D. A. Owens, L. M. Mulfinger, and P. R. Cavanagh, "Stair negotiation in older people: a review," *Journal of the American Geriatrics Society*, vol. 48, no. 5, pp. 567–580, 2000.

[3] P. Haentjens, J. Magaziner, C. S. Colón-Emeric, D. Vanderschueren, K. Milisen, B. Velkeniers, and S. Boonen, "Meta-analysis: excess mortality after hip fracture among older women and men," *Annals of internal medicine*, vol. 152, no. 6, pp. 380–390, Mar. 2010.

[4] R. S. Braithwaite, N. F. Col, and J. B. Wong, "Estimating hip fracture morbidity, mortality and costs," *Journal of the American Geriatrics Society*, vol. 51, no. 3, pp. 364–370, Mar. 2003.

[5] J. Verghese, C. Wang, X. Xue, and R. Holtzer, "Self-reported difficulty in climbing up or down stairs in nondisabled elderly," *Archives of physical medicine and rehabilitation*, vol. 89, no. 1, pp. 100–104, 2008.

[6] J. Jensen, L. Lundin-Olsson, L. Nyberg, and Y. Gustafson, "Falls among frail older people in residential care," *Scandinavian Journal of Public Health*, vol. 30, no. 1, pp. 54–61, Jan. 2002.

[7] K. Rapp, C. Becker, I. D. Cameron, H.-H. König, and G. Büchele, "Epidemiology of Falls in Residential Aged Care: Analysis of More Than 70,000 Falls From Residents of Bavarian Nursing Homes," *Journal of the*

American Medical Directors Association, vol. 13, no. 2, pp. 187.e1–187.e6, Feb. 2012.

[8] T. Al-Aama, "Falls in the elderly: spectrum and prevention," *Canadian Family Physician*, vol. 57, no. 7, pp. 771–776, 2011.

[9] T. Hortobágyi, C. Mizelle, S. Beam, and P. DeVita, "Old adults perform activities of daily living near their maximal capabilities," *The Journals of Gerontology Series A: Biological Sciences and Medical Sciences*, vol. 58, no. 5, pp. M453–M460, 2003.

[10] M. Böhme, F. Weiske, J. Jäkel, J. Zentner, and M. Witt, "Evaluation of the power deficit of elderly people during stair negotiation: Which joints should be assisted at least by an exoskeleton and with what amount?" *Wearable Technologies*, vol. 3, p. e4, 2022.

[11] T. Kotake, N. Dohi, T. Kajiwara, N. Sumi, Y. Koyama, and T. Miura, "An analysis of sit-to-stand movements," *Archives of Physical Medicine and Rehabilitation*, vol. 74, no. 10, pp. 1095–1099, 1993.

[12] S. Yoshioka, A. Nagano, R. Himeno, and S. Fukashiro, "Computation of the kinematics and the minimum peak joint moments of sit-to-stand movements," *BioMedical Engineering OnLine*, vol. 6, no. 1, p. 26, July 2007.

[13] M. A. Hughes, B. S. Myers, and M. L. Schenkman, "The role of strength in rising from a chair in the functionally impaired elderly," *Journal of Biomechanics*, vol. 29, no. 12, pp. 1509–1513, 1996.

[14] M. Schenkman, M. A. Hughes, G. Samsa, and S. Studenski, "The Relative Importance of Strength and Balance in Chair Rise by Functionally Impaired Older Individuals," *Journal of the American Geriatrics Society*, vol. 44, no. 12, pp. 1441–1446, Dec. 1996.

[15] "Assistep – Stair Climbing Aid For Elderly," [Online; accessed 12. May 2023]. [Online]. Available: https://assistep.com/stair-climbing-aid-for-elderly

[16] R. Hanaoka and T. Murakami, "A novel assist device for tension pole based movable handrail," in *IECON 2015-41st Annual Conference of the IEEE Industrial Electronics Society*. IEEE, 2015, pp. 002 235–002 240.

[17] "Molift Quick Raiser 2 - Etac.com." [Online]. Available: https://www.etac.com/products/hoists-and-slings/sit-to-stand-solutions/molift-quick-raiser-2/

[18] "Hug T1." [Online]. Available: https://www.fuji.co.jp/en/items/hug/hugt1

[19] "Ernestine Power Lift Recliner - Ashley Furniture HomeStore." [Online]. Available: https://www.ashleyfurniture.com/p/ernestine-power-lift-recliner/9760112.html

[20] S. Ruszala and I. Musa, "An evaluation of equipment to assist patient sit-to-stand activities in physiotherapy," *Physiotherapy*, vol. 91, no. 1, pp. 35–41, Mar. 2005.

[21] "Bruno Elan Straight Stair Lift," Oct. 2019, [Online; accessed 26. Apr. 2023]. [Online]. Available: https://www.bruno.com/stair-lifts/elan-straight-indoor-stair-lift

[22] "HAL FOR MEDICAL USE (LOWER LIMB TYPE) - CYBERDYNE." [Online]. Available: https://www.cyberdyne.jp/english/products/LowerLimb%5Fmedical.html

[23] "ReWalk™ Personal 6.0 - ReWalk – More Than Walking." [Online]. Available: https://rewalk.com/rewalk-personal-3/

[24] "Exoskeleton for Stroke Recovery Gait Training - Ekso Bionics." [Online]. Available: https://eksobionics.com/eksohealth/eksonr/patients/

[25] "Rex Bionics - Reimagining Rehabilitation," Jan. 2020, [Online; accessed 26. Apr. 2023]. [Online]. Available: https://www.rexbionics.com

[26] M. K. Shepherd and E. J. Rouse, "Design and Validation of a Torque-Controllable Knee Exoskeleton for Sit-to-Stand Assistance," *IEEE/ASME Transactions on Mechatronics*, vol. 22, no. 4, pp. 1695–1704, Aug. 2017.

[27] H. Woo, K. Kong, and D.-w. Rha, "Lower-limb-assisting robotic exoskeleton reduces energy consumption in healthy young persons during stair climbing," *Applied Bionics and Biomechanics*, vol. 2021, 2021.

[28] J. L. Pons, *Wearable robots : biomechatronic exoskeletons.* John Wiley & Sons, 2008.

[29] Y. Akiyama, Y. Yamada, K. Ito, S. Oda, S. Okamoto, and S. Hara, "Test method for contact safety assessment of a wearable robot-analysis of load caused by a misalignment of the knee joint," in *2012 IEEE RO-MAN: The 21st IEEE International Symposium on Robot and Human Interactive Communication*. IEEE, 2012, pp. 539–544.

[30] L. Zhang, G. Liu, B. Han, Z. Wang, H. Li, and Y. Jiao, "Assistive devices of human knee joint: A review," *Robotics and Autonomous Systems*, vol. 125, p. 103394, 2020.

[31] É. Séguin and M. Doumit, "Review and assessment of walking assist exoskeleton knee joints," in *2020 IEEE International Conference on Systems, Man, and Cybernetics (SMC)*. IEEE, 2020, pp. 1230–1235.

[32] M. Gao, Z. Wang, S. Li, J. Li, Z. Pang, S. Liu, and Z. Duan, "Design and optimization of exoskeleton structure of lower limb knee joint based on cross four-bar linkage," *AIP Advances*, vol. 11, no. 6, p. 065124, 2021.

[33] A. Asker, S. Xie, and A. A. Dehghani-Sanij, "Multi-objective optimization of force transmission quality and joint misalignment of a 5-bar knee exoskeleton," in *2021 IEEE/ASME International Conference on Advanced Intelligent Mechatronics (AIM)*. IEEE, 2021, pp. 122–127.

[34] K.-M. Lee and J. Guo, "Kinematic and dynamic analysis of an anatomically based knee joint," *Journal of biomechanics*, vol. 43, no. 7, pp. 1231–1236, 2010.

[35] J. Bessler-Etten, L. Schaake, G. B. Prange-Lasonder, and J. H. Buurke, "Assessing effects of exoskeleton misalignment on knee joint load during swing using an instrumented leg simulator," *Journal of neuroengineering and rehabilitation*, vol. 19, no. 1, pp. 1–18, 2022.

[36] B. Phillips and H. Zhao, "Predictors of assistive technology abandonment," *Assistive technology*, vol. 5, no. 1, pp. 36–45, 1993.

[37] W. Huo, S. Mohammed, J. C. Moreno, and Y. Amirat, "Lower Limb Wearable Robots for Assistance and Rehabilitation: A State of the Art," *IEEE Systems Journal*, vol. 10, no. 3, pp. 1068–1081, Sept. 2016.

[38] V. Pinskerova, H. Iwaki, and M. A. Freeman, "The shapes and relative movements of the femur and at the knee," *Orthopade*, vol. 29, no. SUPPL. 1, pp. S3–S5, June 2000.

[39] J. D. Blaha, C. A. Mancinelli, W. H. Simons, V. L. Kish, and G. Thyagarajan, "Kinematics of the human knee using an open chain cadaver model," *Clinical Orthopaedics and Related Research®*, vol. 410, pp. 25–34, 2003.

[40] M. Biščević, M. Hebibović, and D. Smrke, "Variations of femoral condyle shape," *Collegium Antropologicum*, vol. 29, no. 2, pp. 409–414, 2005.

[41] H. Kurosawa, P. Walker, S. Abe, A. Garg, and T. Hunter, "Geometry and motion of the knee for implant and orthotic design," *Journal of biomechanics*, vol. 18, no. 7, pp. 487–499, 1985.

[42] S. Koo and T. P. Andriacchi, "The knee joint center of rotation is predominantly on the lateral side during normal walking," *Journal of Biomechanics*, vol. 41, no. 6, pp. 1269–1273, Jan. 2008.

[43] Y. Feng, T.-Y. Tsai, J.-S. Li, H. E. Rubash, G. Li, and A. Freiberg, "In-vivo analysis of flexion axes of the knee: femoral condylar motion during dynamic knee flexion," *Clinical Biomechanics*, vol. 32, pp. 102–107, 2016.

[44] M. G. Lykissas, G. I. Mataliotakis, N. Paschos, C. Panovrakos, A. E. Beris, and C. D. Papageorgiou, "Simultaneous bicompartmental bucket-handle meniscal tears with intact anterior cruciate ligament: A case report," *Journal of Medical Case Reports*, vol. 4, no. 1, p. 34, Dec. 2010.

[45] V. M. Zatsiorsky, *Kinematics of human motion*. Human kinetics, 1998.

[46] L.-W. Tsai, *Robot analysis: the mechanics of serial and parallel manipulators*. John Wiley & Sons, 1999.

[47] L. Blankevoort, R. Huiskes, and A. De Lange, "Helical axes of passive knee joint motions," *Journal of biomechanics*, vol. 23, no. 12, pp. 1219–1229, 1990.

[48] L. Yin, K. Chen, L. Guo, L. Cheng, F. Wang, and L. Yang, "Identifying the functional flexion-extension axis of the knee: an in-vivo kinematics study," *PloS one*, vol. 10, no. 6, p. e0128877, 2015.

[49] J. S. Sulzer, R. A. Roiz, M. A. Peshkin, and J. L. Patton, "A highly backdrivable, lightweight knee actuator for investigating gait in stroke," *IEEE Transactions on Robotics*, vol. 25, no. 3, pp. 539–548, 2009.

[50] C. W. Radcliffe, "Four-bar linkage prosthetic knee mechanisms: Kinematics, alignment and prescription criteria," *Prosthetics and Orthotics International*, vol. 18, no. 3, pp. 159–173, June 1994.

[51] A. B. Zavatsky and J. J. O'Connor, "A Model of Human Knee Ligaments in the Sagittal Plane: Part 1: Response to Passive Flexion," *Proceedings of the Institution of Mechanical Engineers, Part H: Journal of Engineering in Medicine*, vol. 206, no. 3, pp. 125–134, Sept. 1992.

[52] M. Karami, G. Maurice, and J. Andre, "A model of exo-prosthesis of the knee optimized with respect to the physiological motion of condyles," *ITBM-RBM*, vol. 25, no. 3, pp. 176–184, Sept. 2004.

[53] J. M. B. Bertomeu, J. M. B. Lois, R. B. Guillem, Á. P. Del Pozo, J. Lacuesta, C. G. Mollà, P. V. Luna, and J. P. Pastor, "Development of a hinge compatible with the kinematics of the knee joint," *Prosthetics and Orthotics International*, vol. 31, no. 4, pp. 371–383, Dec. 2007.

[54] J.-H. Kim, M. Shim, D. H. Ahn, B. J. Son, S.-Y. Kim, D. Y. Kim, Y. S. Baek, and B.-K. Cho, "Design of a knee exoskeleton using foot pressure and knee torque sensors," *International Journal of Advanced Robotic Systems*, vol. 12, no. 8, p. 112, 2015.

[55] H. Zeng, B. Zeng, G. Yuan, X. Liu, and Z. Yu, "Design and optimization of 2dof humanoid dual cross four-bar mechanism for knee joint of an exoskeleton," in *2022 IEEE International Conference on Robotics and Biomimetics (ROBIO)*. IEEE, 2022, pp. 555–562.

[56] Y.-C. Liu and Y. Takeda, "Kineto-static analysis of a wrist rehabilitation robot with compliance and passive joints for joint misalignment compensation," *Machines*, vol. 8, no. 2, p. 23, 2020.

[57] B. Celebi, M. Yalcin, and V. Patoglu, "AssistOn-Knee: A self-aligning knee exoskeleton," in *IEEE International Conference on Intelligent Robots and Systems*, 2013, pp. 996–1002.

[58] A. T. Asbeck, S. M. M. De Rossi, I. Galiana, Y. Ding, and C. J. Walsh, "Stronger, Smarter, Softer: Next-Generation Wearable Robots," *IEEE Robotics & Automation Magazine*, vol. 21, no. 4, pp. 22–33, Dec. 2014.

[59] J. Wang, X. Li, T.-H. Huang, S. Yu, Y. Li, T. Chen, A. Carriero, M. Oh-Park, and H. Su, "Comfort-centered design of a lightweight and backdrivable knee exoskeleton," *IEEE Robotics and Automation Letters*, vol. 3, no. 4, pp. 4265–4272, 2018.

[60] S. V. Sarkisian, M. K. Ishmael, G. R. Hunt, and T. Lenzi, "Design, development, and validation of a self-aligning mechanism for high-torque powered knee exoskeletons," *IEEE Transactions on Medical Robotics and Bionics*, vol. 2, no. 2, pp. 248–259, 2020.

[61] A. M. Dollar and H. Herr, "Lower extremity exoskeletons and active orthoses: Challenges and state-of-the-art," *IEEE Transactions on robotics*, vol. 24, no. 1, pp. 144–158, 2008.

[62] T. D. Royer and P. E. Martin, "Manipulations of leg mass and moment of inertia: effects on energy cost of walking." *Medicine and science in sports and exercise*, vol. 37, no. 4, pp. 649–656, 2005.

[63] P. Beyl, "Design and control of a knee exoskeleton powered by pleated pneumatic artificial muscles for robot-assisted gait rehabilitation," Ph.D. dissertation, Vrije Universiteit Brussel, 2010.

[64] K. A. Witte, A. M. Fatschel, and S. H. Collins, "Design of a lightweight, tethered, torque-controlled knee exoskeleton," in *2017 international conference on rehabilitation robotics (ICORR)*. IEEE, 2017, pp. 1646–1653.

[65] D. Lee, B. J. McLain, I. Kang, and A. J. Young, "Biomechanical comparison of assistance strategies using a bilateral robotic knee exoskeleton," *IEEE Transactions on Biomedical Engineering*, vol. 68, no. 9, pp. 2870–2879, 2021.

[66] R. Rituraj, R. Scheidl, P. Ladner, M. Lauber, and A. Plöckinger, "Prototyping and experimental investigation of digital hydraulically driven knee exoskeleton," *Energies*, vol. 15, no. 22, p. 8695, 2022.

[67] Y.-X. Liu, L. Zhang, R. Wang, C. Smith, and E. M. Gutierrez-Farewik, "Weight distribution of a knee exoskeleton influences muscle activities during movements," *IEEE Access*, vol. 9, pp. 91 614–91 624, 2021.

[68] J. Li, R. Zheng, Y. Zhang, and J. Yao, "ihandrehab: An interactive hand exoskeleton for active and passive rehabilitation," in *2011 IEEE International Conference on Rehabilitation Robotics*. IEEE, 2011, pp. 1–6.

[69] X. Li, J. Liu, W. Li, Y. Huang, and G. Zhan, "Force transmission analysis and optimization of bowden cable on body in a flexible exoskeleton," *Applied Bionics and Biomechanics*, vol. 2022, 2022.

[70] U. A. Hofmann, T. Bützer, O. Lambercy, and R. Gassert, "Design and evaluation of a bowden-cable-based remote actuation system for wearable robotics," *IEEE Robotics and Automation Letters*, vol. 3, no. 3, pp. 2101–2108, 2018.

[71] Y. Tanaka, S. Sakama, K. Nakano, and H. Kosodo, "Comparative study on dynamic characteristics of hydraulic, pneumatic and electric motors," in *Fluid power systems technology*, vol. 56086. American Society of Mechanical Engineers, 2013, p. V001T01A037.

[72] M. Mori, K. Suzumori, M. Takahashi, and T. Hosoya, "Very high force hydraulic McKibben artificial muscle with a p-phenylene-2,6-benzobisoxazole cord sleeve," *Advanced Robotics*, vol. 24, no. 1-2, pp. 233–254, 2010.

[73] R. Morita, H. Nabae, G. Endo, and K. Suzumori, "A proposal of a new rotational-compliant joint with oil-hydraulic McKibben artificial muscles," *Advanced Robotics*, vol. 32, no. 9, pp. 511–523, May 2018.

[74] E. Trostmann, *Water Hydraulics Control Technology*. CRC Press, 1995.

[75] S. Sakama, Y. Tanaka, and A. Kamimura, "Characteristics of hydraulic and electric servo motors," in *Actuators*, vol. 11, no. 1. MDPI, 2022, p. 11.

[76] X. Zang, Y. Liu, and Y. Zhu, "Structure design of a mobile jack robot," *2013 IEEE International Conference on Information and Automation, ICIA 2013*, pp. 1218–1223, 2013.

[77] H. Kaminaga, T. Ko, R. Masumura, M. Komagata, S. Sato, S. Yorita, and Y. Nakamura, "Mechanism and Control of Whole-Body Electro-Hydrostatic Actuator Driven Humanoid Robot Hydra," *Springer Proceedings in Advanced Robotics*, vol. 1, pp. 656–665, 2016.

[78] K. Suzumori and A. A. Faudzi, "Trends in hydraulic actuators and components in legged and tough robots: a review," *Advanced Robotics*, vol. 32, no. 9, pp. 458–476, May 2018.

[79] M. Hemmi, R. Morita, Y. Hirota, K. Inoue, H. Nabae, G. Endo, and K. Suzumori, "Development of Hydraulic Tough Motors with High Power Density and their Application to a 7-axis Robotic Arm," in *Proceedings of the 2019 IEEE/SICE International Symposium on System Integration, SII 2019*, IEEE. Institute of Electrical and Electronics Engineers Inc., Apr. 2019, pp. 264–269.

[80] M. Raibert, K. Blankespoor, G. Nelson, and R. Playter, "BigDog, the Rough-Terrain Quadruped Robot," *IFAC Proceedings Volumes*, vol. 41, no. 2, pp. 10 822–10 825, 2008.

[81] C. Semini, N. G. Tsagarakis, E. Guglielmino, M. Focchi, F. Cannella, and D. G. Caldwell, "Design of HyQ – a hydraulically and electrically actuated quadruped robot:," *http://dx.doi.org/10.1177/0959651811402275*, vol. 225, no. 6, pp. 831–849, Aug. 2011.

[82] S. Kohlbrecher, A. Romay, A. Stumpf, A. Gupta, O. von Stryk, F. Bacim, D. A. Bowman, A. Goins, R. Balasubramanian, and D. C. Conner, "Human-robot Teaming for Rescue Missions: Team ViGIR's Approach to the 2013 DARPA Robotics Challenge Trials," *Journal of Field Robotics*, vol. 32, no. 3, pp. 352–377, May 2015.

[83] X. Li, H. Zhou, H. Feng, S. Zhang, and Y. Fu, "Design and Experiments of a Novel Hydraulic Wheel-Legged Robot (WLR)," *IEEE International Conference on Intelligent Robots and Systems*, pp. 3292–3297, Dec. 2018.

[84] H. Kaminaga, T. Amari, Y. Niwa, and Y. Nakamura, "Electro-hydrostatic actuators with Series Dissipative property and their application to power assist devices," *2010 3rd IEEE RAS and EMBS International Conference on Biomedical Robotics and Biomechatronics, BioRob 2010*, pp. 76–81, 2010.

[85] B. Song, D. Lee, S. Y. Park, and Y. S. Baek, "Design and Performance of Nonlinear Control for an Electro-Hydraulic Actuator Considering a Wearable Robot," *Processes 2019, Vol. 7, Page 389*, vol. 7, no. 6, p. 389, June 2019.

[86] M. Axin, B. Eriksson, and P. Krus, "Flow versus pressure control of pumps in mobile hydraulic systems," *Proceedings of the institution of mechanical engineers, Part I: journal of systems and control engineering*, vol. 228, no. 4, pp. 245–256, 2014.

[87] C. Williamson and M. Ivantysynova, "The effect of pump efficiency on displacement-controlled actuator systems," in *The Tenth Scandinavian International Conference on Fluid Power*, 2007, pp. 301–326.

[88] N. Alle, S. S. Hiremath, S. Makaram, K. Subramaniam, and A. Talukdar, "Review on electro hydrostatic actuator for flight control," *International Journal of Fluid Power*, vol. 17, no. 2, pp. 125–145, 2016.

[89] Q. Chao, J. Zhang, B. Xu, H. Huang, and M. Pan, "A Review of High-Speed Electro-Hydrostatic Actuator Pumps in Aerospace Applications: Challenges and Solutions," *Journal of Mechanical Design, Transactions of the ASME*, vol. 141, no. 5, May 2019.

[90] V. Karanovic, M. Jocanovic, and V. Jovanovic, "Review of Development Stages in the Conceptual Design of an Electro Hydrostatic Actuator for Robotics," *Acta Polytechnica Hungarica*, vol. 11, no. 5, pp. 59–79, 2014.

[91] I. Dulay, *Fundamentals of Hydraulic Power Transmission*, ser. Studies in mechanical engineering. Elsevier, 1988.

[92] Y. Sang, Y. Han, and F. Duan, "Study on the alternating flow hydraulics and its new potential application in the geotechnical testing field," *International Journal of Fluid Machinery and Systems*, vol. 9, no. 3, pp. 245–255, 2016.

[93] T. Miyoshi, K. Yoshida, S. I. Eom, and S. Yokota, "Proposal of a multiple ER microactuator system using an alternating pressure source," *Sensors and Actuators A: Physical*, vol. 222, pp. 167–175, Feb. 2015.

[94] T. Sudhawiyangkul, K. Yoshida, S. I. Eom, and J. wan Kim, "A novel bending microactuator with integrated flexible electro-rheological microvalves using an alternating pressure source for multi-actuator systems," *Microsystem Technologies*, vol. 26, no. 5, pp. 1507–1519, 2020.

[95] F. Conrad, "Trends in design of water hydraulics-motion control and open-ended solutions," in *Proceedings of the JFPS International Symposium on Fluid Power*, vol. 2005, no. 6. The Japan Fluid Power System Society, 2005, pp. 420–431.

[96] *Pirtek Hydraulic Oil 10 Safety Data Sheet*, Pirtek UK Ltd, 3 2016, revision 1.

[97] T. Takahashi, C. Yamashina, and S. Miyakawa, "Development of water hydraulic proportional control valve," *Proceedings of the JFPS International Symposium on Fluid Power*, vol. 1999, no. 4, pp. 549–554, 1999.

[98] X. Wang and A. Yamaguchi, "Characteristics of hydrostatic bearing/seal parts for water hydraulic pumps and motors. Part 1: Experiment and theory," *Tribology International*, vol. 35, no. 7, pp. 425–433, July 2002.

[99] S. Kittisares, H. Nabae, G. Endo, K. Suzumori, and R. Sakurai, "Design of knee support device based on four-bar linkage and hydraulic artificial muscle," *ROBOMECH Journal*, vol. 7, no. 1, pp. 1–10, 2020.

[100] T. J. Engen, "a Plastic Hand Orthosis," *Orthopedic & Prosthetic Appliance Journal*, vol. 13, no. 3, pp. 38–43, 1959.

[101] Ching-Ping Chou and B. Hannaford, "Measurement and modeling of McKibben pneumatic artificial muscles," *IEEE Transactions on Robotics and Automation*, vol. 12, no. 1, pp. 90–102, 1996.

[102] K. Kuribayashi, "Criteria for the Evaluation of New Actuators as Energy Converters," *Advanced Robotics*, vol. 7, no. 4, pp. 289–307, 1992.

[103] F. H. Schulte, "The Characteristics of the McKibben Artificial Muscle," in *The Application of External Power in Prosthetics and Orthotics*. Washington, D.C.: National Academy of Sciences-National Research Council, 1961, pp. 94–115.

[104] B. Tondu, "Modelling of the McKibben artificial muscle: A review," *Journal of Intelligent Material Systems and Structures*, vol. 23, no. 3, pp. 225–253, Feb. 2012.

[105] L. R. G. Treloar, *The Physics of Rubber Elasticity*, 3rd ed. New York: Oxford University Press, 2005.

[106] S. Kurumaya, H. Nabae, G. Endo, and K. Suzumori, "Design of thin McKibben muscle and multifilament structure," *Sensors and Actuators A*, vol. 261, pp. 66–74, 2017.

[107] P. De Leva, "Adjustments to zatsiorsky-seluyanov's segment inertia parameters," *Journal of Biomechanics*, vol. 29, no. 9, pp. 1223–1230, Sept. 1996.

[108] V. M. Zatsiorsky, *Kinetics of Human Motion*. Champaign, IL: Human Kinetics, 2002.

[109] M. K. Mak, O. Levin, J. Mizrahi, and C. W. Hui-Chan, "Joint torques during sit-to-stand in healthy subjects and people with Parkinson's disease," *Clinical Biomechanics*, vol. 18, no. 3, pp. 197–206, Mar. 2003.

[110] K. Kamali, A. A. Akbari, and A. Akbarzadeh, "Trajectory generation and control of a knee exoskeleton based on dynamic movement primitives for sit-to-stand assistance," *Advanced Robotics*, vol. 30, no. 13, pp. 846–860, 2016.

[111] E. W. Weisstein, "Line-Line Intersection." [Online]. Available: http://mathworld.wolfram.com/Line-LineIntersection.html

[112] "Welcome to SENIAM," Oct. 2004, [Online; accessed 11. Aug. 2023]. [Online]. Available: http://www.seniam.org

[113] S. Kittisares, Y. Hirota, H. Nabae, G. Endo, and K. Suzumori, "Alternating pressure control system for hydraulic robots," *Mechatronics*, vol. 85, p. 102822, 2022.

[114] E. Lisowski, G. Filo, and J. Rajda, "Analysis of the energy efficiency improvement in a load-sensing hydraulic system built on the iso plate," *Energies*, vol. 14, no. 20, p. 6735, 2021.

[115] F. Freudenstein, "Approximate synthesis of four-bar linkages," *Transactions of the American Society of Mechanical Engineers*, vol. 77, no. 6, pp. 853–859, 1955.

[116] "Genetic Algorithm Options - MATLAB & Simulink," [Online; accessed 11. May 2023]. [Online]. Available: https://www.mathworks.com/help/gads/genetic-algorithm-options.html

[117] "Vary Mutation and Crossover - MATLAB & Simulink," [Online; accessed 11. May 2023]. [Online]. Available: https://www.mathworks.com/help/gads/vary-mutation-and-crossover.html

[118] R. Chandra and C. W. Omlin, "The comparison and combination of genetic and gradient descent learning in recurrent neural networks: An application to speech phoneme classification." in *Artificial Intelligence and Pattern Recognition*. Citeseer, 2007, pp. 286–293.

[119] C. G. Broyden, "A class of methods for solving nonlinear simultaneous equations," *Mathematics of computation*, vol. 19, no. 92, pp. 577–593, 1965.

[120] ——, "The convergence of a class of double-rank minimization algorithms 1. general considerations," *IMA Journal of Applied Mathematics*, vol. 6, no. 1, pp. 76–90, 1970.

[121] R. Fletcher, "A new approach to variable metric algorithms," *The computer journal*, vol. 13, no. 3, pp. 317–322, 1970.

[122] D. Goldfarb, "A family of variable-metric methods derived by variational means," *Mathematics of computation*, vol. 24, no. 109, pp. 23–26, 1970.

[123] D. F. Shanno, "Conditioning of quasi-newton methods for function minimization," *Mathematics of computation*, vol. 24, no. 111, pp. 647–656, 1970.

[124] W. C. Davidon, "Variable metric method for minimization," *SIAM Journal on Optimization*, vol. 1, no. 1, pp. 1–17, 1991.

[125] R. Fletcher, *Practical methods of optimization*. John Wiley & Sons, 2013.

[126] A. R. Conn, N. I. Gould, and P. L. Toint, "Convergence of quasi-newton matrices generated by the symmetric rank one update," *Mathematical programming*, vol. 50, no. 1-3, pp. 177–195, 1991.

[127] A. Protopapadaki, W. I. Drechsler, M. C. Cramp, F. J. Coutts, and O. M. Scott, "Hip, knee, ankle kinematics and kinetics during stair ascent and descent in healthy young individuals," *Clinical biomechanics*, vol. 22, no. 2, pp. 203–210, 2007.

[128] A. H. Larsen, H. Sørensen, L. Puggaard, and P. Aagaard, "Biomechanical determinants of maximal stair climbing capacity in healthy elderly women," *Scandinavian journal of medicine & science in sports*, vol. 19, no. 5, pp. 678–686, 2009.

[129] T. Andriacchi, G. Andersson, R. Fermier, D. Stern, and J. Galante, "A study of lower-limb mechanics during stair-climbing." *JBJS*, vol. 62, no. 5, pp. 749–757, 1980.

[130] B. J. McFadyen and D. A. Winter, "An integrated biomechanical analysis of normal stair ascent and descent," *Journal of biomechanics*, vol. 21, no. 9, pp. 733–744, 1988.

[131] G. B. Salsich, J. H. Brechter, and C. M. Powers, "Lower extremity kinetics during stair ambulation in patients with and without patellofemoral pain," *Clinical Biomechanics*, vol. 16, no. 10, pp. 906–912, 2001.

[132] R. Riener, M. Rabuffetti, and C. Frigo, "Stair ascent and descent at different inclinations," *Gait & posture*, vol. 15, no. 1, pp. 32–44, 2002.

[133] S. M. Reid, S. K. Lynn, R. P. Musselman, and P. A. Costigan, "Knee biomechanics of alternate stair ambulation patterns." *Medicine and science in sports and exercise*, vol. 39, no. 11, pp. 2005–2011, 2007.

[134] N. D. Reeves, M. Spanjaard, A. A. Mohagheghi, V. Baltzopoulos, and C. N. Maganaris, "Older adults employ alternative strategies to operate within their maximum capabilities when ascending stairs," *Journal of Electromyography and Kinesiology*, vol. 19, no. 2, pp. e57–e68, 2009.

[135] P. A. Costigan, K. J. Deluzio, and U. P. Wyss, "Knee and hip kinetics during normal stair climbing," *Gait & posture*, vol. 16, no. 1, pp. 31–37, 2002.

[136] T. Andriacchi, J. Galante, and R. Fermier, "The influence of total knee-replacement design on walking and stair-climbing." *JBJS*, vol. 64, no. 9, pp. 1328–1335, 1982.

[137] G. Markovich, P. Riley, D. Krebs, R. Mann, and W. Hodge, "Biomechanical analysis of knee motion upon stair acent and descent," *Journal of Biomechanics*, vol. 23, no. 7, p. 725, 1990.

[138] P. Costigan, U. Wyss, K. Deluzio, and J. Li, "Semiautomatic three-dimensional knee motion assessment system," *Medical and Biological Engineering and Computing*, vol. 30, pp. 343–350, 1992.

[139] D. L. Kowalk, J. A. Duncan, and C. L. Vaughan, "Abduction-adduction moments at the knee during stair ascent and descent," *Journal of biomechanics*, vol. 29, no. 3, pp. 383–388, 1996.

[140] P. Joudzadeh, A. Hadi, and K. Alipour, "Conceptual design of a lower limb exoskeleton actuated by shape memory alloys for assisting elderly people in stair climbing," in *2016 4th International Conference on Robotics and Mechatronics (ICROM)*. IEEE, 2016, pp. 530–535.

[141] R. Chaichaowarat, V. Macha, and W. Wannasuphoprasit, "Passive knee exoskeleton using brake torque to assist stair ascent," in *2020 IEEE REGION 10 CONFERENCE (TENCON)*. IEEE, 2020, pp. 1165–1170.

List of Publications

Peer-reviewed Journal Articles

1. **S. Kittisares**, H. Nabae, G. Endo, K. Suzumori, and R. Sakurai, "Design of knee support device based on four-bar linkage and hydraulic artificial muscle," *Robomech Journal*, vol. 7, no. 1, p. 16, 2020.

2. **S. Kittisares**, Y. Hirota, H. Nabae, G. Endo, and K. Suzumori, "Alternating pressure control system for hydraulic robots," *Mechatronics*, vol. 85, p. 102822, 2022.

Conference Presentations

1. **S. Kittisares**, H. Nabae, G. Endo, and K. Suzumori, "Knee Support Device with Polycentric Joint Mechanism Driven by Bundled Thin Soft Muscles," in *The Proceedings of JSME annual Conference on Robotics and Mechatronics (Robomec) 2019*, 2019, pp. 2P1-M03.

2. **S. Kittisares**, H. Nabae, G. Endo, K. Suzumori, R. Sakurai, and S. Ohno, "Hydraulic Artificial Muscle-Powered Knee Support Wearable Device with Four-bar Linkage Mechanism," in *The Proceedings of JSME annual Conference on Robotics and Mechatronics (Robomec) 2020*, 2020, pp. 2P1-C08.

3. **S. Kittisares**, Y. Hirota, H. Nabae, G. Endo, and K. Suzumori, "APCS: A lightweight and efficient hydraulic system," in *The Proceedings of JSME annual Conference on Robotics and Mechatronics (Robomec) 2022*, 2022, pp. 2A1-L05.

4. **S. Kittisares**, H. Nabae, and K. Suzumori, "Sit-to-Stand-Assist Exosuit Powered by Variable-Stiffness Muscle," in *The Proceedings of JSME annual Conference on Robotics and Mechatronics (Robomec) 2023*, 2023, pp. 2A1-B20.

Other Publication

1. **S. Kittisares**, S. Yasuda, T. Kumagai, and H. Yoshida, "Error Prediction of a Differential Drive Wheeled Robot with a Swivel Caster Wheel," in *Proceedings of the 22nd IFAC World Congress* (In press)

Acknowledgment

This work was supported by the JSPS KAKENHI Grant-in-Aid for Scientific Research(A) grant number JP18H03760.

First and foremost, I would like to express my deepest gratitude to my advisor, Prof. Koichi Suzumori, for his unwavering support and invaluable guidance throughout my thesis journey. I am truly grateful for his willingness to provide consultation and support whenever needed. I consider myself incredibly fortunate to have had a supervisor who not only fostered my academic growth but also genuinely cared for my overall well-being. I am immensely thankful for his generosity in dedicating his time and expertise, which I sincerely appreciate.

I would also like to thank to Prof. Gen Endo for providing practical insights and presenting various real-world problems and solutions during our joint seminar. Additionally, I am grateful to Asst. Prof. Hiroyuki Nabae for his impeccable theoretical advice. Their dependable technical insights and constructive criticisms have been indispensable to my research progress and personal development as a researcher.

Special appreciation goes to the late Mr. Yoshiharu Hirota for his technical assistance in this research endeavor. His contributions were invaluable, and his passing is deeply mourned. I would also like to acknowledge Dr. Tohru Ide for his technical assistance in this research and Dr. Feng Yunhao for his consistent support. Furthermore, I express my gratitude to Ms. Naomi Suzuki, Ms. Miwako Shigeto, and Ms. Yoko Kurihara for their unwavering help within the laboratory.

I wish to express my sincere gratitude to Dr. Ryo Sakurai and Dr. Shingo Ohno from Bridgestone Corporation for their collaboration and the provision of numerous customized HAMs, which have played an indispensable role in my research.

Lastly, I would like to convey my deepest appreciation to my parents for their unwavering support and encouragement throughout my life.